Additive Manufacturing of Soft Magnetic Fe50Ni

A

Thesis

Presented to

the faculty of the School of Engineering and Applied Science

University of Virginia

---

in partial fulfillment

of the requirements for the degree

Master of Science

by

Elizabeth Urig

December 2020

APPROVAL SHEET

This

Thesis

is submitted in partial fulfillment of the requirements
for the degree of

Master of Science

Author: Elizabeth Urig

This Thesis has been read and approved by the examing committee:

Advisor: Dr. James Fitz-Gerald

Advisor:

Committee Member: Dr. Ji Ma

Committee Member: Dr. William Soffa

Committee Member: Karen Taminger

Committee Member:

Committee Member:

Committee Member:

Accepted for the School of Engineering and Applied Science:

Craig H. Benson, School of Engineering and Applied Science

December 2020

Abstract

Soft magnetic alloys are widely utilized in electric motors, transformers, and sensors because of their high saturation magnetization, low coercivity, and high permeability. In this research, the magnetic and microstructural properties of Fe50Ni samples manufactured with two additive manufacturing processes, electron beam freeform fabrication (EBF^3) and selective laser melting (SLM), were characterized and correlated with processing parameters.

Using wire and powder feedstock, samples were printed with varying scan speed, beam power, and energy density. Samples were characterized by optical and scanning electron microscopy, electron backscatter diffraction, x-ray dispersive spectroscopy, and vibrating sample magnetometry to correlate the resulting magnetic response with material properties.

While both the EBF^3 and SLM processes were successful in printing Fe50Ni, the EBF^3 depositions exhibited a high degree of printability with no visible porosity or cracking. In comparison, the SLM printed samples resulted in a wide printability map, yielding both excellent and poor quality samples. Significant porosity was observed in many of the SLM samples, with relative densities ranging from 63.7 to 99.0%. High quality SLM samples were deposited at a volumetric energy density of 76.39 J/mm^3, in strong agreement with literature values (60.93 to 83.33 J/mm^3) and the EBF^3 values (87.48 J/mm^3). In addition, the two processes resulted in significantly different melt pool sizes (3.429 mm^2 for EBF^3, 0.0036 mm^2 for SLM) due to absorption and penetration differences in the two heat sources. The differing melt pools impacted the deposition, solidification, and cooling rates. The predicted maximum cooling rate for high quality samples was 5.2x10^{-3} K/s for EBF^3 and 1.8x10^{-7} K/s for SLM, which resulted in a significant variation in grain size, ranging from 566 to 1064 μm for EBF^3 and 16 to 81 μm for SLM.

The structure insensitive magnetic property, saturation magnetization (Ms), exhibited minimal variance, remaining relatively unchanged through the varied processing parameters for both EBF^3 and SLM. All printed samples were shown to be disordered FCC, with saturation magnetization values ranging from 141 to 148 emu/g, near the literature value of 154 emu/g for Fe50Ni.

No significant change in saturation magnetization was observed between the feedstock materials and the final samples, which is consistent with unchanging phase and composition through the printing process.

With respect to the structure sensitive magnetic properties, several microstructural aspects of the material contribute. In general, large grains, minimal porosity, and preferred texture orientation are desired to enhance the structure sensitive magnetic properties. The samples had measured coercivities (H_c) ranging from 1.15 to 6 Oe, and permeabilities (μ) ranging from 37 to 160. The EBF^3 samples exhibited large FCC columnar grains (280 μm), with strong Goss texture. The SLM samples generally had less Goss texture, which weakened as porosity increased.

Overall, samples printed by EBF^3 exhibited lower coercivity values in comparison to SLM printed samples. The lower coercivity associated with EBF^3 suggests that soft magnetic components printed by EBF^3 may have merit. EBF^3 samples exhibit large grains and a strong Goss texture, both of which are favorable for the structure sensitive properties of soft magnetic Fe50Ni. While the research is still in its infancy, the production of additively manufactured soft magnetic materials shows promise for more customizable, novel soft magnetic components.

Acknowledgments

A big thank you goes to my advisor, Prof. Jim Fitz-Gerald, who has mentored and shepherded both this work and me for the last 3 years. He helped me to grow immensely as a budding research scientist and person. The work presented in this document would be a shadow of its current form without the mentorship and advising provided.

An equally important person to acknowledge and thank is my mentor, Karen Taminger. She provided a naive, bright-eyed undergrad the ability to flourish with opportunities and endless guidance. The encouragement, perspectives, technical feedback, and support are what allowed me to persevere and complete my Master's work.

I also want to thank my two faculty committee members, Prof. Ji Ma and Prof. William Soffa, for their dedication of time and insight into my research and thesis. Thank you to Prof. Ji Ma for his willingness to serve as chair of the committee and facilitate discussion and improvements to my thesis work. To Prof. William Soffa, thank you for setting aside the time to teach a remote student in the art of magnetic materials and transform her into a proper, cgs-unit-using magnetician.

A thank you goes to the NASA Langley Research Center and the National Institute of Aerospace for providing me with the opportunity to pursue my graduate education while performing my research alongside NASA scientists and engineers. Specifically, I would like to thank the Compact Additively Manufactured Innovative Electric Motor (CAMIEM) project, under which my research was funded.

Within NASA Langley are the people who supported the day-to-day endeavors and challenges this thesis presented. Thank you to the entire metals group within the Advanced Materials and Processing Branch, whose researchers and technicians facilitated the physical, tangible samples and technical support, even after a pandemic limited my own laboratory access. Outside of the metals group, I wish to acknowledge and thank Dr. Samuel Hocker and Dr. Russell "Buzz" Wincheski who facilitated my CAMIEM involvement and magnetic measurements.

I would be remiss not to thank the current and former Fitz-Gerald graduate students, especially my office-mates Cecilia Mulvaney and Bryan Koscielny. Your constant support through this process, both technical and interpersonal, made this degree possible. From frantic whiteboard scribbles to Friday lunch breaks, my time at NASA and as a graduate student would not be the same without you.

Finally, I want to thank my friends and family. To my honorary editors, Cecilia (editor-in-chief), Bryan, Jonathan, John, Matt, Kubi, Jess, Chris, and Alex, your guidance and quick turn-around times let my work shine beyond my grammar tendencies. Beyond the technical feedback, I appreciate the endless conversation, commiseration, love, and support I received throughout this endeavor. This was possible because of you.

Contents

Chapter 1
Introduction

1.1 Motivation

The *Compact Additively Manufactured Innovative Electric Motor* (CAMIEM) project at NASA worked to improve the efficiency and manufacturability of a lightweight axial flux permanent magnet motor through additive manufacturing methods [1]. In axial flux motors, a stacked rotor and stator generate magnetic flux linearly through the rotor [2]. The magnetic flux changes direction rapidly as the axial flux motor cycles, which reduces motor efficiency through magnetic core and eddy current losses. Soft magnetic structural core components and hardware are used to reduce magnetic core losses and improve motor efficiency [2]. Soft magnetic materials are a particular group of magnetic materials which respond to changing magnetic flux fields rapidly with minimal core losses.

One of the objectives of the CAMIEM project was to assess the feasibility of producing soft magnetic components through additive manufacturing. By additively manufacturing the soft magnetic stator core and other complex components, the number of individual components in the motor can be reduced and the magnetic response of each component can be tailored to a specific application while improving motor efficiency.

Fe-Ni, commonly known as permalloy, is a soft magnetic material used in industry for transformer cores, choke cores, magnetic shielding and conductors [3]. The core objective of the work described in this thesis was to determine the viability of producing desirable magnetic responses in Fe50Ni with additive manufacturing by evaluating the influence of manufacturing processing parameters and the resulting microstructure on the optimization of the magnetic response.

1.2 Scope of Work

This thesis investigates the metallurgical and magnetic responses of Fe50Ni produced with additive manufacturing. The thesis condenses relevant background literature, describes the manufacturing and characterization performed, presents the metallurgical and magnetic measurements, and summarizes the findings.

Chapter 2 provides an overview of magnetic materials and additive manufacturing. Key magnetic concepts, measurements, and features are reviewed. The relationship between magnetic response and microstructure is described and the ideal magnetic response for soft magnetic materials is explained. Two additive manufacturing methods utilized in this work, Electron Beam Freeform Fabrication (EBF^3) and Selective Laser Melting (SLM), are discussed. The material system chosen for this work, Fe-Ni, is reviewed. Rationale for alloy selection is detailed and a phase diagram and material properties are provided. The manufacturing techniques for Fe-Ni from historical and modern perspectives, including hydrogen annealing, welding, and additive manufacturing are reviewed. Finally, historical and current literature for manufacturing Fe-Ni and other magnetic material systems is aggregated.

Chapter 3 describes the initial materials, processing, and characterization that were performed. Initial powder and wire feedstock are summarized. Next, deposition parameters for EBF^3 and SLM are enumerated. Metallurgical characterization was done with a combination of optical and scanning electron microscopy (SEM), energy dispersive X-ray spectroscopy (EDS), electron backscatter diffraction (EBSD), and X-ray diffraction (XRD). The microstructural analysis of grain size, texture, phase, and composition for both SLM and EBF^3 samples was performed. The experimental set-up for magnetic hysteresis loop collection using a Vibrating Sample Magnetometer (VSM) is described. Coercivity, permeability, hysteresis loss, and saturation magnetization were also recorded. A thermal model of melt pool solidification, used to provide estimates for cooling rates and melt pool morphology for a subset of EBF^3 and SLM experimental samples, is presented.

Chapter 4 aggregates the metallurgical and magnetic data for starting materials and EBF^3 and SLM deposits and presents the results from the melt pool simulations. The metallurgical characterization performed to confirm vendor specifications and magnetic measurements for the starting materials are given.

The EBF^3 metallurgical results, magnetic properties and process-property relationships are presented. SLM metallurgical and magnetic results are provided using the same format as the EBF^3 results. The resulting melt pool dimensions and predicted cooling rates from the simulation described in Chapter 3 are reported.

Chapter 5 interprets and discusses the overall results. The printability of Fe-Ni using EBF^3 and SLM is explored. Comparisons between SLM and EBF^3 cooling rate regimes were performed. Microstructure-process-property correlations between magnetic properties, input parameters, and grain morphology are made. Relationships between texture, grain size, porosity, and structure sensitive magnetic properties such as coercivity and permeability are discussed. The relationship among interconnected properties to variations in cooling rates observed between the EBF^3 and SLM processing regimes are presented.

Chapter 6 summarizes the main findings of the work and makes recommendations for further research.

Chapter 2
Background

2.1 Background: Magnetic Materials

Since this thesis focuses on developing magnetic fields, a clarification and distinction between magnetic classes and types is important. Materials are classified by responses to applied magnetic fields. Five classifications exist: diamagnetism, paramagnetism, ferromagnetism, ferrimagnetism, and antiferromagnetism [4].

The classes used for traditional magnetic applications are ferri- and ferromagnetic. These two classes exhibit desirable parallel magnetic moment alignment and spontaneous magnetization.

Magnetic moments are generated from electron orbit and electron spin of an atom. For both classes, spontaneous magnetization occurs on the microscale when atomic magnetic moments align favorably, dependent on electron orbitals and lattice structure. In ferro- and ferrimagnets, these microscale spontaneous magnetic moments align parallel or antiparallel with neighboring magnetic moments, forming magnetic domains [5].

Generally, Fe, Ni, Co, and Mn form alloys and intermetallics which generate the appropriate electron orbital to lattice constant spacing for ferromagnetism [5]. This is emphasized by the Bethe-Slater curve, which demonstrates the relationship between magnetic moment and interatomic to d-orbital shell radius ratio (Figure 2.1).

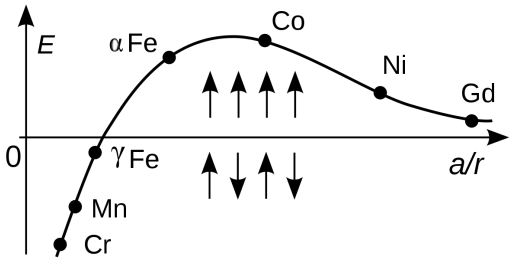

Figure 2.1: Bethe-Slater curve, demonstrating the quantitative magnetic moment of ferromagnetic crystals dependent on the interatomic crystal distance:d-orbital shell radius ratio [5]

The key difference between ferri- and ferromagnetism lies in the magnitude of the saturation magnetization. In a ferromagnet, the magnetic moments align in a parallel manner throughout the lattice, forming magnetic domains which compound the effects of all the singular magnetic moments. In ferrimagnets, the material structure is comprised of two sub-lattices. When the magnetic moments align in a magnetic domain, one lattice amplifies the effect of the magnetic field, while the other responds antiparallel to the field direction, "demagnetizing" the domain and reducing the overall effect.

For this reason, although ferri- and ferromagnets are similar in magnetic properties, the saturation magnetizations of ferrimagnets are much lower than those of ferromagnets [4]. Ferromagnets remain the main category of magnetic class for use in magnetic field applications.

In the presence of an externally applied magnetic field, the magnetic domains of ferromagnets align in the bulk material. An example of this global alignment with an externally applied upward field is demonstrated in Figure 2.2.

Evaluation of Magnetic Materials

Within the more useful classes of magnetic materials lies another division: soft and hard magnets. This division characterizes a ferromagnetic material's response in an externally applied magnetic field.

The magnetic response to an applied magnetic field is visualized by a hysteresis loop. The x-axis denotes the magnitude of the applied magnetic field, while

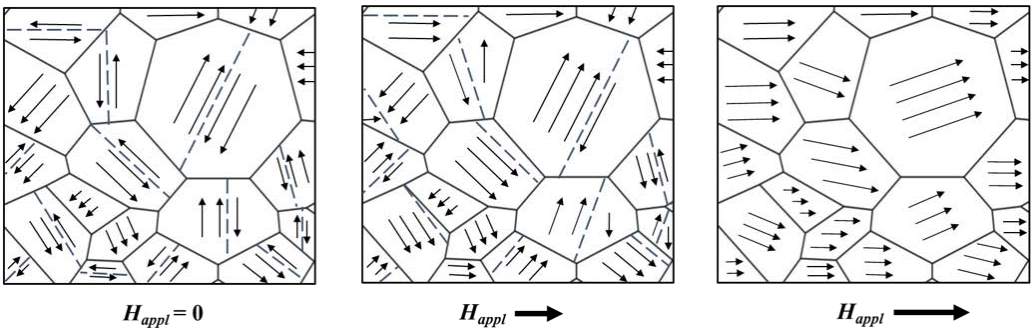

Figure 2.2: Magnetic domain alignment with an applied external magnetic field. As the applied magnetic field H_{appl} increases in magnitude, magnetic domains within the material align to match the direction of the applied field.

the y-axis shows the induced magnetic response of the material. The applied field is loaded in a cyclic nature; the magnetic response forms a loop when plotted in 2D space.

Hard, also known as permanent, magnets are characterized by large, rectangular hysteresis loops. Conceptually, it takes a large magnetic field to align all the domains, but once the domains are aligned, they will remain aligned at low applied fields.

In contrast, an ideal soft magnet hysteresis loop is rather a straight line. Typical soft magnet applications require a high sensitivity to the applied magnetic field. Soft magnetic material domains are expected to align with applied magnetic fields of varying magnitudes. Figure 2.3 shows the general hysteresis loop shapes for hard and soft ideal magnetic materials, along with the real material loops.

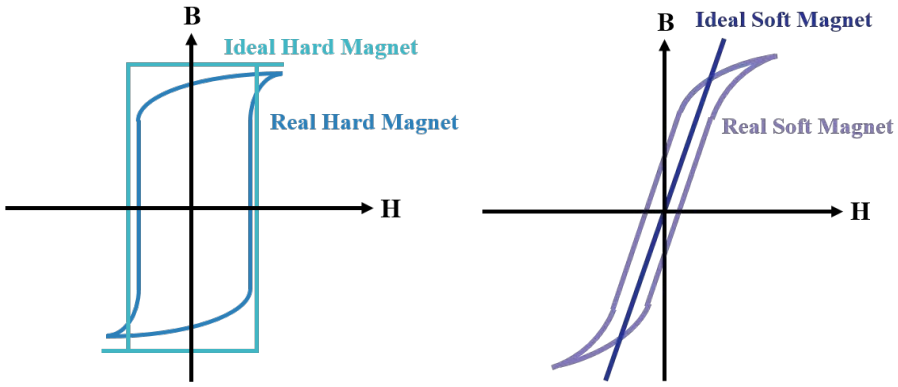

Figure 2.3: Hard and soft hysteresis loops, idealized and for real materials. The figure emphasizes the differences in loop shape and axis intercepts. [6]

The area enclosed by a hysteresis loop is quantified as hysteresis loss. The area, often reported in Watts/cycle (W/cycle), is the energy lost to rotating domains every time the applied field cycles [5]. For soft magnetic materials, a very low hysteresis loss is desired to minimize losses.

Magnetic Material Properties

Hysteresis loops provide quantitative measurements for many magnetic properties, including coercivity, permeability, and saturation magnetization. All three of these magnetic properties are weighted when determining the application of a magnetic material. The saturation magnetization is given as the positive and negative y-axis asymptote on the hysteresis loop. Physically, this occurs when all domains are aligned in the direction of the applied magnetic field. Coercivity is given as the x-axis intercepts. Coercivity is the applied field required to bring the total magnetic flux within the sample (B) to zero. Finally, the maximum permeability is the maximum slope between the origin of the B-H graph and a point on the hysteresis loop which gives this maximum. Figure 2.4 indicates the positions of maximum permeability, coercivity, and saturation magnetization.

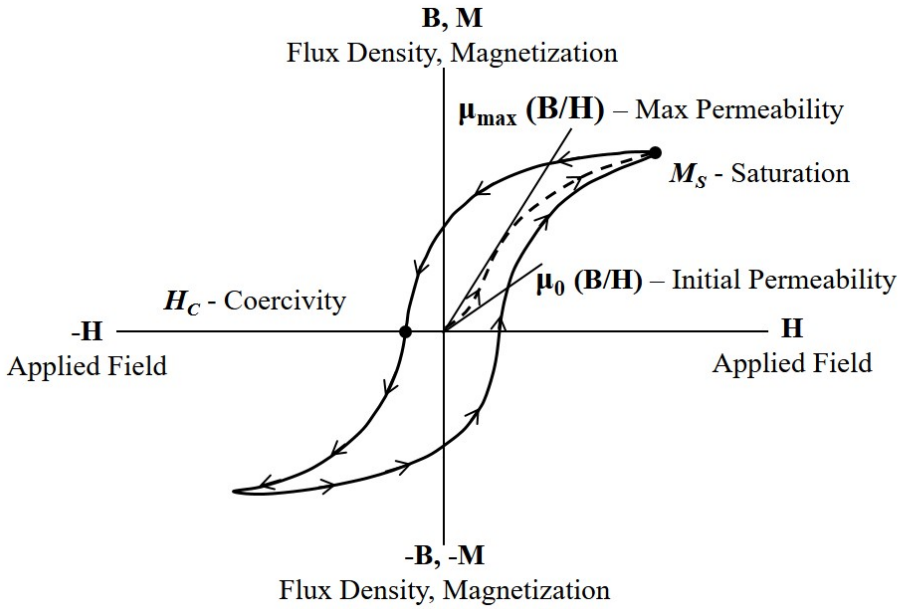

Figure 2.4: Hysteresis loop with key magnetic properties (saturation, coercivity, permeability) labeled [7]

Magnetic Properties and Microstructure Linkage

When tailoring magnetic properties for an application, the divide between structure sensitive and insensitive properties must be considered. For soft magnetic material applications, low coercivity, high permeability, and high saturation magnetization are desired.

Coercivity and permeability are structure sensitive properties which are dependent on the grain size, texture, and porosity of a sample. Coercivity and permeability are both measurements which describe the way domain walls move and propagate through a microstructure. Similar to dislocations, magnetic domain walls have preferred crystal directions for movement and can become pinned on grain boundaries and porosity. A textured microstructure with minimal grain boundaries and defects is desired for low coercivity and high permeability.

Saturation magnetization is a structure insensitive property. This property,

which measures the magnetization of a sample when the magnetic domains are all aligned, is dependent only on the phase and composition of the material.

2.2 Additive Manufacturing Overview

Fundamental knowledge and research conducted in metallic additive manufacturing (AM) has expanded dramatically in recent years. To best encompass the rapidly evolving field, the authors of *Additive manufacturing of metallic components - Process, structure and properties* offer the following definition of the metallic AM processes:

> The AM processes consolidate feedstock materials such as powder, wire or sheets into a dense metallic part by melting and solidification with the aid of an energy source such as laser, electron beam or electric arc, or by the use of ultrasonic vibration in a layer by layer manner. [8]

This definition points to a key facets and area of concern for additive manufacturing - localized rapid solidification. The rapid solidification of additive manufacturing gives rise to non-equilibrium structures. Metastable phases, varied microstructures, and residual stresses must all be considered when utilizing additive manufacturing [8]. Similar to welding, additive manufacturing encourages preferential grain growth in the direction of largest cooling rate and temperature gradient [9].

As cooling rates are highly dependent on the energy source and printing parameters, the subsequent microstructure is as well [10]. Figure 2.5 demonstrates the solidification relationships of cooling rate, grain morphology, and melt pool location [11]. Additive structures have been shown to exhibit heterogeneous nucleation, with epitaxial growth at the melt pool boundaries, transitioning to a more equiaxed dendritic structure in the center of the melt pool [10]. The variation in microstructure is typically a signature of additive structures, which impacts the mechanical and magnetic properties of the final part significantly [10].

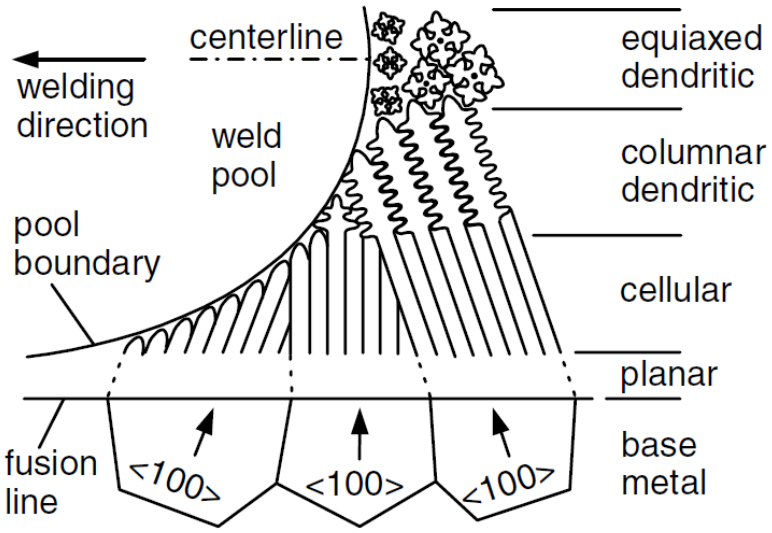

Figure 2.5: Solidification structure regimes for a given velocity profile showing varying grain morphology depending on melt pool location. The centerline of the weld tends to demonstrate more dendritic and equiaxed structures, while melt pool boundaries have cellular and even planar grains [11].

For this work, two different additive manufacturing methods are used to compare the effects of different energy sources and cooling rates. The first, Electron Beam Freeform Fabrication (EBF^3), is a wire-based directed energy deposition system which utilizes an electron beam energy source. The second system used is Selective Laser Melting (SLM), which uses a laser energy source and powder feedstock.

2.2.1 Electron Beam Freeform Fabrication

Electron Beam Freeform Fabrication (EBF^3) is a large scale wire-based process developed at NASA Langley Research Center in 2003 [12]. Utilizing a modified Sciaky AccuBeam VX.4 electron beam welder, EBF^3 is considered a directed energy deposition process, with wire feedstock and the electron beam as an energy source. The process is performed under vacuum (10^{-4} Torr) [13]. A process schematic is shown in Figure 2.6.

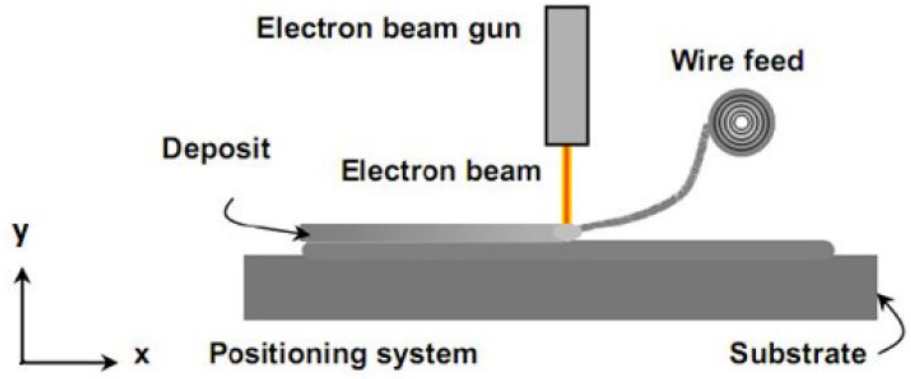

Figure 2.6: Electron beam freeform fabrication diagram, showing the system mid-deposit, with wire being fed into the electron beam heat source to melt and consolidate on previous layers [13]

A deposition is produced by using the electron beam to generate a molten pool on a flat baseplate, then feeding wire into the molten pool. As this system translates horizontally, a layer is deposited. Subsequent layers deposited in this fashion result in a 3-D sample, manifested as a deposit.

EBF^3 has control over the deposition rate and beam parameters. For a typical deposit, deposition rate is controlled by the speed at which wire is fed into the pool (WF) and the velocity the electron beam and wire feeder translate relative to the deposited metal (TS). The electron beam is formed by collimating a beam of electrons off a filament current source (BC) through an accelerating voltage (AV). Similar to an SEM, this collimated beam is manipulated through focusing and deflecting coils before striking the baseplate substrate. These coils are considered controllable machine parameters through the variables beam focus (BF) and raster pattern. Additional print parameters that must be programmed are layer height, sample geometry, and pause time between layers [14].

All programming is done through G-code. For machine parameter optimization tests, deposit geometry is typically printed in "single-bead" depositions, where each layer is a single straight line. Generally, the most impactful variables

are accelerating voltage (AV) beam current (BC), translation speed (TS) and beam focus (BF) [13].

To predict and normalize deposition variables, linear energy density (Equation 2.1) can estimate the overall heat source impact of deposition parameters, where AV is accelerating voltage (kV), BC is beam current (mA), and TS is the translation speed in inches per minute (ipm).

$$E_L = \frac{60AV \cdot BC}{1000TS} \frac{\text{kJ}}{\text{in}} \tag{2.1}$$

2.2.2 Selective Laser Melting

Selective Laser Melting (SLM) is a widely used metallic additive manufacturing process [8]. A general schematic of the process is provided in Figure 2.7. An SLM Solutions 125 machine was used for the SLM printing.

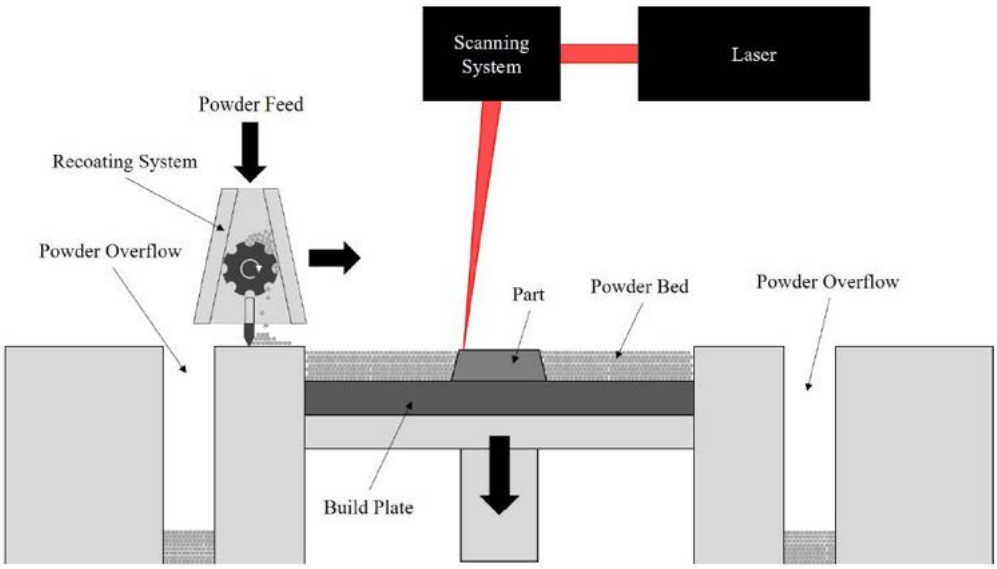

Figure 2.7: Selective Laser Melting diagram [15]

A layer of powder is spread using the recoating system. A laser, typically an IPG fiber laser, is rastered onto the powder layer in a preselected pattern,

selectively melting the powder in the desired pattern. The powder bed is lowered a distance equal to the desired layer thickness, a new layer of powder is spread, and the process repeats. User-controlled variables include scan speed, beam power, raster pattern, hatch spacing, and layer thickness. Volumetric energy density is often computed from these user-controlled variables to compare power-scan speed combinations (Equation 2.2) [8].

$$E_v = \frac{P}{vht} \tag{2.2}$$

2.3 Literature Review of Additively Manufactured Magnetic Materials

The field of additively manufactured magnetic materials is still widely unexplored. A variety of literature exists from multiple research groups, investigating printing both permanent and soft magnetic alloys. A myriad of additive processes are considered, from Fused-Deposition Modeling (FDM) and binder jet systems to Laser Engineered Net Shaping (LENS) and Selective Laser Melting (SLM)[16, 17, 18, 19].

2.3.1 Additively Manufactured Bonded Magnets

Bonded magnets are produced using powdered ferromagnetic alloy, usually NdFeB, with a polymer binder to join the powder particles together. Conventionally, these are then pressed into form through an injection molding process [20]. Whether produced with conventional or additive methods, the bonded magnets are formed below the material's Curie temperature, ensuring homogeneity in material domains. Typical bonded magnets show good isotropic properties, both magnetically and mechanically.

The first research group to extensively publish on the subject is Li, et al. [21]. Li contributed work in three fields: Big Area Additive Manufacturing (BAAM), binder jet process, and a review of additive manufacturing with respect to magnetic components.

The first publication delves into producing bonded permanent magnets using the BAAM process [22]. BAAM operates similar to a large-scale FDM process, where material is supplied in pellet form through a hopper, rather than the continuous filament of small-scale FDM. For this experiment, nylon pellets and NdFeB powder was extruded through the hopper. The resulting depositions consisted of 65% isotropic NdFeB powder and 35% polyamide (Nylon-12). NdFeB magnets are typically injection molded; a comparison between the traditional injection molded and BAAM magnets indicated similar density and hysteresis loops across the processes.

Li et al. also pursued bonded magnets generated through a binder jet additive process [17]. A commercial Ex-One printer was used to bond NdFeB powder into the suitable "green" magnet. The magnets were then infiltrated with NdCuCo or PrCuCo. The infiltrated magnets gave a higher intrinsic coercivity and a slight reduction in remanence. Li et al. propose that this is due to separation of the NdFeB magnetic grains, which is induced by the diffusion of the Nd or Pr rich (and Fe deficient) non-ferromagnetic phase.

2.3.2 Additively Manufactured Consolidated Magnets

Beyond bonded magnets, additional research groups have investigated methods to additively produce consolidated magnets. In conventional methods, consolidated magnets begin the manufacturing process similar to bonded magnets with an initial ferromagnetic powder pressed into a suitable shape. Unlike bonded magnets, these magnets are then sintered and densified [20]. Sintered magnets usually have higher coercivity and permeability values than bonded magnets. However, sintered magnets are anisotropic, limiting the possible shapes and applications [20].

Additively producing consolidated magnets varies from conventional methods. Magnetic alloyed powder is locally melted in layers, slowly building up the shape. The properties of additive manufactured parts are often compared to annealed properties. However, since the part is developed through local rapid solidification, the texture and magnetic domain alignment varies dramatically from conventional manufacturing.

Development of additively manufactured consolidated magnets is ongoing. Currently pursued alloys are mainly binary Fe alloys, which have less variance

between constituents than NdFeB magnets. Geng et al. developed Fe-Co LENS produced magnets and several groups are researching Fe-Ni alloys [18, 19, 23].

Geng et al. produced a comprehensive library of binary Fe-Co alloys of various compositions. The LENS system was utilized to vary deposition compositions from pure Fe to pure Co. The deposits were characterized using XRD and VSM and compared to current experimental data of conventionally produced Fe-Co alloys.

The main aim of the paper by Geng et al. was to show the capabilities of rapid characterization of a binary alloy. Both microstructurally and magnetically, the LENS-produced Fe-Co showed good agreement with data produced through conventional methods, with similar values of lattice parameters, saturation magnetization, and Curie temperature across all compositions [23].

Fe-Ni LENS Magnets

Mikler et al. utilized the LENS system to print binary Fe-Ni alloys. The research spans several publications, investigating Fe-Ni alloys, fabricated from elemental Ni and Fe powders [18, 24]. The papers developed correlations between processing parameters (scan speed and laser power) and final deposition microstructure and magnetic properties. Final deposits contained both face-centered cubic (FCC) and body-centered cubic (BCC) crystals.

Using EBSD, the researchers concluded that the FCC and BCC grains had a Nishiyama-Wasserman orientation relationship (N-W OR). The N-W orientation relationship is typically seen in BCC martensitic plate precipitates and rolled parent FCC austenite grains. Mikler et al. concluded that the BCC grains observered were likely a martensitic transformation occurring within the parent FCC grain. This transformation is stress and deformation induced and likely formed from thermal and residual stresses rather than energy input or solidification mechanisms [18]. In the follow-up paper, Mikler et al. noted that depositions made at higher scan speeds were FCC dominated, and at higher energy inputs, more BCC and higher saturation magnetization was observed [24]. A conference paper alluded to the potential application of functionally grading high entropy magnetic alloys using the LENS system. Results showed the coercivity and saturation magnetization dependency on

energy density and the subsequent FCC to BCC phase transition [25].

The final and most recent publication systematically investigated the impact of composition on saturation magnetization, coercivity, and microstructure for Fe-Ni and Fe-Co alloys produced with LENS. Fe30-Ni70, Fe40-Ni60, Fe55-Ni45, Fe60-Ni40, and Fe70-Ni30 were produced from elemental powder. The authors observed a monatomic increase to saturation magnetization as Fe content increased. The coercivity had an observed minimum at Fe40-Ni60. EBSD and KAM were performed on the samples, where it was shown that there was minimal lattice strain within the grains, only at grain boundaries [25].

Fe-Ni SLM Magnets

Research by Zhang et al. was performed on Fe70-Ni30 SLM deposits. The research group blended elemental Fe and Ni powder in a hopper, and then manufactured cylinders through the SLM process [19]. The researchers varied print speeds and laser power to develop correlations between the final deposit microstructure and magnetic properties. Final deposits were characterized using mainly XRD and VSM.

Zhang et al. concluded that the BCC phases were observed at faster scan speeds, while more FCC was observed at slower, higher energy density values. Comparing results with the Fe-Ni deposits produced through LENS, both the SLM and LENS processes show good agreement that faster scan speeds correlate with higher amounts of BCC phases [19]. A supplemental publication for the same samples described fine dendritic grains at the slower scan speeds and coarse grains were distributed within the fine grain matrix at higher scan speeds [26].

In a follow-up paper, a Fe20-Ni80 alloy was printed in a similar manner. VSM measurements showed that the SLM-produced magnets have a higher coercivity than those sintered or cold compacted. The researchers suggested that the SLM has a very fine grain structure, namely a single domain structure. The single domain structure has a higher coercivity than consolidated sintered structure where strong particle=particle interactions lead to self-demagnetization [27].

Shishkovsky and Saphronov considered the influence of laser fluence and

applied emf fields on final phase distributions [28]. Using a pre-alloyed Fe20-Ni80 powder, the SLM process produced mainly magnetic taenite (γ Fe, Ni) and awaruite ($FeNi_3$) phases. The researchers concluded that the optimal energy density required was 60 to 100 J/mm^2, which increased the phase transformation for intermetallic compounds. Moreover, when exposed to applied magnetic fields during the printing process, significantly more magnetite (Fe_3O_4) was formed.

Work published in late 2019 by Mazeeva et al. thoroughly investigated producing Fe50-Ni50 using SLM [29]. Beginning with a pre-alloyed gas-atomized powder, the group used only one set of printing parameters to produce samples, focusing the efforts on heat treatments. All samples investigated were produced with an EOSint M270 system at a laser power of 195 W and a scan speed of 800 mm/s. Heat treatments were in the ASTM recommended annealing region, 1125 °C to 1300 °C for 3 to 10 hours. EBSD showed minimal microstructural changes between the as-deposited and heat-treated condition, indicating the as-deposited structure is stable. Hardness testing indicated a reduction in residual stress after heat treatment, which lead to higher permeabilities and lower coercivities [29].

The final publication discussed considers the applications and implementation of additively manufactured soft magnetic components [30]. Yakout et al. produced motor stators out of a silicon steel alloy (Fe-6Si), Fe50-Ni50, and stainless steel (SS 430L) using pre-alloyed powder and an EOSint M280 system. Microstructure was not investigated, but printing parameters were optimized for relative density. The Fe50-Ni50, SS 430L, and a traditionally formed laminated stator were used for electrical analysis and testing. The iron losses, which combine the effects of eddy and hysteresis losses, ranged from 10 W (750 rpm) to 60 W (2500 rpm) for the additively manufactured stators. The laminated stator iron losses were below 10 W for that entire range. The results emphasize the importance of lamination to minimize eddy currents when developing motor components [30].

2.4 Fe-Ni System

Fe-Ni is chosen as the alloy system for this work, due to the manufacturability, magnetic properties, and accessibility. Fe50-Ni50, abbreviated as Fe50Ni

henceforth, was chosen for the fundamental research, as at the time of selection Fe50Ni had not been produced utilizing additive manufacturing [29].

From the *Journal of Phase Equilibria*, a phase diagram for the entirety of the Fe-Ni system is constructed and compared against experimental data [31]. A copy of this diagram is given in Figure 2.8.

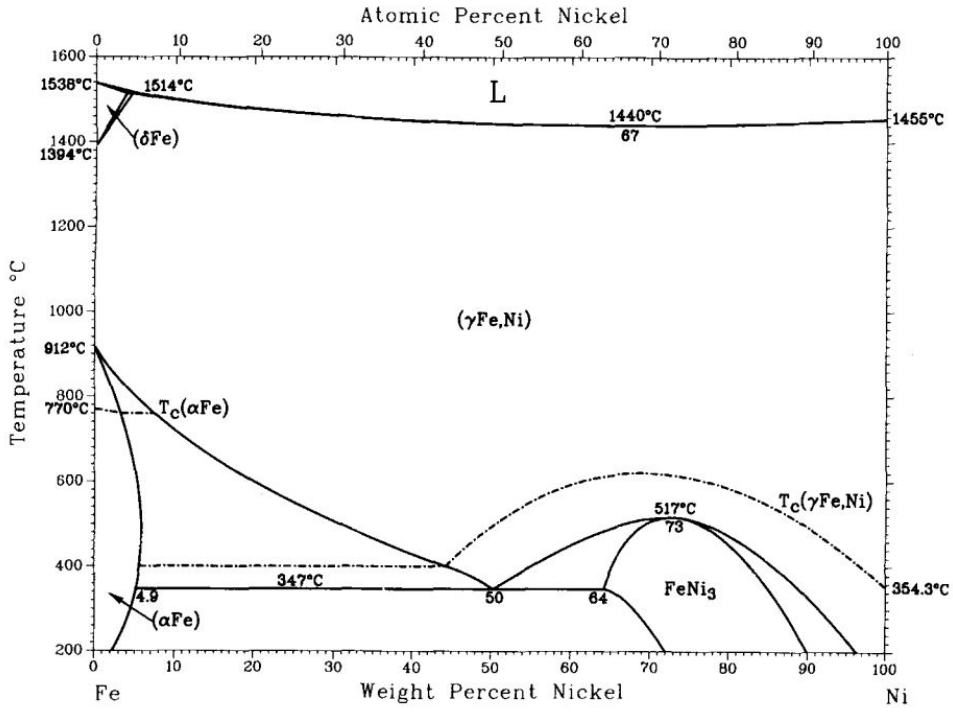

Figure 2.8: Fe-Ni Equilibrium Phase Diagram [31]

Within the phase diagram, the Curie line is indicated as a dashed line (T_C). Moreover, at Fe50Ni, the equilibrium phases consist of γ and $\gamma+\alpha$, depending on the temperature. Fe and Ni are completely soluble in one another, which allows for a wide range of potential compositions, with minimal risk of cracking or solute trapping. However, the phase diagram below the Curie temperature for Fe50Ni is still actively researched. Highlighting this, Figure 2.9 shows a proposed phase diagram from 1989, showing significantly more allotropes than Figure 2.8.

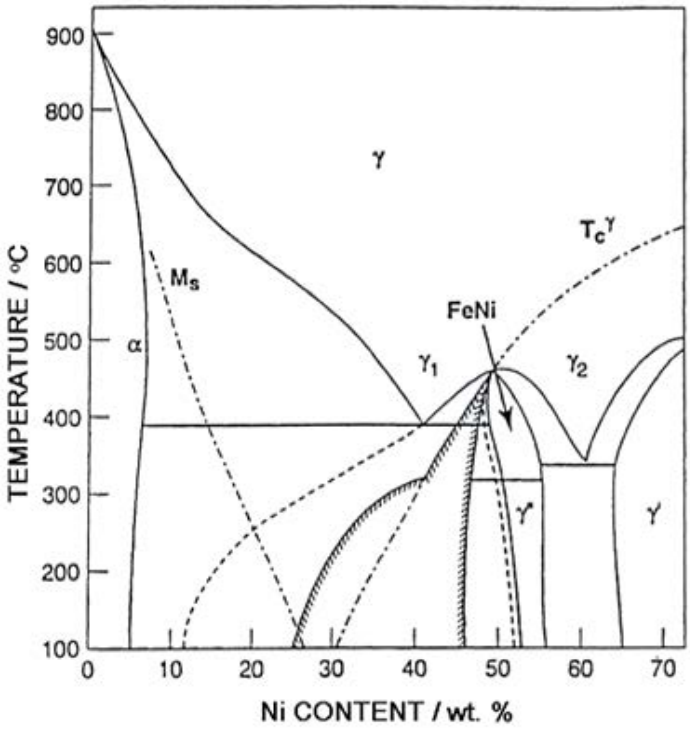

Figure 2.9: Fe-Ni low temperature phase diagram about Fe50Ni, showing multiple allotropes and phases at Fe-50Ni. [32, 33]

Much of this uncertainty is the result of the chemically ordered - disordered transition at Fe50Ni. Fe and Ni are similar enough to interchange atomic positions in metastable FCC. The FCC phase is a chemically disordered phase. For the ordered phase, the Fe and Ni atoms are arranged in monotomic layers, creating a slight tetragonal crystal shape is formed through the layer heights. The difference between the ordered and disordered phases is presented in Figure 2.10.

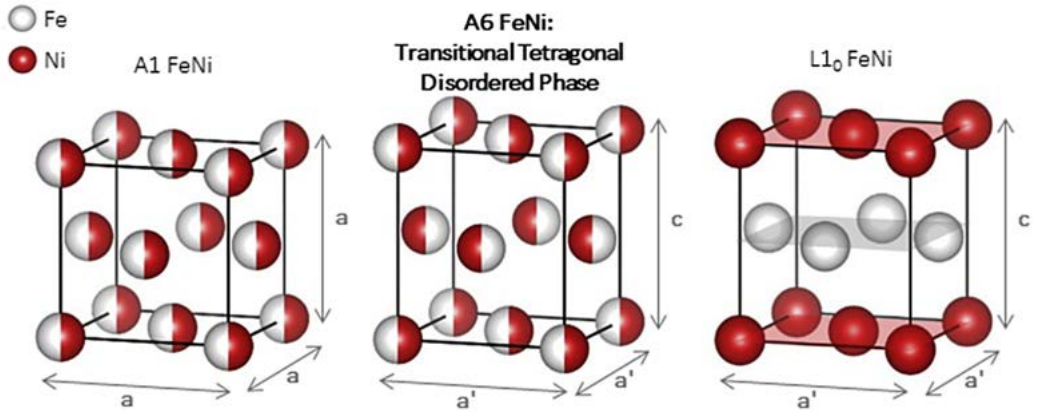

Figure 2.10: Potential crystal structures of Fe50Ni, showing disordered FCC, disordered tetragonal, and ordered tetragonal ($L1_0$) [34]

The ordered Fe50Ni is known as the $L1_0$ phase. The $L1_0$ phase, which is also called tetrataenite, has dramatically different magnetic properties than disordered Fe50Ni [32]. $L1_0$ has long range order, which generates hard magnetic properties that rival state-of-the-art rare earth magnets [35]. The $L1_0$ phase has coercivities around 1200 Oe, and BH_{max} = 42 MGOe [35]. However, due to extremely low atomic mobilities between Fe and Ni (1 atomic jump / 10000 years at 300°C), this phase has yet to be manufactured in bulk and has only been observed in meteorites [36]. Most recently, trace amounts of $L1_0$ were manufactured through the annealing of Fe50Ni amorphous ribbons [37]. However, reliable commercial manufacturing of $L1_0$ has still not been achieved.

2.4.1 Magnetic Properties of Disordered Fe-Ni

Binary Fe-Ni alloys have been characterized and used for magnetic applications since 1889 [38]. The Permalloy region, which spans from 30% to 90% Ni, was comprehensively characterized by Gustav Elmen in 1913. The Permalloy region yields remarkably high initial permeabilities, as high as $\mu_0 = 16000$ with heat treatment. The high permeability led to commercial applications in communication industries and for magnetic shielding [38].

The general magnetic property information for Fe-Ni is gathered from *Ferromagnetism* by Richard Bozorth [38]. Bozorth devotes Chapter 5 to the many

material properties of the Fe-Ni system. Magnetic properties plotted with respect to composition include saturation magnetization, lattice constant, permeability, and coercivity. The saturation magnetization phase diagram is reprinted from Bozorth in Figure 2.11.

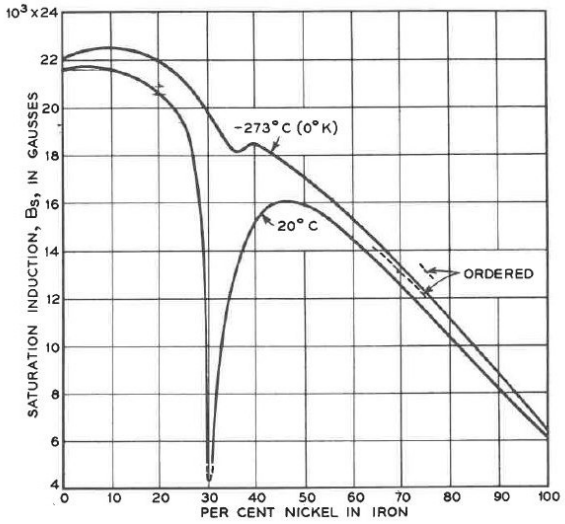

Figure 2.11: Fe-Ni saturation magnetization, showing a massive change at 30% Ni, where the system transitions from BCC to FCC. Also shown is the relative maximum at Fe-50Ni [38]

From Figure 2.11, there is a significant drop in magnetization at 30% Ni and a local maximum near 50% Ni. Moreover, there is a larger change in magnetization values about 50%; if the composition changes marginally in this region, the magnetic effects will be observable.

Figure 2.12 shows the coercivity dependence on composition. For 50% Ni, coercivity is expected to be 2.5 Oe. However, coercivity is an structure sensitive property and is reliant on grain size and texture in addition to phase diagram considerations.

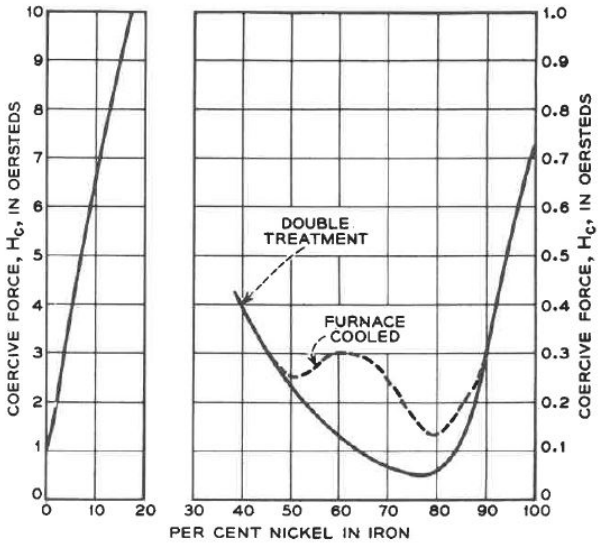

Figure 2.12: FeNi coercivity, which is approximately 2.5 Oe at Fe-50Ni, can be impacted by the cooling mechanisms [38]

For grains larger than ∼100 nm, the coercive field strength is proportional to the reciprocal grain diameter. Initially derived by Mager in 1952 to describe the grain boundary effects on coercivity, Equation 2.3 describes the coercive field strength (H_c) with respect to the wall energy γ_w, saturation polarization J_s, and grain diameter (d_k)[39].

$$H_c \approx 3\frac{\gamma_w}{J_s}\frac{1}{d_k} \tag{2.3}$$

Equation 2.3 was experimentally verified for Fe50Ni by Herzer in 1992. Figure 2.13 gives the results of the experiment, showing a linear relationship between the inverse of the grain size and coercivity.

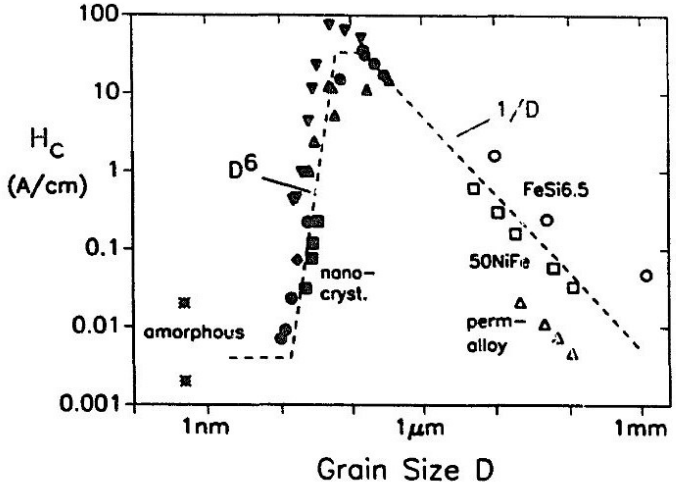

Figure 2.13: Fe-Ni experimental coercivity reprinted from Herzer et al. [40]. Coercivity H_c versus grain size for various soft magnetic metallic alloys. The data of the nanocrystalline material refer to (▲) FeNbSiB and (●) FeCuNbSiB [41], (♦) FeCuVSiB [42], (■) FeZrB [43], and (▼) FeCoZr [44]. Micron scale data obtained from Herzer et al. [40].

Texture also has a large effect on the structure sensitive magnetic properties of Fe-Ni. For BCC structures, <001> is considered the easy magnetization direction, while for FCC <111> is the easy direction. The impact of easy magnetization direction on hysteresis curves is demonstrated in Figure 2.14.

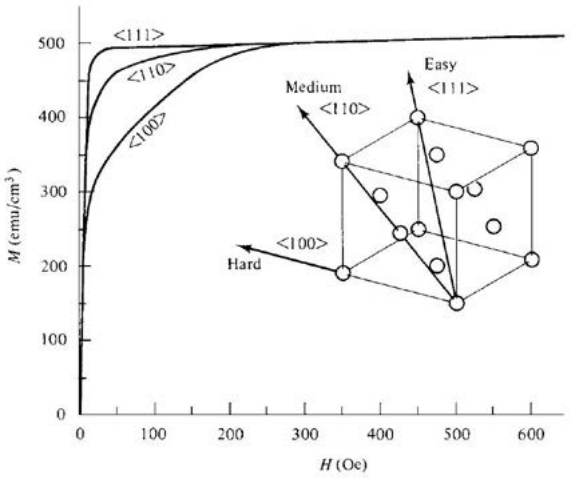

Figure 2.14: Easy magnetization direction for FCC Ni with texture effects on magnetization shown [5]

FCC and BCC share a medium magnetization direction of <110>. In 1934, Goss was the first to successfully create a large-scale textured Si-Fe which harnessed this medium direction. The Goss texture is shown in Figure 2.15. By cold rolling and applying both intermediate and final annealing, the "cube on edge" (110)[001] is formed through secondary recrystallization when grains selectively form to minimize surface energy [45].

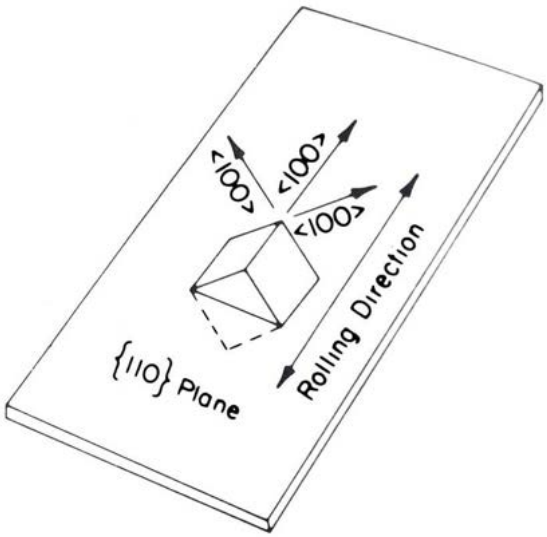

Figure 2.15: Goss texture demonstrated with cubic crystal and rolling direction labeled [45]

The Goss texture is observed in many additively manufactured structures [46, 47]. For FCC materials, the easy solidification direction is <100> [9]. The <100> grains will then preferentially grow in the direction of the highest thermal gradient, towards the moving heat source. Due to the localized motion of the heat source, final FCC additive parts often exhibit the Goss texture [46, 47]. The <100> grains grow vertically through the layers, towards the center of the melt pool. The vertical growth is perpendicular to the localized scan direction, forming the Goss texture [47]. Magnetically, an additively-produced FCC Goss texture allows for an applied magnetic field along the in-plane <111> easy and <110> medium magnetization direction, which yields more desirable soft magnetic properties than the <100> direction [5].

2.4.2 Traditionally Manufactured Fe-Ni

Some of the first applications for Fe-Ni alloys were in the communications industry in the 1900s, as a means of increasing inductance through transatlantic telegraphs [48]. This need for increased inductance, high permeability alloys spurred the creation of Permalloy. Elmen, a researcher of Bell Laboratory, discovered that alloys containing 30 to 90% Ni had much higher initial

permeabilities than Fe-Si steel when heat-treated [49]. Generally speaking, to achieve high permeabilities in Fe-Ni alloys, the alloy undergoes a two stage heat treatment, the first being hydrogen annealing and the second a thermomagnetic treatment [50]. The dry hydrogen anneal is performed at 1080 to 1400 °C, for 6 to 24 hours [38, 50]. This hydrogen annealing eliminates dislocations, promotes grain growth, and encourages secondary recrystallization [50]. Additionally, hydrogen annealing removes sulfur and carbon impurities [38]. Cooling rates range from 60 to 600 °C/hr, with no impact to final permeabilities [50]. The second stage of heat treatment is a thermomagnetic treatment, which applies a small magnetic field (≈10 Oe) below the Curie temperature to induce anisotropy, creating an induced easy axis [50].

This two stage heat treatment process dramatically increases permeabilites from ∼15000 to ∼80000 and promotes high permeability and low coercivity with an anisotropic microstructure with low residual stress and defects [38, 50].

2.4.3 Additively Manufactured Fe-Ni

From Section 2.3, much of the work done to additively manufacture magnetic materials utilizes binary Fe material systems, likely due to material availability and cost. The directed energy deposition and powder-bed fusion processes, which occur well above the material's Curie temperature, often use Fe-Ni or Fe-Co. Fe and Ni are considered to be metallurgically compatible, with similar densities and laser adsorbtion levels and no galvanic couple formation [51]. Moreover, the previous work with Fe-Ni ensures a valuable verification method for future depositions.

Two previous papers, summarized in Section 2.3.2, deposited Fe-50Ni using SLM [29, 30]. The most successful deposition parameters, along with reported results, are summarized in Table 2.1.

Table 2.1: Successful deposition parameters and results compiled from published literature on the selective laser melting of Fe-50Ni

	As-Built [29]	**Heat-Treated** (1300 °C, 6 hr) [29]	**As-Built** [30]
Deposition Parameters (Laser Power, Scan Speed, Layer Height, Hatch Spacing)	195 W, 800 mm/s, 40 µm, 100 µm	195 W, 800 mm/s, 40 µm, 100 µm	200 W, 600 mm/s, 40 µm, 100 µm
Coercivity (H_c)	200 A/m	100 A/m	–
Permeability (μ_{max})	1000	5000	–
Grain size	10-100 µm	10-100 µm	–
Density	8.14 ±0.01 g/cm^3	8.14 ±0.01 g/cm^3	8.20 g/cm^3
Iron (Core) Loss	–	–	10 W/800 RPM - 60 W / 1500 RPM

Chapter 3
Methodology

Samples were produced from two additive manufacturing methods, Electron Beam Free Form Fabrication (EBF^3) and Selective Laser Melting (SLM). Both of the processes can produce high quality metallic structures but the thermal history, deposition rates, starting materials, and final deposition build attributes vary significantly. Section 2.2 underscores the differences between these processes. The process parameters, manipulated variables, and iterations for SLM and EBF^3 are explained along with sample preparation.

Chemical and microstructural characterization was performed with optical and scanning electron microscopy (SEM), electron dispersive x-ray spectroscopy (EDS), and electron backscatter diffraction (EBSD). Magnetic measurements were performed with vibrating sample magnetometer (VSM).

3.1 Base Materials

Both wire and powder forms of the Fe50Ni alloy are analyzed and utilized. Welding wire 1.6 mm in diameter was purchased from Alloy Wire International [52]. The wire (Alloy 52) was fabricated according to ASTM F30 - 96 *Standard Specification for Iron-Nickel Sealing Alloys* [53]. The wire has a commercial application as welding wire for sealing glass to metal.

Gas-atomized Fe50Ni powder, ranging in size from 15 to 45 μm, was purchased from Sandvik Osprey Powders [54]. The powder was atomized in a nitrogen environment, bottled and shipped in argon. In the lab setting, the powder was handled in an argon environment to minimize oxidation effects. Powders for microscopy and VSM were exposed to atmosphere during sample preparation. Both vendors provided X-ray fluorescence (XRF) chemical analysis for the materials. The final vendor chemistries of the materials are given in Table 3.1.

Table 3.1: XRF chemical analysis (wt%) of base wire and powder material supplied by vendors

Element	Wire	Powder
Fe	Bal	Bal
Ni	50.60000	48.70
Mn	0.44000	0.36
Si	0.20000	0.24
Al	0.01000	–
C	0.00300	–
Cr	0.01000	–
P	<0.00200	–
S	0.00200	–

Metallurgical analysis was performed to confirm that the material met vendor and standard specifications. The powder and wire were prepared and characterized in the manner detailed in Sections 3.4 and 3.5. Composition was confirmed though EDS and structure was inspected through optical imaging and EBSD.

Samples of the wire and the powder were also used to gather baseline magnetic responses for the materials using the procedure outlined in Section 3.5.2.

3.2 EBF^3 Depositions

The EBF^3 process at NASA Langley Research Center was utilized to synthesize a total of 80 depositions on 8 separate build (base) plates. Images of the EBF^3 build chamber are provided in Figure 3.1. From this deposition array, 51 samples were characterized in this research program.

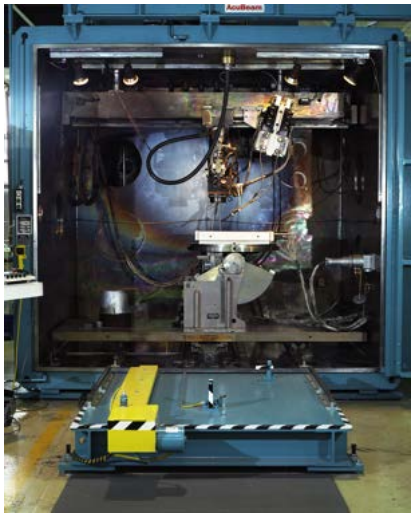

(a) Full EBF^3 chamber

(b) Close-up of deposition area

Figure 3.1: EBF^3 chamber, with open door shown in 3.1a. The large blue box is the vacuum chamber, which houses the electron beam gun (top center cylinder), wire feeding system (suspended to the upper right), and build platen (middle, floor of chamber). EBF^3 has a 60 in. x 24 in. x 24 in build envelope. 3.1b shows the first three build plates after deposition (8-10) as viewed when loaded into the build platen. The wire feed nozzle is visible in the top quarter of the photo.

The base plates are 1/2" thick A-36 steel plate, 6" x 12". Each plate was designed to allow for 10 depositions, 4.5" long. The diagram in Figure 3.2 shows the location and spacing of each of the depositions.

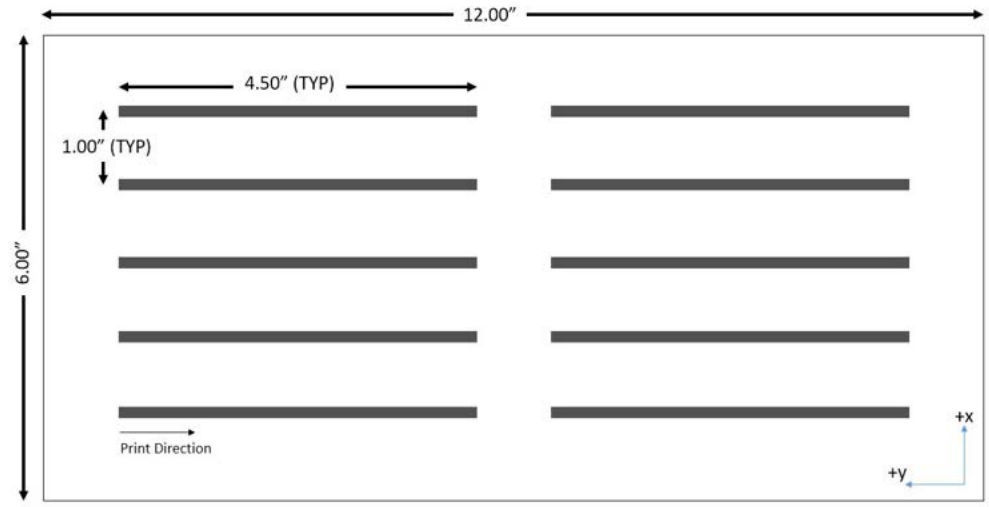

Figure 3.2: EBF^3 deposit locations, shown as grey rectangles, relative to baseplate dimensions. Printer coordinates are provided in the bottom right corner.

In comparing EBF^3 and SLM, both require tight control on the process parameters. However, the impact of variance in deposition quality is more pronounced for the EBF^3 depositions. For this reason, many times when the depositions fail due to poorly optimized parameters, the deposition is not completed or samples are not able to be removed from the baseplate, accounting for the uncharacterized depositions.

The first plate of successful depositions, Plate 8, was used as a screening tool to refine parameter testing for future depositions. The printing parameters varied systematically around a set of base parameters obtained previously through visual inspection and engineering judgment. Translation speed, wire feed rate, beam current, and pause time are isolated to determine individual variable effects on magnetic response. The final plate, with 9 successful deposits and changed variables labeled, is shown in Figure 3.3.

Figure 3.3: EBF^3 Plate 8 depositions systematically varied wire feed rate, beam current, translation speed, and pause time. Final depositions showed generally minimal impact to sample exterior appearance, though decreasing wire feed rate to 30 inches per minute (ipm) showed some oscillations in deposition cross-section and uneven thicknesses.

Three deposits, including the base parameter set, for each variable were run. For example, the translation speed was varied between 15, 20, and 30 inches per minute (ipm) while keeping all other parameters the same. The changes, as well as a the base parameters, are summarized in Table 3.2.

Table 3.2: EBF^3 initial deposition parameter ranges

Variable	Base Parameters	Ranges
Accelerating Voltage (kV)	30	30-40
Beam Current (mA)	85	75-100
Translation Speed (ipm)	20	15-30
Wire Feed Rate (ipm)	40	30-95
Pause Time (s)	120	60-180
Beam Focus	318	318

Plate 9 was deposited simultaneously with Plate 8 to investigate the impact

of beam current on magnetic response. Plates 10 to 15 were deposited after general characterization of Plates 8 and 9. These plates looked at more finely tuned impacts of accelerating voltage, beam current, beam focus, and translation speed. For a complete summary of parameters used for each deposition, see Appendix A.

The ranges used for each parameter set are given in Table 3.3.

Table 3.3: EBF^3 total deposition parameter ranges

Variable	Base Parameters	Ranges
Accelerating Voltage (kV)	30	25-40
Beam Current (mA)	85	60-120
Translation Speed (ipm)	20	10-55
Wire Feed Rate (ipm)	40	30-95
Pause Time (s)	120	60-180
Beam Focus	318	313-333

3.3 SLM Depositions

To contrast the cooling rates and microstructures seen using EBF^3, 36 5 mm cube samples were printed using a SLM Solutions model 125 printer at UVA (Figure 3.4).

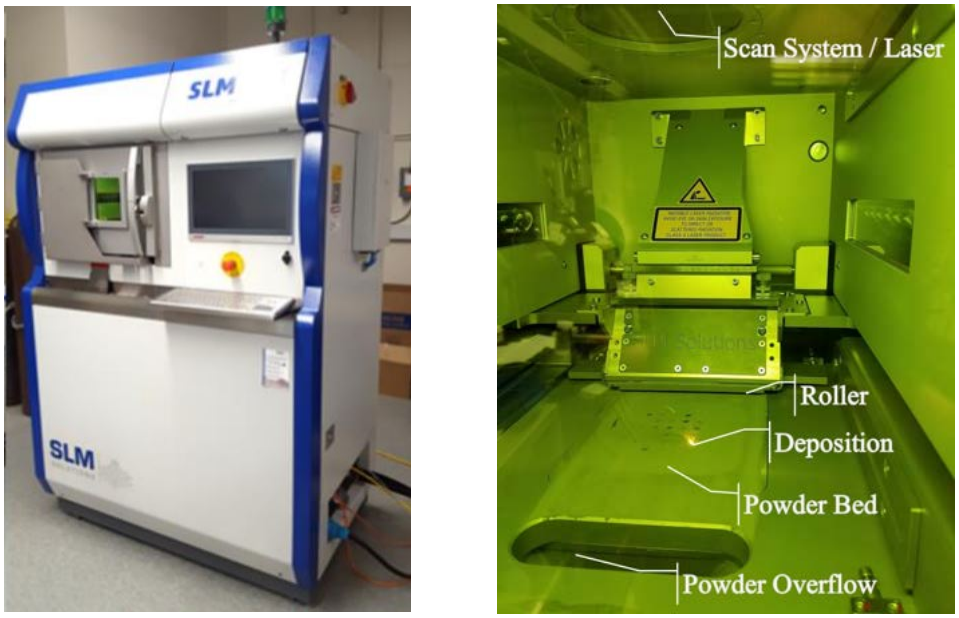

(a) SLM125 located at University of Virginia **(b)** Close-up of chamber interior

Figure 3.4: SLM125 used to deposit samples for this work. Shown in 3.4a is the full printer, and 3.4b shows the chamber mid-deposition.

Using 12 unique parameter combinations, triplicates of each parameter set are made using available literature for Fe70-30Ni as a starting point [19]. Thermal conductivity and melting temperature of Fe70-Ni30 and Fe50Ni were checked for similarity [31, 55].

Only scan speed and laser power were varied between the 36 samples, with all other parameters held constant. The laser hatch spacing was 120 µm, the layer height was 30µm, and the hatch spacing was rotated 15° every layer (167 layers were deposited). The print pattern was a perimeter box, with a straight line fill pattern in alternating scan directions from perimeter edge to edge. Table 3.4 lists the power-scan speed combinations used and the resulting volumetric energy.

Table 3.4: SLM Laser Power and Scan Speed processing parameter combinations

	Laser Power (W)	**Scan Speed (m/s)**	**Volumetric Energy (J/mm^3)**
1	50	0.1	138.89
2	50	0.2	69.44
3	50	0.4	34.72
4	50	0.8	17.36
5	80	0.1	222.22
6	80	0.2	111.11
7	80	0.4	55.56
8	80	0.8	27.78
9	80	1.6	13.89
10	110	0.4	76.39
11	110	0.8	38.19
12	110	1.6	19.10

The SLM samples were deposited on a 1" thick A36 steel base plate (123mm x 123mm). The samples are in a 6x6 array on the build plate. The parameter set assignment and array are depicted in Figure 3.5.

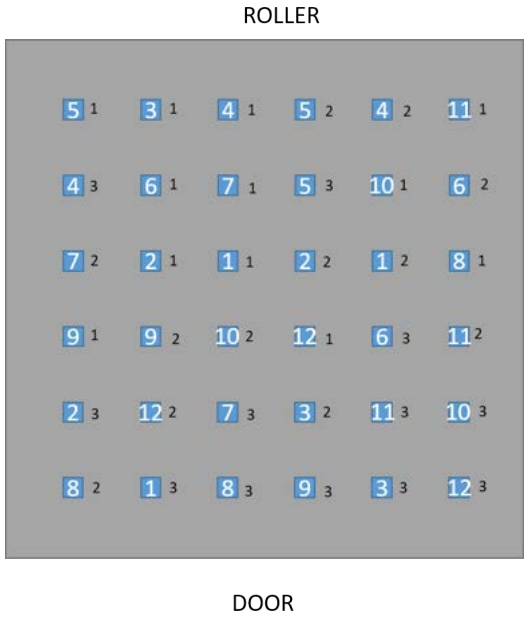

Figure 3.5: SLM build layout on base plate. The word "Door" indicates the loading door and viewing window perspective that the photo in Figure 3.4b was taken from. The home location of the powder spreading "Roller" is also indicated. The parameter set is indicated by the white label and the triplicate is a black label. Samples are randomized to remove any unintentional build chamber location bias.

The printed SLM samples are shown in Figure 3.6.

Figure 3.6: The SLM samples after deposition, prior to removal from the base plate, with the same orientation in Figure 3.5. A 6" ruler is provided for scale.

3.4 Sample Preparation

The subsequent samples are obtained using a combination of waterjet cutting and wire EDM. Preparation for both magnetic and crystallographic characterization is detailed.

Samples were obtained from depositions utilizing a variety of sources, including precision water jet, wire electrical discharge machine (EDM), and a Buehler slow-speed saw. For EBF^3 depositions, samples are removed at least 1" inward from the deposition starting and ending locations. Figure 3.7 shows a sample cut plan for the standard EBF^3 deposits with water jet cuts. For each EBF^3 deposit, a metallurgical sample perpendicular to the deposition direction, a sample along the centerline, and a sample for magnetic characterization is needed. The SLM samples were removed from the baseplate with EDM.

Figure 3.7: Plate 9 deposits after water jet cutting. Due to water exposure during the cutting process, as well as general humidity during storage, the cut locations exhibit surface level rust. Rust is manually polished away before characterization and has no impact on reported results.

In order to simplify the magnetic measurement process, the samples measured must be rectangular prisms approximately 1 gram or less in weight.

For the EBF^3 samples, excess material flash and surface roughness was removed with a combination of the slow-speed saw and mechanical grinding using 400 grit SiC paper. The final rectangular dimensions are dependent on the initial deposit height and width.

For the SLM samples, measurements were taken from the whole sample cube with as-deposited surface roughness. Magnetic measurements were completed before the cubes are sectioned for metallurgical analysis. The rectangular sample dimensions for both EBF^3 and SLM are presented in Appendix B.

The length, width, and height of each VSM specimen were measured with a Mitutoyo digital caliper, accurate to ± 0.005 mm. Each specimen was weighed using a precision scale with accuracy ± 0.005 mg.

Table 3.5: EBSD polishing methodology for FeNi samples

Grit	**Platen Speed (RPM)**	**Platen Direction**	**Sample Mass (g)**	**Sample Deflection (mm)**	**Polishing Time (min)**
600 SiC	125	CW	300	0.050	until flat
1200 SiC	125	CCW	200	0.045	8
3 μm Metadi slurry	75	CW	200	0.045	10
1 μm Metadi slurry	75	CCW	100	0.045	15
OPS	50	CW	50	0.035	80

For the EBF^3 deposits, excess baseplate material was removed with the slow speed saw on the transverse and perpendicular cross-sections. The SLM cubes were sectioned in half using a slow-speed saw. Specimens for optical characterization were hot mounted with Buehler black phenolic powder using a Buehler Pneumet I Mounting Press. Otherwise samples were attached to a metallic mount with adhesive.

For Electron Backscatter Diffraction (EBSD) analysis, the samples were mechanically polished using the Allied MultiPrep Micro-Polishing System, with a series of SiC paper and diamond Metadi suspension slurries with nylon polishing pads. The full specifications, including time, mass, and polishing compound are given in Table 3.5.

For all other metallurgical analysis, samples were prepared by hand polishing using a Pace Technologies NANO 1200T polisher, or automatically on an Allied METPREP 4 Grinder/Polisher with a Power Head. The samples were ground flat with SiC low grit paper (240 grit) and then polished to an optical finish using a series of SiC grit papers (400, 600, 800, and 1200). All samples were finished using Buehler MasterPrep 0.05 μm alumina suspension.

For etched samples, etching was performed according to the procedures outlined in *ASM Metals Handbook 9* and *ASTM E407-07* [56, 57]. An enchant of $FeCl_3$ and HCl is swabbed on the polished surface for 20 seconds, then rinsed with water and methanol. The etchant results in etch pits on (110)[001] (cube on edge) texture, showing the general structure [56].

3.5 Sample Characterization

In order to effectively connect process, structure, and properties in this work, a number of measurements on both microstructure and magnetic response were performed.

3.5.1 Metallurgical Characterization

Metallurgical characterization was performed to evaluate composition, microstructure, texture, and morphology. Micrographs were recorded by both optical microscopy (OM) and scanning electron microscopy (SEM). Optical microscopy was performed on a Leica MeF4 inverted microscope in both bright and polarized modes. Polarized light micrographs were used to obtain grain size for the non-equiaxed structures, using the process detailed in *ASTM E112* [58].

A Hitachi S-3700N SEM was used for all electron microscopy. This instrument was equipped with secondary, backscatter, electron backscatter diffraction (EDAX EBSD), and energy dispersive x-spectroscopy (EDS)detectors (Oxford Instruments).Post-processing was performed with AZtec software on the EDS data. Chemical analysis data for composition was acquired semi-quantitatively.

EBSD was used to determine the phase and orientation of a grain, which also gives indication of grain morphology and size. For this work, the Hitachi S-3700N SEM was used with an EDAX EBSD detector. The sample was mounted at a 70 ° angle with respect to the horizontal plane, with the electron beam set to 20 kV and 90 mA. A working distance of approximately 25 mm is used. The Kikuchi patterns were recorded using AZtec software. For EBF^3 samples, a step size of 12 µm is used, while a step size of 2.5 µm is used for SLM samples. Post-processing and evaluation was performed using OIM$^{\text{TM}}$ software.

The average grain diameter can be computed one of two ways in post-processing: average number and average area. The grain diameter for an individual grain is $2\sqrt{A}/\pi$, where A is the area of the grain. For number averaged, the individual diameters are averaged using Equation 3.1, where N

is the total number of grains and v_i is the value of the parameter of interest (diameter) for grain i.

$$\bar{v} = \frac{1}{N} \sum_{i=1}^{N} v_i \tag{3.1}$$

Equation 3.2 is for grain area-averaged values, where A_i is the area of an individual grain. Generally, area averaged values are better descriptors for non-equiaxed microstructures [59].

$$\bar{v} = \frac{\sum_{i=1}^{N} A_i v_i}{\sum_{i=1}^{N} A_i} \tag{3.2}$$

EBSD also provides a measure of texture. Multiples of Uniform Density (MUD) values are used in conjunction with a pole plot, determining how similarly grains are oriented. Generally speaking, a MUD value of 1 is randomly distributed, while higher values show stronger texture [59].

To confirm phase identification and give some indication to lattice parameters and residual stresses, XRD was performed with a Rigaku Diffractometer with a Cu tube ($\lambda = 1.5405$ Å). The scan was performed from 35 to 99 degrees (2θ), with a step scan mode with a 0.84 sec scan speed (step = 0.0660°). To reduce florescence and noise, the collection occurred in parallel beam mode, with a Soller slit (5°) for the receiving slit, and a parallel slit analyzer (PSA 0.5°) for the receiving optical device.

3.5.2 Magnetic Characterization

Saturation magnetization, coercivity, initial and relative permeability, and hysteresis loss were measured and evaluated for the EBF^3 and SLM samples.

All magnetic measurements were taken using a Lakeshore 7300 Vibrating Sample Magnetometer (VSM). The VSM is capable of generating a magnetic field of 10,000 Oe. The stability for the output is ±0.05% of the emu field range [60].

VSM operates by measuring the flux change in a coil when a magnetized sample is vibrated near it. This flux change is a measurement of the total magnetic flux density (B), which is a combination of both the internal magnetization and demagnetizing field. In order to have an accurate measurement for the material magnetization and not the demagnetizing field, corrections for the shape must be taken into account. The effect of demagnetization is shown in Figure 3.8.

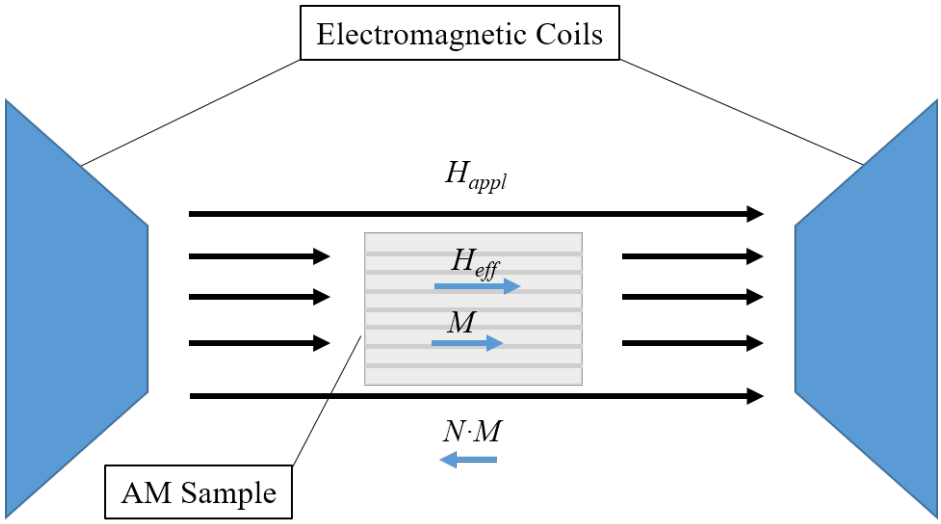

Figure 3.8: Diagram depicting VSM operation with demagnetizing effects. The externally applied magnetic field is indicated in black, while the sample response effects are indicated in blue. To demonstrate the orientation of the additive samples evaluated, grey lines are drawn on the sample to indicate layers. The build direction is oriented vertically, with the translation speed (EBF^3) or roller direction (SLM) oriented parallel to the applied magnetic field.

Quantitatively, the demagnetization effect changes as the applied magnetic field and the internal magnetization of a sample change. Equation 3.3 shows the relationship between the internal effective magnetic field (H), the externally applied field (H_{appl}), magnetization (M) and demagnetization factor (N).

$$H_{eff} = H_{appl} - N \cdot M \tag{3.3}$$

Demagnetization Factors

Demagnetization factors arise from the morphology of a magnetic specimen. For the additively manufactured samples, this comes from two sources: shape and porosity.

The shape demagnetization factor varies for each sample depending on the length, width, and height of the rectangular prism. The N_d demagnetizing factor for rectangular prisms is analytically determined by Chen, et al [61, 62]. A schematic showing rectangular dimensions relative to the applied magnetic field (H_a) is provided in Figure 3.9. The appropriate shape demagnetization factor is determined by double interpolation using the ratios of $c/\sqrt{ab}$ and a/b. The analytic demagnetization factors are printed in the chart in Figure 3.9. For a perfect cube, $c/\sqrt{ab} = 1$, $a/b = 1$, and $N_d = 0.27445$.

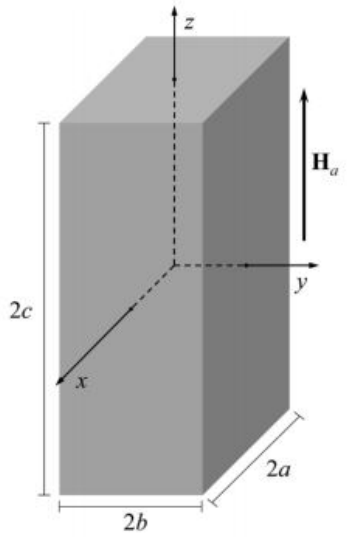

$c/\sqrt{ab}$	a/b=1	a/b=2	a/b=4
0.7	0.38505	0.3713	0.33455
1	0.27445	0.26669	0.24517
1.5	0.19882	0.19283	0.17665
2	0.15329	0.14874	0.13615

Figure 3.9: Rectangular demagnetization factors

The other consideration for demagnetization factors is porosity. Porosity can be though of as non-magnetic inclusions, which inhibit domain wall movement [5]. Several publications propose methods for addressing and removing the influence of porosity in magnetic materials [63, 64, 65].

For this work, the contribution of porosity to the total demagnetization

factor will only be considered for the powdered base material. Assuming a randomly packed spherical particle powder, the total demagnetization factor can be determined with Equation 3.4, where N is the total demagetization factor, f is the relative density (packing fraction), and N_d is the shape demagnetization factor of the powder sample [63]. Porosity is large concern for additive manufacturing, particularly SLM [8]. Since the processing parameters generate the porosity, it would be errant to remove the effects of porosity from the resulting measurements. The total demagnetization factors for each VSM sample, along with sample dimensions, are presented in Appendix B.

$$N = \frac{1}{3} + f\left(N_d - \frac{1}{3}\right) \tag{3.4}$$

Hysteresis Loops

The main method of magnetic measurement is hysteresis loops. The VSM was run with an applied field from $\pm 10^3$ Oe. The VSM has an output stability less than 0.05%, so measurements are stable within ± 5 emu, with an absolute accuracy better than 2% of the reading. With a theoretical saturation magnetization of 154 emu/g, error for Fe50Ni is expected to be ± 3 emu/g [38, 60]. The time constant is 100 ms, with a hypersine distribution of 120 points. The VSM collects data in units of Oe (independent variable, applied field) and emu (dependent variable, internal magnetization). The data is adjusted to remove the influence of shape and mass, through the demagnetization factor in Equation 3.3 and the mass influence in 3.5. Equation 3.5 determines the mass magnetization (σ) in units of emu/g, where m_{moment} is the magnetic moment (emu), and m is sample mass in grams.

$$\sigma = \frac{m_{moment}}{m} \tag{3.5}$$

From the corrected hysteresis loops, coercivity, saturation magnetization, hysteresis loss, and a permeability estimate were computed using a MATLAB script.

The hysteresis loop obtained for EBF^3 sample 8-1 is shown in Figure 3.10 to graphically demonstrate how the magnetic properties are obtained. The

resulting loop and magnetic properties are discussed further in Chapter 4.

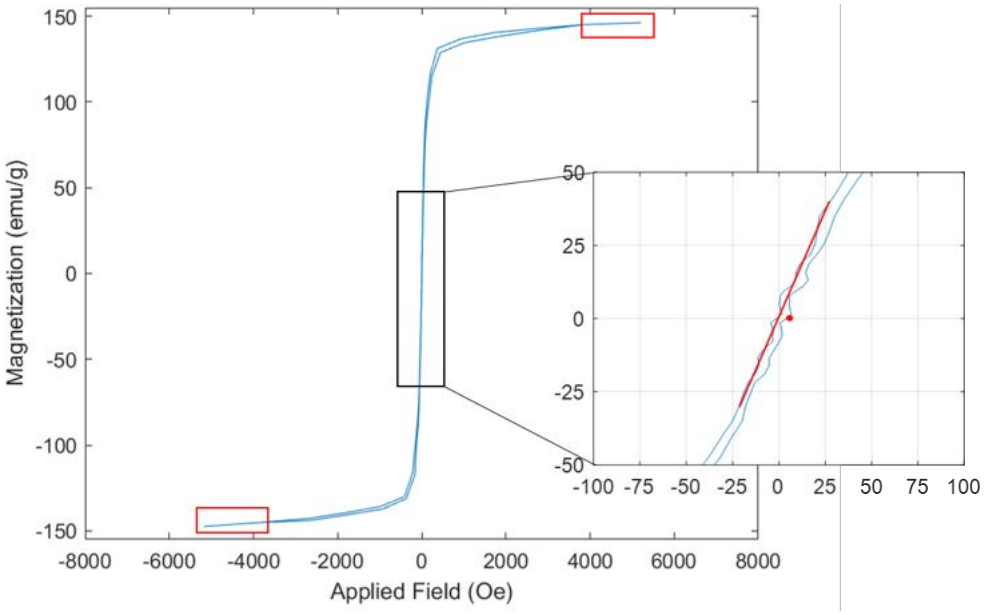

Figure 3.10: Hysteresis loop of sample 8-1 with magnetic properties labeled

Saturation magnetization was obtained by averaging the intrinsic magnetization values from when the applied field has a magnitude greater than 3500 Oe (averaged over 6 to 10 data points). The multi-point averaged saturation magnetization mitigates some magnetostriction effects and provides a more robust measurement than a single final point. The red box in Figure 3.10 indicates the positive points used for the average. The absolute values of the negative points were also included in the saturation magnetization average.

The area enclosed by the curve was considered hysteresis loss per cycle. Mathematically, the hysteresis loss is considered work and can be determined by Equation 3.6, where W is energy loss, H is the applied field, and dM is the incremental change to the magnetization.

$$W = \int_0^M H dM \tag{3.6}$$

The area was easily computed by a built-in MATLAB^{TM} function, 'polyarea',

in units of erg/g. For literature comparison, the area was multiplied by 10^{-7} to determine loss in J/g.

For coercivity and a permeability estimate, two lines of best fit are determined about the x-intercepts for -50<H<50. The line for the demagnetization curve is indicated in the inset of Figure 3.10, and a matching one is computed for the remagnetization side. The x-intercepts were assumed to be the coercivity, and the absolute values of the x-intercepts were averaged for the reported coercivity value. Variance was obtained for each slope and x-intercept using the MATLAB^{TM} function 'fit', and average variance and standard deviation for permeability and coercivity was determined using pooled variance.

Permeability was approximated as the slope of the line of best fit. The slope is an approximation of permeability, which underestimates the value. Maximum permeability is the maximum slope from the origin to the tangent of the initial magnetic flux curve, which will always be greater than the slope of the line of best fit [7]. To convert from intrinsic magnetization (M) to total magnetic flux (B), Equation 3.7 is used, where $M = \sigma\rho$, ρ is the density, and σ is the mass magnetization in emu/g. Permeability is unitless, as B and H have the same base units.

$$\frac{B}{H} = 4\pi\frac{\sigma}{H}\rho + 1 \tag{3.7}$$

Initial Magnetization Curves

To determine initial and maximum permeabilities, initial magnetization data was collected for a small subset of samples. The samples were subjected to a demagnetization process on the VSM, which applies alternating magnetic fields until the sample has zero internal magnetization.

A secondary process was then performed on the sample, applying a magnetic field slowly from 0 Oe to 10,000 Oe in one direction. This gives the initial magnetization curve as the sample moves from no internal magnetization to saturation. Permeability is typically reported as the initial magnetization slope from the origin (μ_{init}) or the maximum tangent slope from the origin to a point on the initial magnetization curve (μ_{max}) [5]. Figure 3.11 shows the

shape-corrected initial magnetization curve for EBF^3 sample 8-1, as well as the raw data from the VSM near the origin.

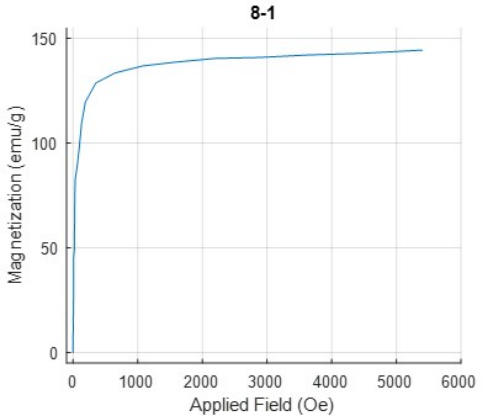

(a) Initial magnetization curve for EBF^3 sample 8-1

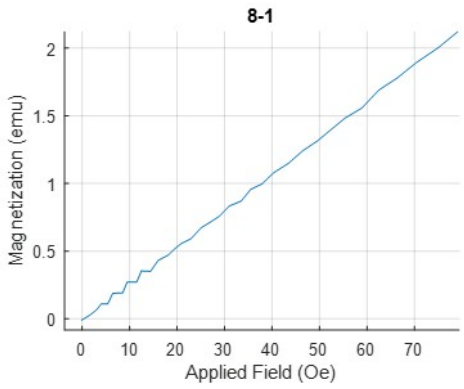

(b) Close-up of origin of EBF^3 8-1 magnetization curve

Figure 3.11

The initial magnetization curve for 8-1 was at the scale of machine resolution, with the origin at 0 Oe, 7.4^{-3} emu. The data was collected with 1 second time constant. The minimum viable increment of ΔH, 1 Oe, was used. Based on the plots obtained in Figure 3.11, there is no discernible difference in slope through the entirety of the initial magnetization curve, and the curve is a linear line until the sample approaches saturation. Since it is known that the initial magnetization curve must be enclosed in the hysteresis loop, it can be concluded that the hysteresis loop slope can be used as an underestimated proxy for the permeability.

3.6 Data Analysis and Verification

To derive relationships between processing and properties, various statistical methods were utilized. In addition to drawing conclusions from experimental data and statistics, computational Finite Element Analysis (FEA) was performed to provide support and verification for experimental results.

3.6.1 Statistical Analysis

Histograms were used for visualizing distributions. Pearson correlation coefficients were determined between input machine parameters and output magnetic measurements. Pearson correlation coefficients are a standard method of determining correlation, assuming linear relationships between the two variables. The coefficients are computed by Equation 3.8, where $Cov(X, Y)$ is the covariance of each X, Y pair, and s_x^2, s_y^2 are sample variances for X, Y.

$$r = \frac{Cov(X, Y)}{\sqrt{s_x^2 s_y^2}} \tag{3.8}$$

In order to address potential non-linear relationships between variables, known relationships for energy density and power density were determined from the input data. To account for outliers, any sample with an R^2 <0.7 for a line of best fit used to determine permeability and coercivity was excluded from the correlation determination.

Pearson correlation coefficients range from -1 to 1. The negative sign indicates a positive or negative correlation, while the magnitude indicates the strength of the correlation. Table 3.6 gives descriptors for each magnitude range [66].

Table 3.6: Pearson correlation coefficient values and ranges [66]

Magnitude of Correlation Coefficient	Description
1.0	Perfect Association
0.8 - 1.0	Very Strong Association
0.6 - 0.8	Strong Association
0.4 - 0.6	Moderate Association
0.2 - 0.4	Weak Association
0.0 - 0.2	Very Weak to No Association

3.6.2 Computational Modeling and Verification

A 3D transient thermal solidification finite element model was created in Sierra Mechanics to simulate a single track pass of the energy source. This

was simulated for three parameter cases for SLM deposits and one EBF[3] case. The thermal model provides estimations for the melt pool geometry, maximum cooling rates, and temperature gradients.

Governing Equation

The main equation for these simulations is the heat diffusion equation at $T(x,t)$, given in Equation 3.9. $T(x,t)$ is the temperature of a location x at time t.

$$\rho c_p \frac{\partial T}{\partial t} - \nabla \cdot (k \nabla T) = S + q_L \tag{3.9}$$

For Equation 3.9, ρ is the density, c_p is the specific heat, k is the thermal conductivity, and q_L is the applied heat source. S is the phase change source term, given by Equation 3.10, where L_f is the latent heat of fusion.

$$S = \rho L_f \frac{\partial f_L}{\partial t} \tag{3.10}$$

Material Properties

The material properties were obtained from a number of online sources, and are given in Table 3.7.

Table 3.7: Fe50Ni thermal properties collected for use in solidification modeling

Physical Property	Units	Value	Reference
Liquidus temperature (T_L)	K	1693	[67]
Solidus temperature (T_S)	K	1643	[67]
Latent heat of fusion (L_f)	Jg^{-1}	270	[67]
Absorptivity (A)		0.32	[68]
Solid specific heat (c_p)	$Jkg^{-1}K^{-1}$	$\begin{cases}(2E-6)T^{-3}-(3E-3)T^2+1.7T+136.3 & T<778K\\(1.1E-3)T^2-2.5926T+1997 & 778\leq T\leq 1693\end{cases}$	[69]
Liquid specific heat (c_p)	$Jkg^{-1}K^{-1}$	789.76	[70]
Solid thermal conductivity (k)	$Wm^{-1}K^{-1}$	$(5E-3)T+19.18$	[71]
Liquid thermal conductivity (k)	$Wm^{-1}K^{-1}$	28.86	[70]
Solid density (ρ)	kgm^{-3}	8250	[67]
Liquid density (ρ)	kgm^{-3}	7370	[72]

Geometry and Boundary Conditions

The geometry was modeled as a rectangular prism, with a mesh refinement (SLM - 11 μm, EBF^3 - 0.22 mm) applied along the path of the heat source. Figure 3.12 shows the orthogonal mesh, mesh refinement, and location of the heat source. For the SLM samples, the full domain was 6 x 6 x 3 mm. For the EBF^3 simulation, the full domain was 60 x 60 x 30 mm. A symmetry plane was applied at z=0, so that only half the melt pool needs to be simulated.

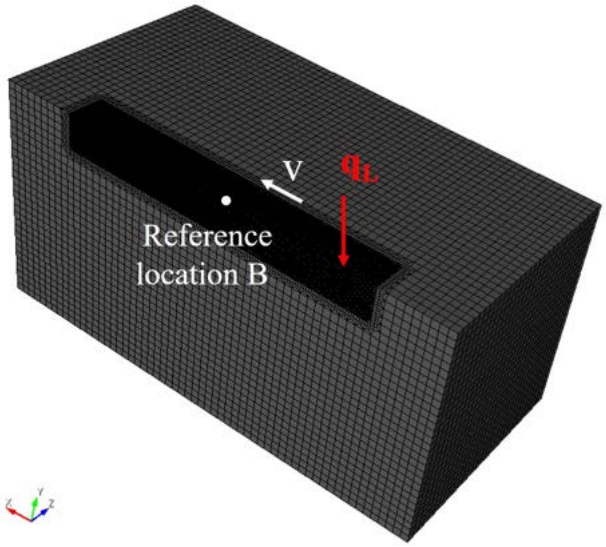

Figure 3.12: FEA single track solidification model geometry depicting mesh, mesh refinement, location of temperature reading (location B), heat input at the start of the simulation (q_L) and travel velocity direction (v)

The bottom boundary of the substrate was modeled as constant ambient temperature ($T = 298K$). The sides of the block are adiabatic, with $q = 0$ W/mm^2. The top surface was modeled as a moving heat flux, q_L.

Equation 3.11 describes the laser heat source, q_L, for the SLM simulations. The moving heat source is assumed to be a Gaussian heat distribution [73]. For the SLM125 used for the experimental work, the laser spot size is 70 μm, so the radius $\sigma = 0.35$μm. The power (P) in Watts changes between the three simulations, A describes the absorptivity (0.32, Table 3.7), and r is the radial distance from the center of the beam to location x.

$$q_L = \frac{PA}{2\pi\sigma^2} e^{\frac{1}{2}\left(\frac{r}{\sigma}\right)^2} \tag{3.11}$$

The EBF^3 case was iteratively simulated to match the experimental results of the deposit. The iterations are performed since the EBF^3 heat source cannot be directly modeled as single track pass. Due to the influence of the wire feed rate, the actual thermal model heat source is significantly more complex. For a first approximation, the single track pass was modeled with a conical heat source (Figure 3.13) to provide an estimate for cooling rates and thermal profiles.

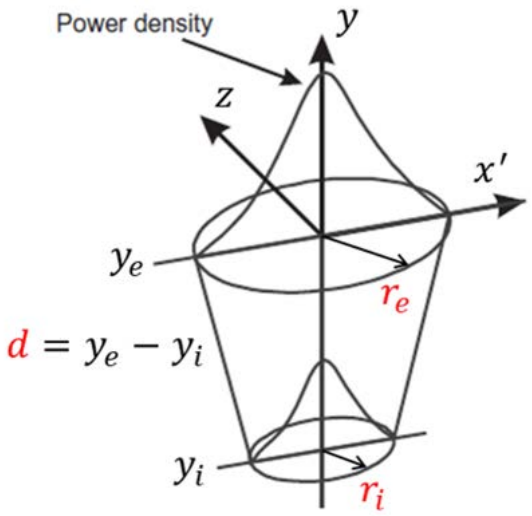

Figure 3.13: Graphical description of the conical heat distribution used as the heat flux source for the EBF^3 thermal model

The conical heat source is described by Equation 3.12a, where A is absorptivity, P is beam power (W), and $r_e = 1.1$mm, $r_i = r_e/4$, and $d = 1.1$mm are graphically shown in Figure 3.13 and were iteratively tuned to best match the resulting experimental substrate melt pool of Sample 8-1.

$$q_L = \frac{9AP}{2\pi} \frac{e^{-3r^2/r_0^2}}{d(r_e^2 + r_e r_i + r_i^2)} \tag{3.12a}$$

$$r_0 = r_e - \frac{(r_e - r_i)(y_e - y)}{d} \tag{3.12b}$$

$$d = y_e - y_i \tag{3.12c}$$

Initial Conditions

The power-scan speed combinations for the 3 SLM cases are presented in Table 3.8. These cases were selected after characterizing the experimental cubes to describe a well-formed parameter set, as well as the lower and upper bounds of the parameters printed. For ease of readability, the cases selected are named with respect to energy density (low, medium, and high). The entire domain is initialized at $298K$.

Table 3.8: Laser power and scan speeds used for the three SLM thermal solidification models

	Laser Power (W)	**Scan Speed (m/s)**
SLM Med	110	0.4
SLM High	80	0.1
SLM Low	80	1.6

For the EBF^3 simulation, the accelerating voltage is 30 kV and the beam current is 85 mA (2550 W). The translation speed (v) is 0.0085 m/s (20 ipm).

Chapter 4
Results

4.1 Base Material Characterization

Metallurgical characterization was performed to confirm vendor specifications on the base wire and base powder. In addition, the VSM was used to collect magnetic data to provide a basis for comparison to depositions and historical literature.

4.1.1 Wire Analysis

Wire analysis consisted of OM imaging of etched samples, SEM imaging, and EDS. Figure 4.1 shows the bright field optical images for etched radial and transverse sections of the starting wire. The diameters of the wire sections ranged from ⌀ 1.629 to 1.635 mm, which was within an acceptable range of the nominal 1.6 mm typically used for the EBF^3 process.

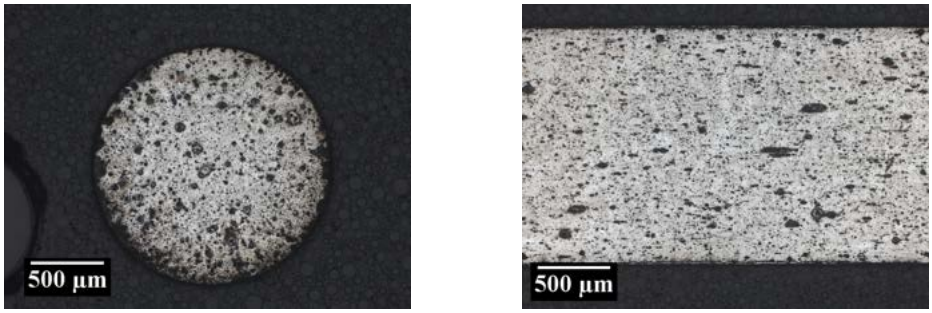

(a) Radial optical wire micrograph **(b)** Transverse optical wire micrograph

Figure 4.1: Optical micrographs taken of the transverse and radial directions of the base wire

The etched surfaces showed a number of black regions, which were inspected further with secondary and backscatter SEM images. Figure 4.2 presents

an etched black region under SE and composite topographic conditions. From the SEM images, a single etched black region was multiple grains approximately 100 μm in width and is not a precipitate, which would be manifested by elemental contrast in the SE-BSE topographic image. The grains seen in Figure 4.2 were preferentially exposed through the etching process and subsequent removal of cube-on-edge grains.

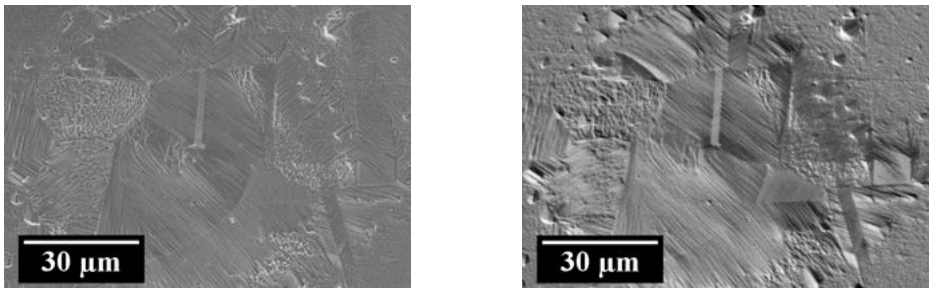

(a) SE **(b)** SE-BSE topographic image

Figure 4.2: SEM micrographs of the base wire, showing the black features with areas of relief seen in Figure 4.1. It was determined that a single black region appears to be comprised of multiple grains approximately 100 μm in width and is not a precipitate.

To confirm the vendor specifications and determine alloy distribution, EDS mapping was performed on an unetched portion of the wire. Figure 4.3 presents a representative spectra, which confirmed a wire composition of 50wt% Ni and 49.7wt% Fe.

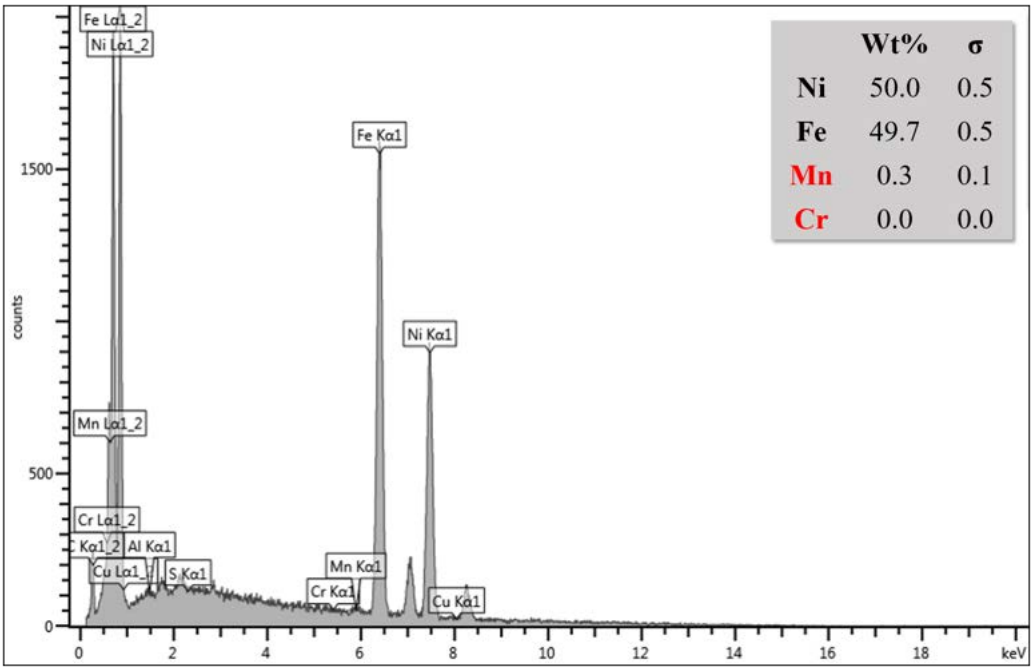

Figure 4.3: Representative EDS spectra of the base wire from Alloy Wire International

4.1.2 Powder Analysis

The Sandvik Osprey powder was analyzed using SEM and EDS. Figure 4.4 shows an SEM image of a mounted and polished cross-section of the powder. ImageJ^{TM} was used to confirm that the powder range was between 15 to 45 µm. For the 49 particles (threshold: diameter>5 µm) counted in Figure 4.5, the average diameter was on the low side of the vendor range, at 20 µm with a standard deviation ±9.2µm. While most powder spheres are within that range, a number of fine particles less than 5 µm were observed.

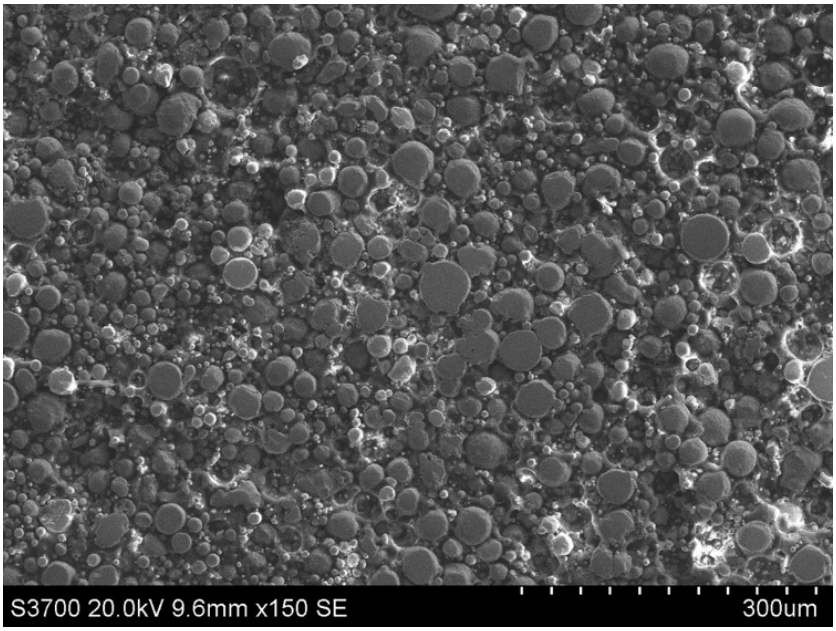

Figure 4.4: Base powder at 150x magnification. The powder consists of globular particles, on the order of 20±9.2µm in diameter. Satellite particles 3 µm and smaller are seen interspersed throughout the larger globular particles. The powder was mounted and polished to obtain a flat cross-section.

EDS was performed at seven locations to confirm the composition. Across the seven locations indicated in Figure 4.5, the average composition was 51.1wt% and 48.9wt% Ni. A representative EDS spectrum is provided in Figure 4.6. Minimal variance was seen across the seven locations, falling within a percent of the reported average.

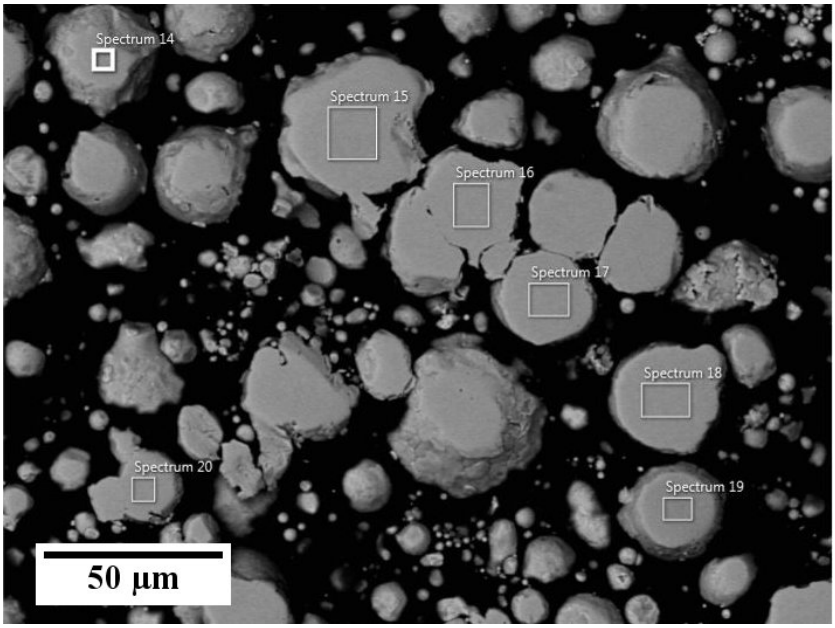

Figure 4.5: Backscatter SEM image of base powder. EDS spectra were taken at the seven locations indicated in the micrograph.

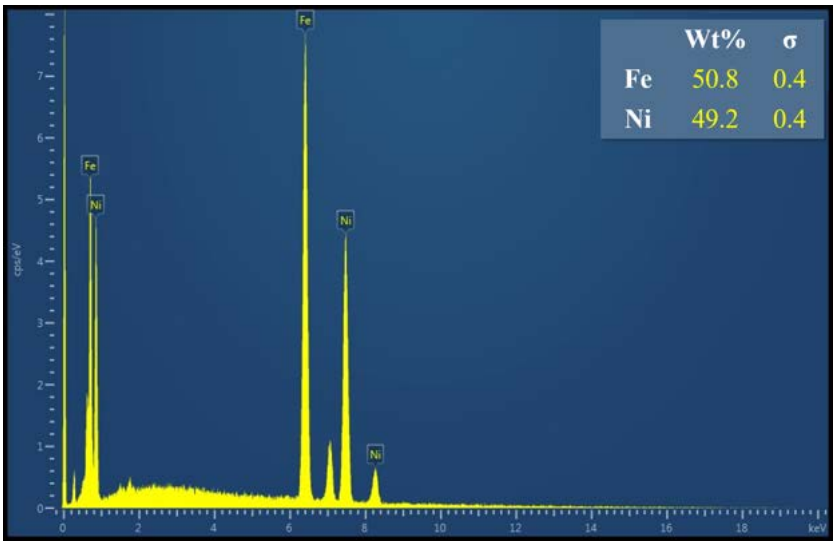

Figure 4.6: EDS spectra for the base powder obtained from Sandvik Osprey

4.1.3 Magnetic Properties

Hysteresis loops were collected for the base wire and powder samples as shown in Figure 4.7. The powder (blue) loop had a more gradual curve to reach the saturation magnetization asymptote. The difference in curvature was due to the microstructural differences between the two base materials.

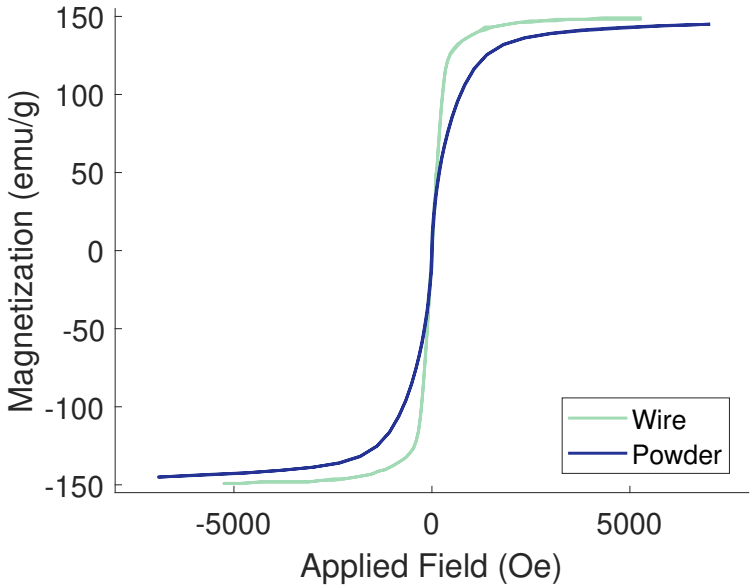

Figure 4.7: Hysteresis loops of base wire and powder materials. The hysteresis loops demonstrate the impact of microstructure and porosity on hysteresis shape and properties, as the wire (green) has a squared curve compared to the gradual transition of the powder (blue)

Table 4.1 compiles the magnetic properties measured for the wire and powder. Coercivity, the measure of remaining magnetization at the x-intercepts, was slightly higher for the powder. The powder's permeability, approximated as the slope B/H through the x-axis intercepts, was lower. The higher coercivity and low permeability was likely due to the homogeneity of the powder, compared to the wire, which was elongated due to the drawing process. Also of note, the saturation magnetization of the powder was lower than that of the wire. The slight elemental variance of the trace elements within each alloyed base material was likely to result in different saturation magnetization

values. Both the base wire and powder had a lower saturation magnetization than the literature value for pure Fe50Ni (154 emu/g) [38].

Table 4.1: Magnetic properties of base wire and powder

	Wire	**Powder**
Permeability (μ)	44±4.3	38±9.2
Coercivity (Oe)	2.5±0.89	3.5±2.5
Saturation Magnetization (emu/g)	148.6±2.9	141.9±2.9
Energy Loss (J/g)	4.19E-4±1.3E-5	4.61E-4±1.4E-5

4.2 EBF^3 Results

Of the 80 EBF^3 samples produced with the base wire described in Section 4.1.1, 51 were characterized for both metallurgical and magnetic properties with the methodology outlined in Section 3. Microstructure characterization is presented first, followed by the magnetic results.

4.2.1 Metallurgical Characterization

Optical Micrographs

Optical micrographs were used to determine deposit features, layer boundaries, and grain structure of the samples produced by EBF^3. Figure 4.8 shows the cross-sections of sample 8-1 perpendicular to the beam travel direction. Sample 8-1 was deposited using the "base" parameter set (AV 30, BC 85, WF 40, TS 20, BF 318) Bright field mode was used to emphasize the layer boundaries, melt pool morphology, the heat affected zone (HAZ), and the meta-stable structures of the final layer. Dark field mode was used to evaluate grain size and shape.

(a) Bright field optical micrograph

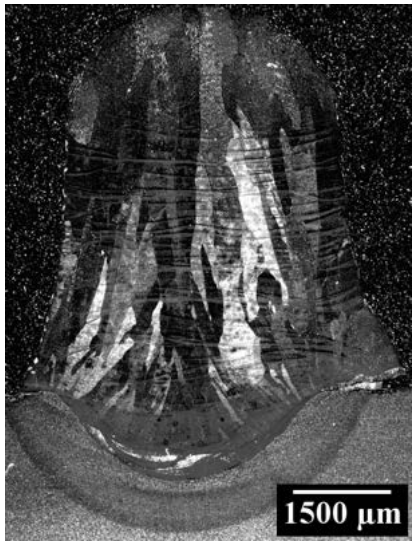

(b) Transverse optical wire micrograph

Figure 4.8: Optical micrographs (bright and dark field) taken of EBF^3 sample 8-1: Figure 4.8a shows individual layers, while 4.8b highlights the tall columnar grains extending through the length of the deposit.

General observations from the dark field image in Figure 4.8b showed the columnar grains. Grains were oriented towards the center top of the deposit, correlated with the easy solidification direction and highest thermal gradients. The bright field micrograph (Figure 4.8a) showed distinct layers and grains extending through layers. The top layer in the bright field image indicated a different grain morphology than the middle layers. The differences between the dendritic structure of the top layer and the columnar middle layers are highlighted in Figure 4.9. The optical micrographs from Figure 4.9 were obtained from sample 9-2, which was deposited at a higher beam current than 8-1 (AV 30, BC 100, WF 40, TS 20, BF 318).

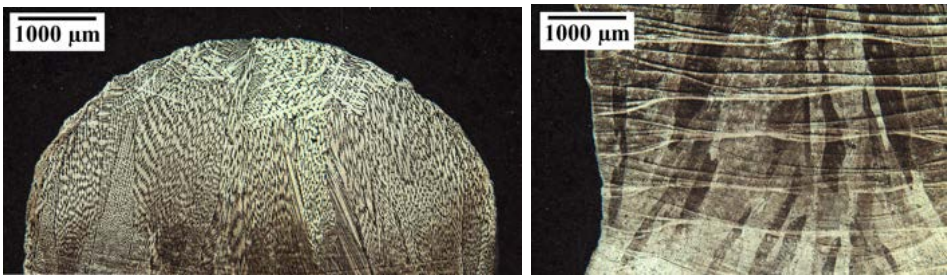

Figure 4.9: Optical micrographs (bright field) taken of EBF^3 sample 9-2. Top layer of the deposit (left) showed dendritic structures, while the middle of the deposit (right) showed columnar grains. Scale bars in the top left are 1 mm length.

The differing microstructures observed in Figure 4.9 are characteristic of all the EBF^3 deposits. The top layer morphology was similar to that of a weld, with a more equiaxed dendritic structure at the top center and cellular structures within the bulk of the deposit. The dendritic structure was formed because the center top had the highest solidification rate and lowest thermal gradient within the melt pool [11]. The columnar grains in the middle indicate remelting occurred. As a new layer is deposited, the previous top layers are remelted, losing the dendritic structure and reforming as columnar grains. Due to the different microstructure, the top layer may not have the same properties as the bulk of the deposit.

Transverse cross-sections were also evaluated for proper grain size determination of non-equiaxed structures [58]. The corresponding dark field transverse sample is shown in Figure 4.10. Figure 4.10 showed the slight angular rotation of the columnar grains, which point towards the print direction and direction of highest thermal gradient.

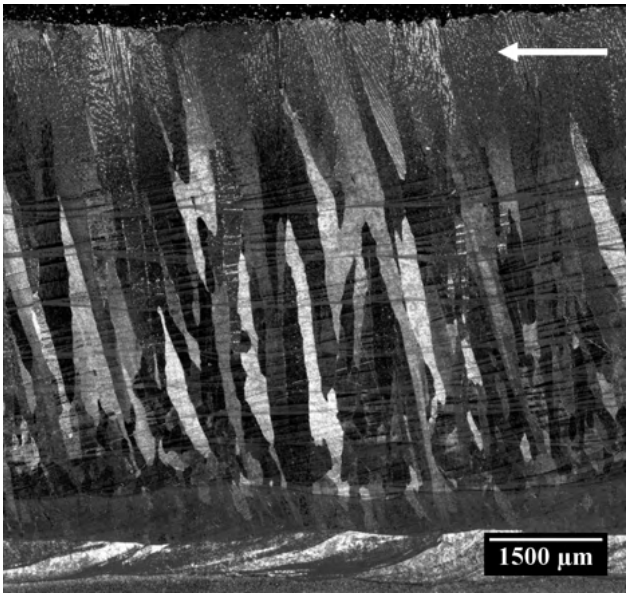

Figure 4.10: Optical dark field micrograph of transverse EBF^3 sample 8-1, with an arrow indicating the print direction

The grain sizes are given in Table 4.2. Grain size analysis was performed per ASTM E112 which requires 3 measurements in orthogonal directions [58]. Table 4.2 is organized in the following order: the translation column reports the average grain length in µm parallel to the print direction. The height reports the average grain length through the layers and with reports the same grain length through the width. The following three columns report the aspect ratios between the 3 directions. Most grains showed an aspect ratio of 4 to 1, with the long needle-like grains extending through layers. Finally, the average grain sizes are reported, which when normalized to an average diameter, ranged from 234 to 288 µm.

Table 4.2: Grain size distribution of selected EBF^3 deposits

Sample	Parameter	Average Grain Diameter (µm)				Aspect Ratio		
		Width	Height	Translation	Average	T:H	W:H	W:T
8-1	Base	200	670	167	284	4.01	3.35	1.19
8-6	TS 0.0064 m/s (15 ipm)	192	714	174	288	4.10	3.72	1.10
8-7	TS 0.013 m/s (30 ipm)	179	769	130	262	5.92	4.29	1.38
9-1	BC 75 mA	152	833	152	269	5.48	5.48	1.00
9-2	BC 100 mA	137	533	175	234	3.05	3.89	1.27

Composition Analysis

EDS was performed on a representative sample, 8-6, to determine vapor losses and elemental distribution through the deposit layers. The base wire had 50.0wt% Fe, 49.7wt% Ni, while the 8-6 deposit contained 51.3wt% Fe, 48.1wt% Ni. Elemental mapping from the base plate into the deposit is shown in Figure 4.11.

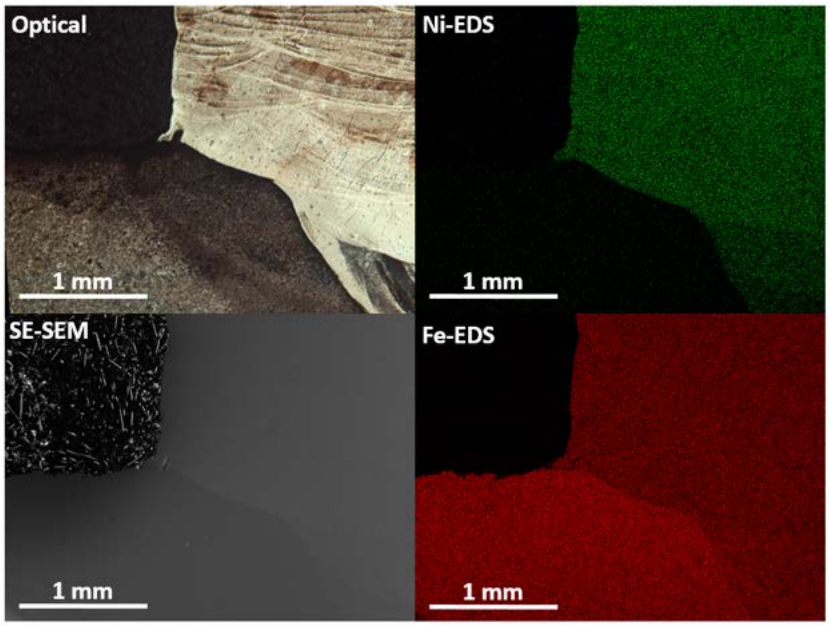

Figure 4.11: EDS mapping and SEM secondary imaging of EBF^3 sample 8-6. Sharp divisions of Fe and Ni composition are seen between the baseplate, below the deposit, and into the first layer.

The elemental mapping showed a sharp division between the base plate and the deposit. Furthermore, there was no observable solute segregation seen at the grain boundaries. The base plate and deposit segregation is reinforced in Figure 4.12, which used a series of EDS line scans to investigate the dilution of Fe through deposit layers.

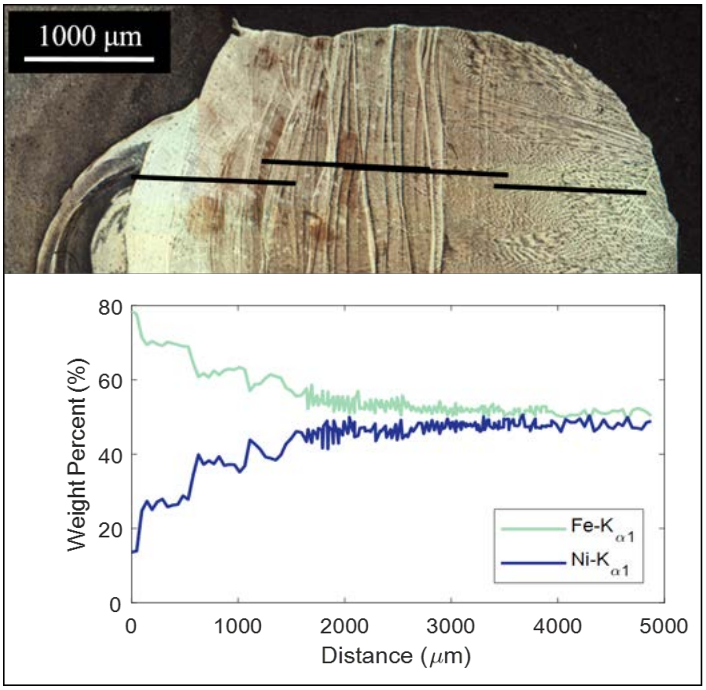

Figure 4.12: EDS line scan across the deposit layers of 8-6. Locations of the line scans are indicated by the black lines on the etched micrograph.

Figure 4.12 demonstrates that the baseplate material was diluted after layer 4, with elemental Fe and Ni reaching homogeneity. Four discrete Fe-rich steps were observed from the base plate through the first 3 layers closest to the base plate. Samples for the magnetic measurements in Section 4.2.2 were extracted above layer 4, to ensure elemental homogeneity.

Phase and Texture Measurement

XRD and EBSD were used in tandem to determine and verify phase. XRD was first used to determine the phase for samples 8-1, 8-6, and 8-7. EBSD was performed on samples 8-1, 8-3, and 10-3. The measured samples were selected based on variance in permeability, discussed in Section 4.2.2. The variance within magnetic properties indicated there may be microstructural differences. The processing parameters and magnetic properties of the five samples selected for EBSD or XRD are reported in Table 4.3.

Table 4.3: Magnetic properties of EBF^3 sample subset

Sample	AV (kV)	BC (mA)	WF (ipm)	TS (ipm)	BF	Coercivity (Oe)	Permeability	Sat. Mag. (emu/g)	Hyst. Loss (J/g)
8-1	30	85	40	20	318	3.33±2.68	130.9±14.5	146±2.92	1.63E-3 ±4.89E-5
8-3	30	85	30	20	318	0.335±0.13	16.12±1.52	146.2±2.92	1.76E-4±5.29E-06
8-6	30	85	40	15	318	9.43±28.18	240±240	145.7±2.91	2.33E-3±6.98E-5
8-7	30	85	40	30	318	2.93±2.044	102.1±11.17	146±2.93	1.89E-3±5.67E-5
10-3	30	85	40	20	323	1.521±0.8568	67.6±4.5	150±3	8.11E-05±2.43E-6

The diffraction patterns observed from XRD are given in Figure 4.13. The intensity peaks along the x-axis corresponded to FCC Fe50Ni [74]. The XRD results showed good agreement in peak location and it was concluded that all 3 samples are FCC. However, the peak intensities did not match the computed values for relative peak intensity of Fe50Ni. The discrepancy in peak intensities was due to the texture and grain size of the EBF^3 deposits. Since a polycrystalline sample has more grains of a particular orientation than a randomly distributed powder sample, the peak intensities will be skewed. Since Fe and Ni have similar x-ray scattering coefficients, the ordering of the phase is not able to be determined through XRD [75]. However, the magnetization results in Section 4.2.2 indicate that this was standard disordered Fe50Ni.

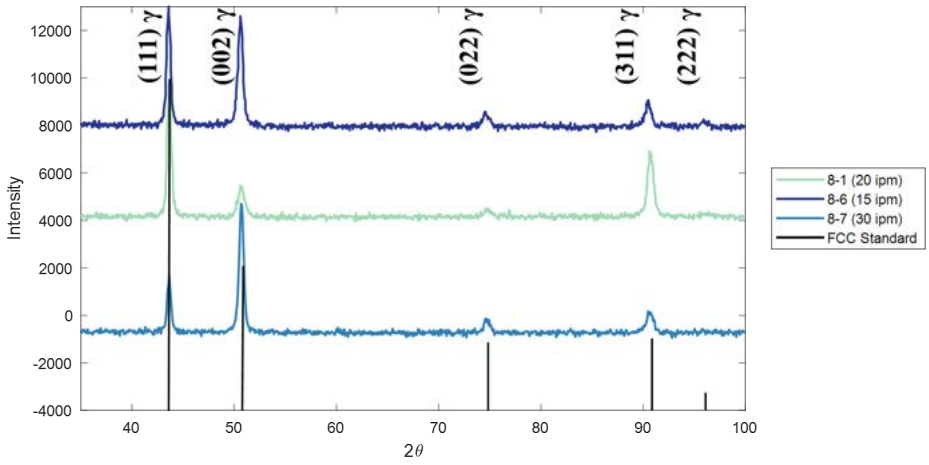

Figure 4.13: XRD diffraction patterns of three EBF^3 deposits

Three deposits were analyzed using EBSD. EBSD confirmed the FCC phases observed in Figure 4.13 and provided quantitative texture and grain size

information. Figure 4.14 shows the grain morphology and orientation of samples 8-1, 8-3, and 10-3.

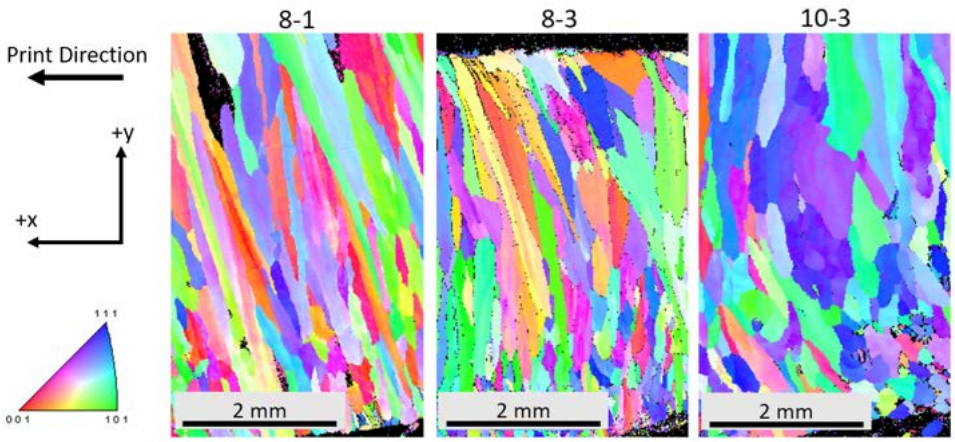

Figure 4.14: EBSD inverse pole plot (+z) mapping of EBF^3 deposits.

A pole plot of sample 8-1 (Figure 4.15) shows the texture. From Figure 4.15, the density clusters showed that the grains were arranged with a strong Goss texture [45]. The Goss texture, (110)[001], is commonly observed in rolled materials, as well as additive structures [45, 15].

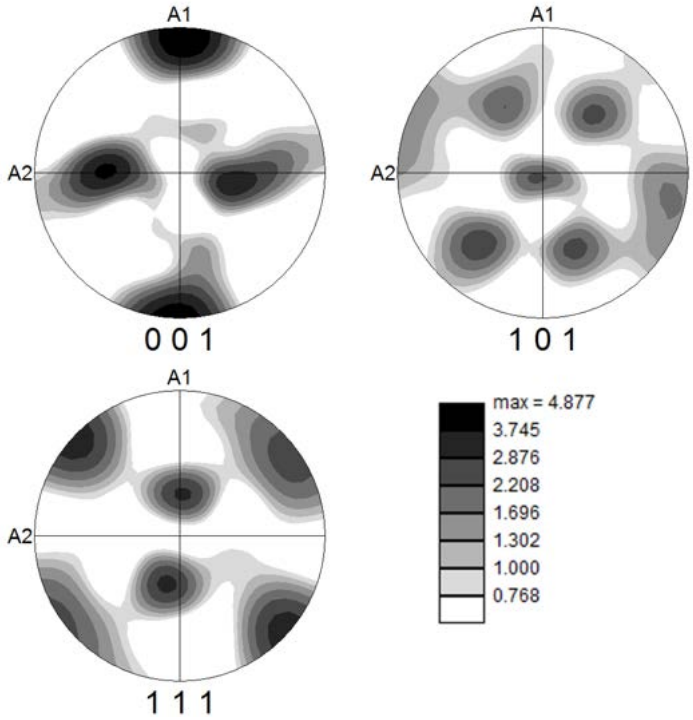

Figure 4.15: Pole plot of EBF^3 deposit 8-1

From the IPF maps in Figure 4.14, grain size (number and area) and texture were computed and are aggregated in Table 4.4. From Table 4.4, Sample 10-3 was noted to have the largest grains (1064 μm) and the highest MUD value 6.491.

Table 4.4: Grain diameter, and texture strength collected from EBSD on EBF^3 samples

	8-1	**8-3**	**10-3**
Average Number (μm)	170.5	141.1	404.4
Average Area (μm)	714.2	565.7	1064
MUD Value	4.877	4.328	6.491

4.2.2 Magnetic Results

The data obtained from the hysteresis loops for all EBF^3 samples thorough the deposit bulk were best visualized through statistical analysis. Figure 4.16 presents the distributions of input parameters as well as the results of magnetic measurements. For an individual sample's magnetic results, refer to Appendix C, or Table 4.3 for a subset. Due to the systematic, incremental design of experiments, the input parameters (AV, BC, WF, TS, BF, and E_L) were not normally distributed and have clear preferred values.

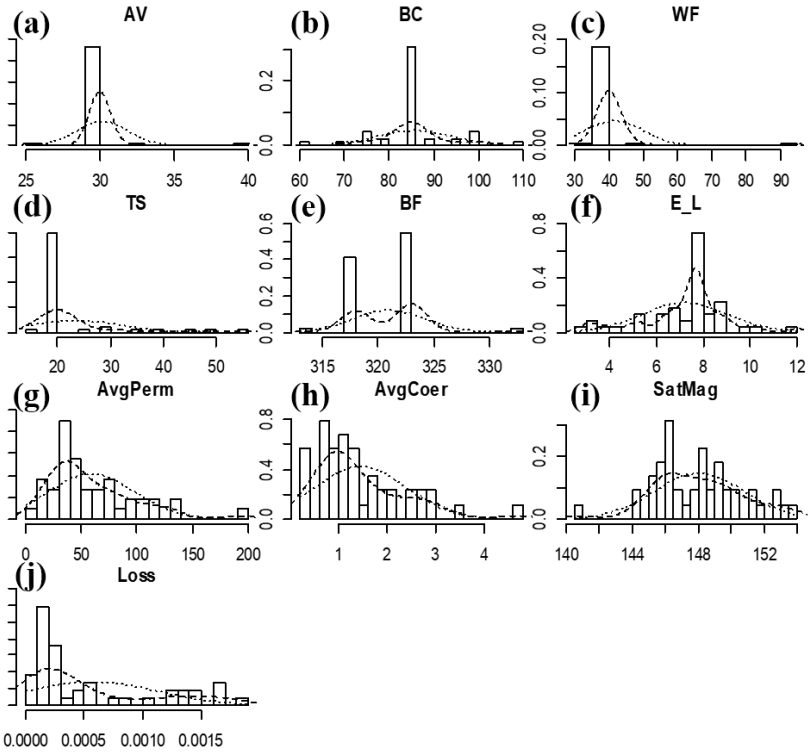

Figure 4.16: Histogram distributions of EBF^3 processing parameters and magnetic properties. Input parameters are represented by (a) to (f), were accelerating voltage is given in kV (a), beam current is given in mA (b), wire feed rate in ipm (c), translation speed in ipm (d), beam focus (e), and linear energy input as a function of AC, BC, and TS (f). The measured magnetic results are given in (g) to (j), with permeability (g), average coercivity in Oe (h), saturation magnetization in emu/g (i) and hysteresis loss in J/g (j).

Based on the histograms in Figure 4.16, the measured saturation magnetization values (i) had an approximately normal distribution. Permeability (g), coercivity (h), and hysteresis loss (j) were observed to be left-skewed. Since a lower bound of zero was present with all three of these measurements, the left skew was not unexpected. The means and standard deviations of the EBF^3 magnetic measurements are reported in Table 4.5.

Table 4.5: Statistics of EBF^3 magnetic properties

	Mean	**Standard Deviation**
Permeability (μ)	58.88	38.57
Coercivity (Oe)	1.439	0.9459
Saturation Magnetization (emu/g)	148.0	2.713
Hysteresis Loss (J/g)	5.576E-4	5.631E-4

Expanding on the population distributions, Pearson correlation coefficients were determined between processing parameters and magnetic results. A colorized heat map is presented in Figure 4.17 to show the correlations between these variables.

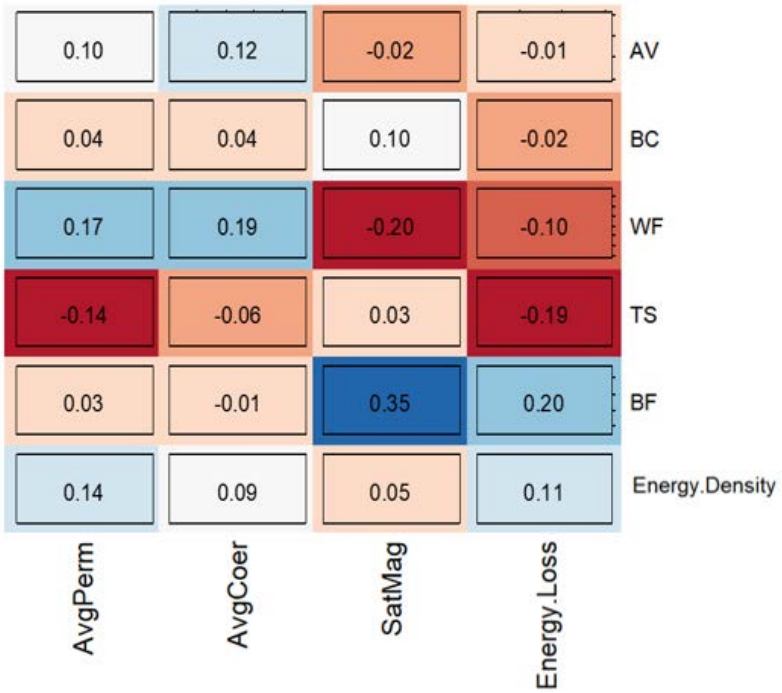

Figure 4.17: Pearson correlation coefficients between EBF^3 processing parameters and magnetic properties

Figure 4.17 demonstrates that there was very little correlation between the processing parameters and magnetic results for the EBF^3 samples. Pearson coefficients less than 0.3 are generally considered to be a low degree of correlation [66]. The only moderate degree of correlation observed in the EBF^3 samples was seen between the saturation magnetization values and beam focus.

In addition to bulk measurements, the magnetic response of the dendritic top layer (discussed in Section 4.2.1) was compared to the magnetic response of the bulk of the sample. The resulting hysteresis loops are presented in Figure 4.18.

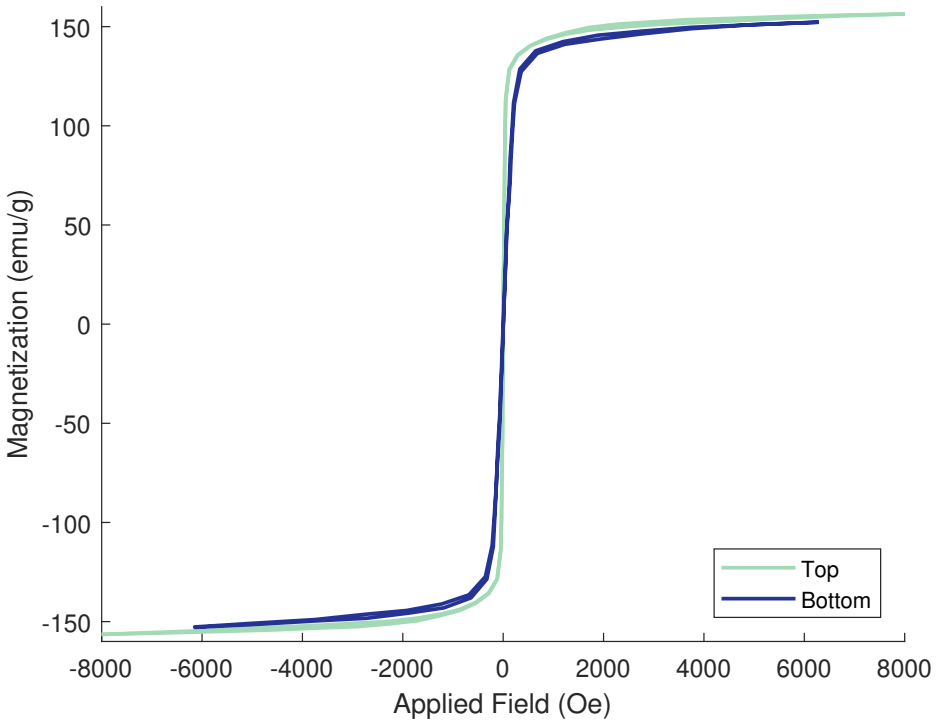

Figure 4.18: Hysteresis loops of 8-2 bulk and top layer. After the shape correction was applied, the bulk of the deposit has a smaller applied field. The smaller corrected applied field was expected due to the "squareness" of the bulk sample and subsequently larger shape demagnetization correction factor. The top sample had a bar magnet shape and a smaller demagnetization correction factor.

Different curvatures were observed for the top and bulk hysteresis loops as saturation magnetization was approached in Figure 4.18, indicating a difference in domain propagation. The magnetic properties are listed in Table 4.6. The magnetic properties vary between the top and bottom layers. The discrepancy in magnetic properties indicated that the dendritic structure impacts the magnetic measurements in a non-trivial way. However, given the nature of the EBF^3 process, the top layer is a transient role. While the top layer results are noted, the magnetic properties of the "steady-state" middle layer region of EBF^3 are of more interest.

The coercivity value was higher in the top layer, based on the smaller grains

and higher amount of grain boundaries. The permeability was also higher for the top layer, which was not expected. There are two possible explanations: the lower permeability may indicate domain wall movement is resisted in the bottom microstructure due to grain aspect ratio or texture, or it may be an artifact of the demagnetization correction factors.

Table 4.6: Magnetic properties comparison between top and bottom microstructures of EBF^3 deposits.

	Permeability (μ)	**Coercivity (Oe)**	**Saturation Magnetization (emu/g)**	**Energy Loss (J/g)**
Top	267.9	4.4711	154.6	1.50E-03
Bottom	66.955	1.74715	151	1.60E-03

4.3 SLM Results

Based on the relatively homogeneous and uncorrelated magnetic results of EBF^3, SLM samples were produced for comparison. The magnetic results of SLM are compiled in a similar manner to the EBF^3 results (Section 4.2.2).

4.3.1 Metallurgical Characterization

Optical Micrographs

Etched optical micrographs were taken of each selected SLM processing condition (Figure 4.19). With the aggregated array, Figure 4.19 gives a sense of which printing parameters yielded good microstructures and which had significant defects.

Microstructure varied greatly within the SLM samples. The process parameters spanned the printability map. Visual inspection and characterization showed that some samples had over-melt, while others had non-consolidated powder. Figure 4.20 shows camera and optical micrographs for an over-melted (Case 2), non-consolidated (Case 3), and good quality sample (Case 1).

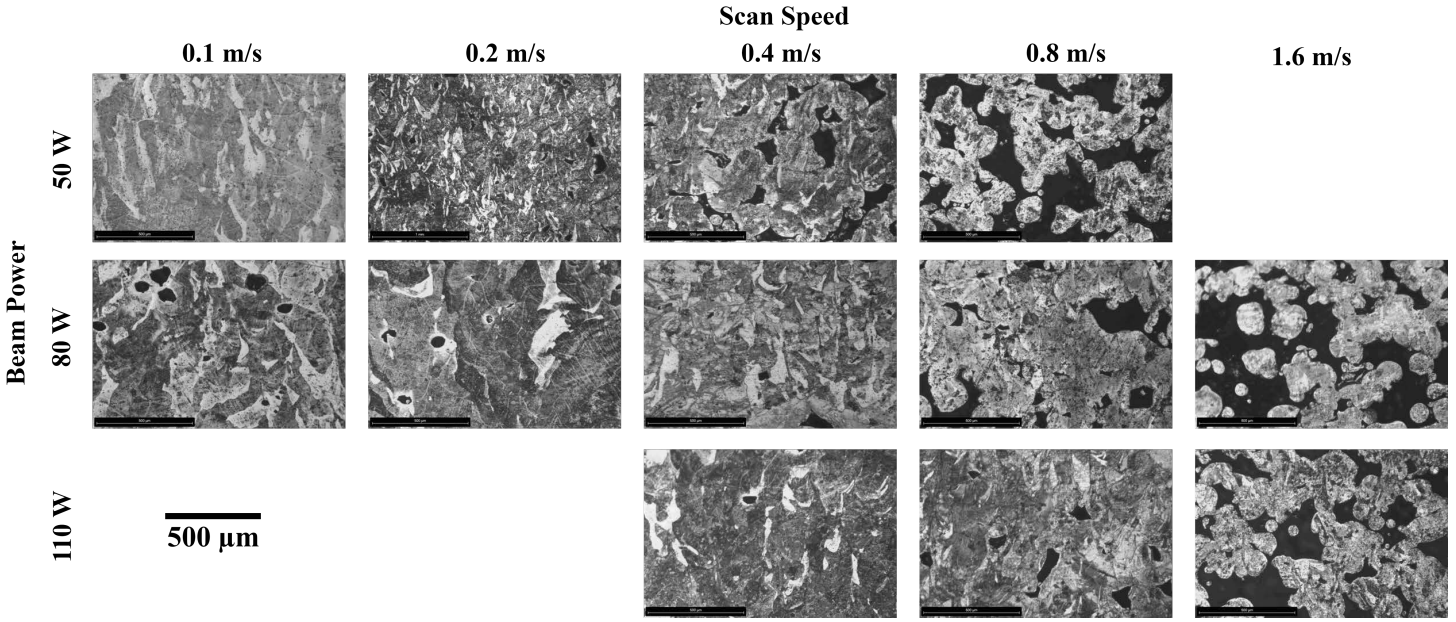

Figure 4.19: Optical micrographs (25x) of SLM deposits, displayed by scan speed and beam power. Parameter sets 1-1 to 12-1 are arranged from left to right, starting at the top left (0.1 m/s, 50 W). Micrographs are scaled appropriately for use with the scale bar in the bottom left. As scan speed increases, more lack-of-fusion porosity and unmelted powder is observed.

Inspection of Figure 4.20c shows a porous, spongy appearance. The associated micrograph shows a large amount of powder particles, which were not incorporated into the melt pool. The lack of melting and subsequent fusion is further supported by density measurements. The atomic density of disordered Fe50Ni is 8.25 g/cm^3 [38]. Deposited sample densities ranged from 5.26 to 8.17 g/cm^3, while the initial powder had a poured density of 4.20 g/cm^3 and a tapped density of 5.29 g/cm^3. The non-consolidated sample had a density of 5.26 g/cm^3. Essentially, the non-consolidated samples sintered enough to bind together, while maintaining the structure of the powder.

When examining the over-melted sample, the surface shows a sunken middle, with large smooth facets (Figure 4.20a). The optical micrograph shows porosity, though more likely due to gas entrapment over lack of fusion (see Figure 5.10 for more detail). The sample considered good quality (Case 1), Figure 4.20b, had a good optical surface finish and minimal porosity.

ImageJ^{TM} measurement analysis was performed on the micrographs provided in Figure 4.19 to measure porosity and evaluate melt pool dimensions. Porosity was evaluated through manipulating the micrograph coloring to a binary image, then measuring the percent area of each color. Melt pool dimensions were measured manually, between several visible melt pools.

Table 4.7: Melt pool morphology and porosity measurements from SLM samples. Some high porosity samples did not have measureable melt pools and are marked with '–'.

	Depth (μm)	**Width (μm)**	**Percent Porosity (Area)**
1-1	91.1	236	0.103
2-1	103	218	1.61
3-1	–	–	11.0
4-1	–	–	26.8
5-1	160	219	1.32
6-1	168	163	0.416
7-1	132	210	2.73
8-1	104	270	9.64
9-1	–	–	34.9
10-1	129	149	0.385
11-1	107	200	6.59
12-1	–	–	28.0

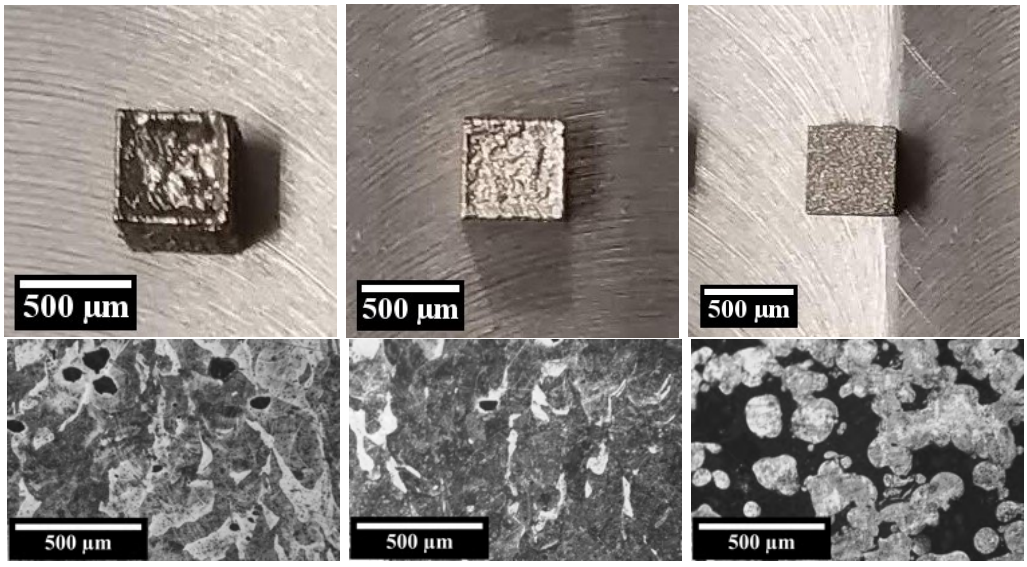

(a) SLM 2 (80W, 0.1 m/s) - Over-melted

(b) SLM 1 (110W, 0.4 m/s) - - Good Quality

(c) SLM 3 (80W, 1.6 m/s) - Non-consolidated

Figure 4.20: Camera and optical images showing the visual and microstructural differences though the SLM deposition parameters. When the energy input is too high, as observed in 4.20a, over-melt occurs. Over-melt vaporizes alloying elements, generating porosity from trapped gases. Non-consolidation and lack-of-fusion defects occur when energy input is too low (seen in 4.20c), and the powder does not form a melt pool that achieves depth of penetration.

Composition Analysis

EDS was performed on samples of varying power density. Elemental composition was checked semi-quantitatively for the *"over-melted"* sample case (5-1, 80 W, 0.1 m/s), a *"good quality"* sample (10-1, 110 W, 0.4 m/s), and a *"non-consolidated"* sample (4-1 50 W, 0.8 m/s). Area scans were performed to provide compositional data to the SE SEM micrographs in Figure 4.21.

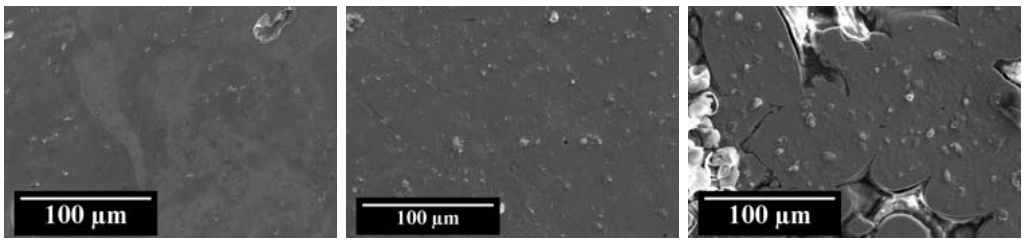

(a) 5-1 **(b)** 10-1 **(c)** 4-1

Figure 4.21: SE SEM micrograph of the areas used for EDS analysis of SLM deposits. Area scan EDS is performed in the bulk of each SLM sample. 4.21a is taken from SLM 5-1, an over-melted sample, 4.21b is taken from SLM 10-1, a good quality sample, and 4.21c, a non-consolidated sample.

The elemental compositions obtained by area EDS are given in Table 4.8. The initial powder had an elemental composition of 51.1wt% and 48.9wt% Ni. The final SLM deposits had a negligible difference in composition to the initial powder material.

Table 4.8: Elemental composition collected from EDS on SLM samples

	Fe (wt%)	**Ni (wt%)**
5-1	50.3	49.1
10-1	51.4	48.6
4-1	51.2	48.8

Texture and Grain Size Analysis

EBSD was performed on a sample from each of the 12 selected processing conditions. EBSD was used to determine phase, grain size, grain morphology, and texture of the samples. The (+z) map of each condition is presented as a chart in Figure 4.22. From Figure 4.22, grain size and texture strengthening is observed as scan speed decreases or beam power increases.

Based on the Kikuchi patterns, all 12 deposits were FCC. In addition to confirming FCC phase, the EBSD plots gave texture and grain morphology information. Compared to the EBF^3 deposits (Figure 4.14), SLM grains were

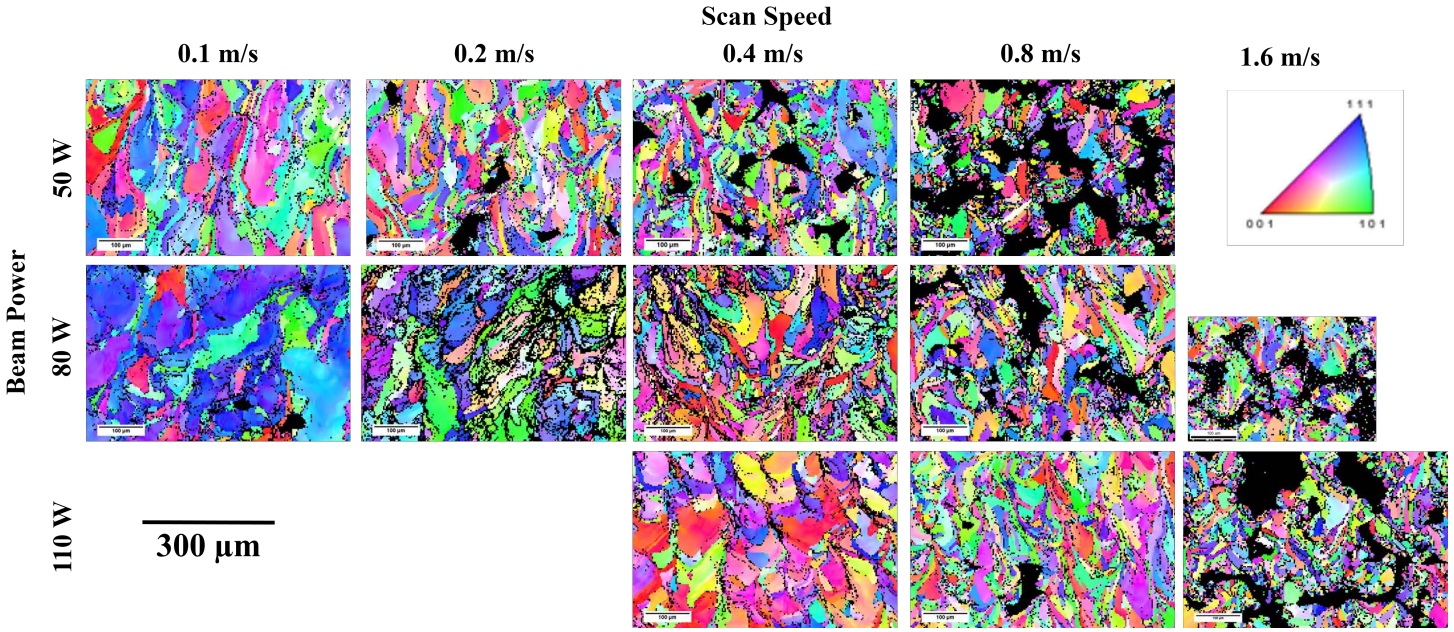

Figure 4.22: EBSD mapping of SLM deposits, displayed by scan speed and beam power. Parameter sets 1-1 to 12-1 are arranged from left to right, starting at the top left (0.1 m/s, 50 W). IPF coloring is in the (+z) direction, out of the page. As scan speed decreases or beam power increases, grain size is observed to increase and texture strengthen.

also columnar but with smaller aspect ratios. The texture, average grain size, and average misorientation angle are presented in Table 4.9.

Table 4.9: Grain size, misorientation, and texture strength collected from EBSD on SLM samples

	Average Number (μm)	**Average Area** (μm)	**Misorientation Angle** (degrees)	**MUD Value**
1-1	15.43	58.84	22.79	2.351
2-1	13.27	34.17	32.44	1.759
3-1	11.98	28.48	34.90	1.425
4-1	10.63	22.18	37.52	1.605
5-1	15.23	80.78	15.77	6.401
6-1	13.57	47.98	13.53	2.564
7-1	12.35	34.46	25.36	1.944
8-1	11.44	27.98	33.71	1.965
9-1	8.46	15.98	36.36	1.812
10-1	15.41	57.05	20.38	3.314
11-1	12.74	32.87	31.48	1.824
12-1	12.35	34.46	36.67	1.514

4.3.2 Magnetic Measurements

Figure 4.23 shows the variable histogram distributions for both the processing parameters as well as the magnetic responses. The SLM distributions shown in Figure 4.23 were similar to the EBF^3 histograms (Figure 4.16). Both permeability (d) and coercivity (e) had a left skew, likely due to the lower bound of zero for the measurements. In contrast to EBF^3, the saturation magnetization values (f) showed a uniform distribution rather than a normal distribution. Additionally, the SLM hysteresis energy loss (g) was less skewed than the EBF^3 distribution and is better categorized as a normal distribution.

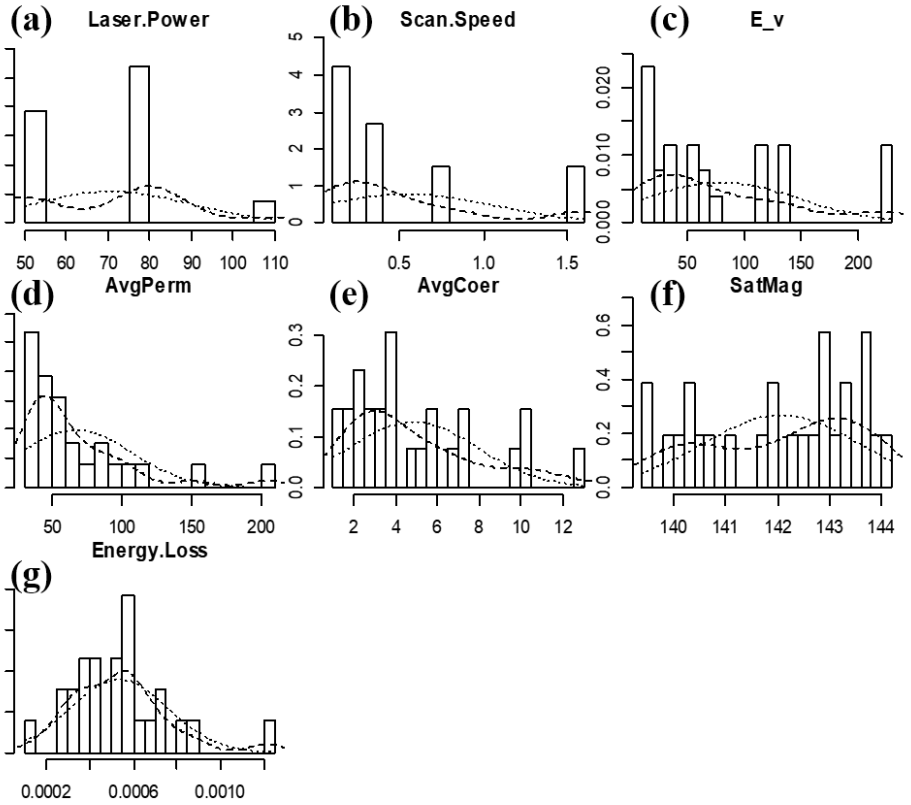

Figure 4.23: Histogram distributions of SLM processing parameters and magnetic properties. Input parameters are represented by (a) to (c), were laser beam power is given in W (a), scan speed is in m/s (b), and volumetric energy J/mm^3(c). The measured magnetic results are given in (d) to (g), with permeability (d), average coercivity in Oe (e), saturation magnetization in emu/g (f) and hysteresis loss in J/g (g)

The mean and standard deviation of the SLM magnetic properties are presented in Table 4.10.

Table 4.10: Statistics of SLM magnetic properties

	Mean	Standard Deviation
Permeability (μ)	66.67	40.36
Coercivity (Oe)	4.824	3.092
Saturation Magnetization (emu/g)	142.1	1.496
Hysteresis Loss (J/g)	5.331E-4	2.234E-4

Finally, the Pearson correlation coefficients were determined for the SLM inputs and outputs and are presented in Figure 4.24.

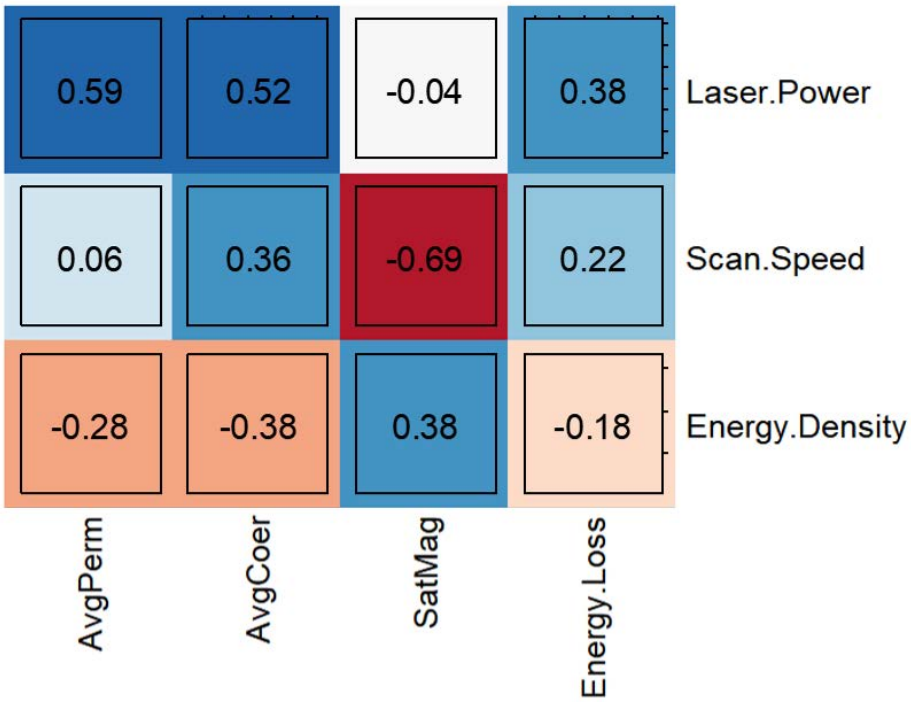

Figure 4.24: Pearson correlation coefficients between SLM processing parameters and magnetic properties

Many of the Pearson coefficients had a moderate to high degree of correlation. Specifically, any coefficients with an absolute value between 0.3 and 0.5 are considered a moderate degree of correlation, while anything greater than 0.5

is considered a high degree of correlation. For the SLM population, high degrees of correlation were seen between permeability and laser power, and coercivity and laser power. While energy density was also correlated strongly, the energy density was dependent on laser power and was not an independent variable. The other high degree of correlation observed was between scan speed and saturation magnetization. While correlation alone is not enough to determine cause, the highly correlated relationships allow process-property linkages to be explored.

4.4 Computational Results

A Sierra Mechanics^{TM} model was run to determine theoretical melt pool geometry, a temperature profile, and cooling rate for a single track model on a flat plate to provide verification and comparison to the experimental results of a subset of the SLM and EBF^3 depositions.

The computed thermal distribution for SLM Med (110 W, 0.4 m/s) is shown in Figure 4.25 and the results of the simulations are compiled in Table 4.11.

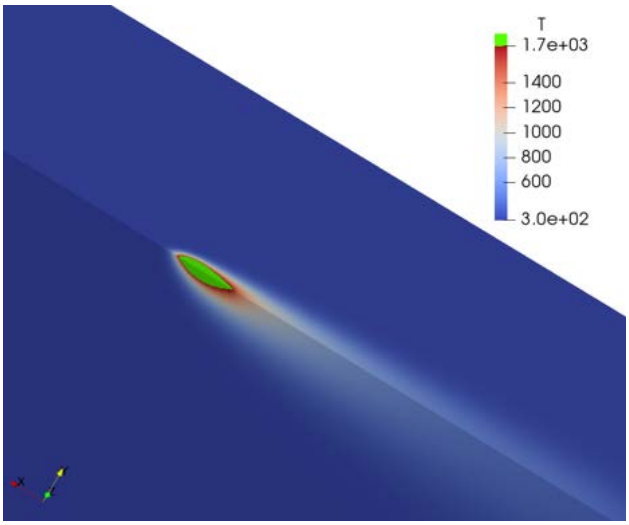

Figure 4.25: Temperature distribution of single track laser heating of flat plate. The liquid phase and melt pool morphology is shown in green, and determined at the melting temperature threshold (1693K).

Table 4.11: Predicted melt pool morphology and maximum cooling rates for 3 SLM cases and one EBF^3 case using a solidification model of a single track pass.

	Power (W)	**Scan Speed** (m/s)	**Depth** (μm)	**Width** (μm)	**Length** (μm)	**Cooling Rate** (K/s)
SLM Med	110	0.4	128.8	35.9	600.4	1.8e7
SLM High	80	0.1	160.4	56.2	199.1	3.5e6
SLM Low	80	1.6	59.8	5.8	107.6	6.0e7
EBF^3	2550	0.0085	4550	23900	10040	5.17e3

Chapter 5
Discussion

Research was carried out to evaluate the magnetic properties of Fe50Ni printed by electron beam freeform fabrication (EBF^3) and selective laser melting (SLM). As previously discussed in Chapter 4, the printed samples exhibited a wide variation in terms of microstructures and defect density. Printability considers the impact of processing parameters on porosity, cracking, deposit surface morphology, and microstructures. This chapter first explores aspects of printability which assesses changes in specific processing parameters on porosity, cracking, deposit surface morphology, and microstructures. Next, relationships between grain size, texture, and morphology are presented and compared with conventional solidification theory and literature from the welding community. Finally, the structure insensitive and sensitive magnetic properties are discussed.

5.1 Printability of FeNi

Printability, is defined as "the ability of a feedstock material to be successfully deposited as bulk material meeting the mechanical, metallurgical, and functional performance requirements of a specific application [8]." Printability relies on both appropriate alloy selection and processing parameters. It was anticipated Fe50Ni would have good alloy printability since Fe and Ni are considered to be metallurgically compatible and possess similar densities, laser adsorption levels, and no galvanic couple formation [51]. Moreover, Fe50Ni is used commercially as weld wire and in other rapid solidification processes such as melt-spin forming [37, 53]. Since additive manufacturing is a rapid solidification process which shares similarities to welding, Fe50Ni was expected to be compatible with additive manufacturing.

To evaluate processing parameter printability, macro-scale features such as surface finish, cracking, and porosity were assessed. Parameter printability is often approximated by the heat input of the system. Energy density,

which combines print speed, beam power, and layer thickness, is often used to estimate the volumetric heat input. Equation 2.2, reprinted below, determines the energy density (E_v) for SLM processing using beam power (P), scan speed (v), hatch spacing (h), and layer thickness (t) [8].

$$E_v = \frac{P}{vht} \tag{5.1}$$

High power, low scan speed, and small layer thickness lead to high energy densities. If the energy density is too high, over-melting occurs, leading to slumping and porosity from keyhole formation and gas entrapment [8]. When the energy density is too low, the deposition is under-melted. Under-melting leads to lack of fusion between layers and significant porosity. The energy density thresholds for good printability vary with material properties and are typically determined experimentally using engineering judgment.

5.1.1 EBF^3 Printability

The EBF^3 depositions exhibited excellent printability. All characterized EBF^3 samples showed good surface finish, no visible porosity, and no cracking. Metallurgically, the samples had large needle-like columnar grains with a strong Goss texture (MUD = 4.877). Area-averaged grain sizes ranged from 565.734 to 1064.73 μm. As presented in Section 3, EBF^3 samples were concentrated to a much smaller processing window than SLM. The small processing window is attributed to the manual nature of EBF^3. Each new layer is manually activated, so poor processing parameters are adjusted or abandoned in-situ.

Effects of poor processing parameters consisted of two categories, under-melted or over-melted. Both cases lead to inhomogeneities. Under-melted samples lead to "wire sticks" where the melt pool doesn't have enough heat input to smoothly melt the wire feedstock, and unmelted wire is present in the final deposit. Over-melted samples are characterized by slumping, where the previous layers begin to sink towards the baseplate. At less extreme over and under-melting, the material will "hump" or ball due to PlateauRayleigh instability, forming an inhomogenous deposit cross-section [8]. Figure 5.1

shows two representative EBF^3 deposits, with the visual characteristics of good and poor printability noted.

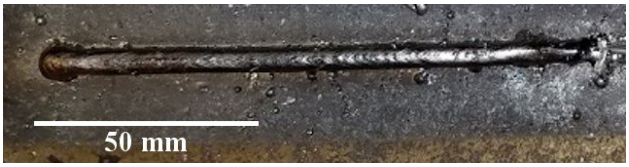

(a) Good Printability

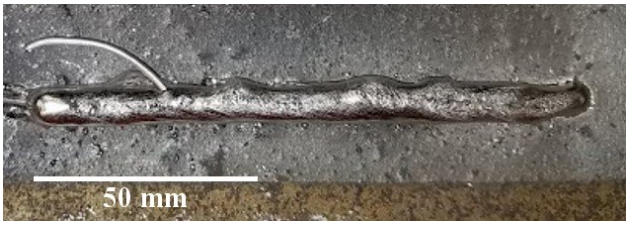

(b) Poor Printability

Figure 5.1: Images of EBF^3 deposits demonstrating good and poor printability. The sample in Figure 5.1a was deposited at 30 kV, 75 mA, 0.017 m/s (40 ipm) (WF), 0.0085 m/s (20 ipm) (TS) and has a smooth surface finish and constant cross-section. Figure 5.1b was deposited at 40 kV, 100 mA, 0.04 m/s (95 ipm) (WF), 0.0085 m/s (20 ipm) (TS) and shows a wire stick and *"humping"* through the cross-section.

Due to the narrow processing window and in-situ control, EBF^3 samples had less variance in microstructure, resulting in less overall variation in properties.

5.1.2 SLM Printability

For SLM, the microstructure, porosity, and printability varied greatly across the processing window where changes in laser power and laser speed spanned the printability map. Visual inspection and characterization in Section 4.3.1 showed that samples 5-1 and 6-1 were significantly over-melted (80 W, 0.1 to 0.2 m/s), while all samples printed at 0.8 m/s or faster were under-melted, as well as 2-1 and 3-1 (50 W, 0.2 to 0.4 m/s). As expected, the over-melted and non-consolidated samples exhibited large degrees of porosity and poor surface finish. The porosity variance is underscored in Figure 5.2.

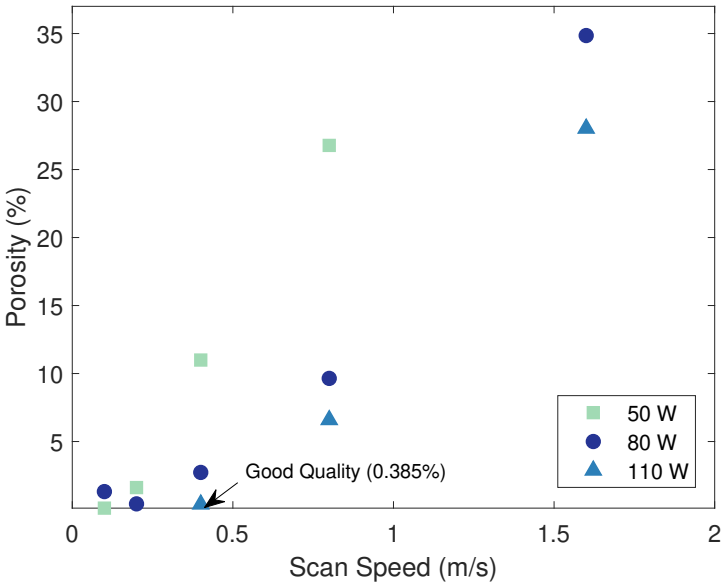

Figure 5.2: Area porosity of SLM deposits dependent on laser speed and power. The "good quality" sample, SLM Med, is labeled.

Lower scan speeds produced samples with low porosity samples as shown in Figure 5.2. The processing window for SLM samples was not symmetric about printability, and yielded more non-consolidated, under-melted porosity than keyhole porosity. The only sample with clear over-melted porosity occurred at 80 W, 0.1 m/s. Figure 5.2 shows the area porosity increase when the scan speed decreased from 0.2 to 0.1 m/s at 80 W, indicating over-melt porosity. The sample labeled "good quality" in Figure 5.2 was selected for further discussion, hereby referred to as SLM Med. Optical microscopy performed on SLM Med, Figure 4.20b, shows that the sample has a good optical surface finish and minimal porosity. Table 5.1 compares the processing parameters for SLM Med against literature sources.

The work performed by Mazeeva et. al, summarized in Section 2.3.2, investigated the magnetic response of Fe50Ni produced by SLM. Mazeeva et. al heat-treated printed samples and characterized using EBSD, XRD, and VSM [29]. The work is referenced again when discussing experimental magnetic properties in Section 5.3. A second body of work compared, performed by Yakout et. al (Section 2.3.2), focused on developing rotary motors using AM

and determined printability on the basis of density. The rotory motor work did not characterize the resulting microstructures [30] and is only used to compare processing parameters.

Table 5.1: Parameters determined from experimental SLM and literature sources

	Power (W)	**Velocity** (mm/s)	**Hatch Spacing** (μm)	**Layer Height** (μm)	**Volumetric Energy** J/mm^3
SLM Med	110	400	120	30	76.39
Kurchatov Institute [29]	195	800	100	40	60.93
McMaster University [30]	200	600	100	40	83.33

Table 5.1 indicates that the overally volumetric energy was consistent with literature, despite variations in laser power and scan velocity for the SLM Med sample. In addition, the average grain sizes of the SLM samples fall within the range reported by the Mazeeva et. al [29]. Experimentally, the area-averaged grain sizes were 15.98 to 80.78 μm, while the literature reported 10 to 100 μm.

While over-melted and non-consolidated samples are undesirable for industrial applications, the microstructural variations allow for clear distinctions between processing regimes. The wide range of microstructures present through SLM amplifies potential process-structure-property linkages while conducting fundamental research.

5.2 Impact of Solidification Rate

While EBF^3 and SLM are both shown to have good printability, the resulting grain size and shape varied between the two processes. The differing microstructures emphasize the different processing conditions produced by each AM method.

As discussed in Section 2.2, the length scale for EBF^3 was much larger than SLM. The average EBF^3 print width was 4500 μm, while the hatch spacing for SLM was 120 μm. The EBF^3 layer height was 762 μm (0.03 in), while SLM was 30 μm, summarily the EBF^3 melt pool was significantly larger than that of SLM. Moreover, the majority of EBF^3 deposits occurred at 0.0085 m/s (20 ipm), which is significantly slower than the 0.1 to 1.6 m/s of SLM.

As a result, EBF^3 resulted in a larger heated volume and subsequently much lower thermal gradients and cooling rates as compared to SLM.

The difference in melt pool sizes and layer thickness between EBF^3 and SLM result in dissimilar deposition, cooling, and solidification rates. To compare the two processes, the temperature gradients and solidification (growth) rates were determined. Solidification theory was used to show how grain size and structure correspond to the temperature gradients and growth rates. Figure 5.3, obtained from *Welding Metallurgy* by Sindo Kou, shows how temperature gradients, solidification rates, cooling rates, and grain morphologies are related [9].

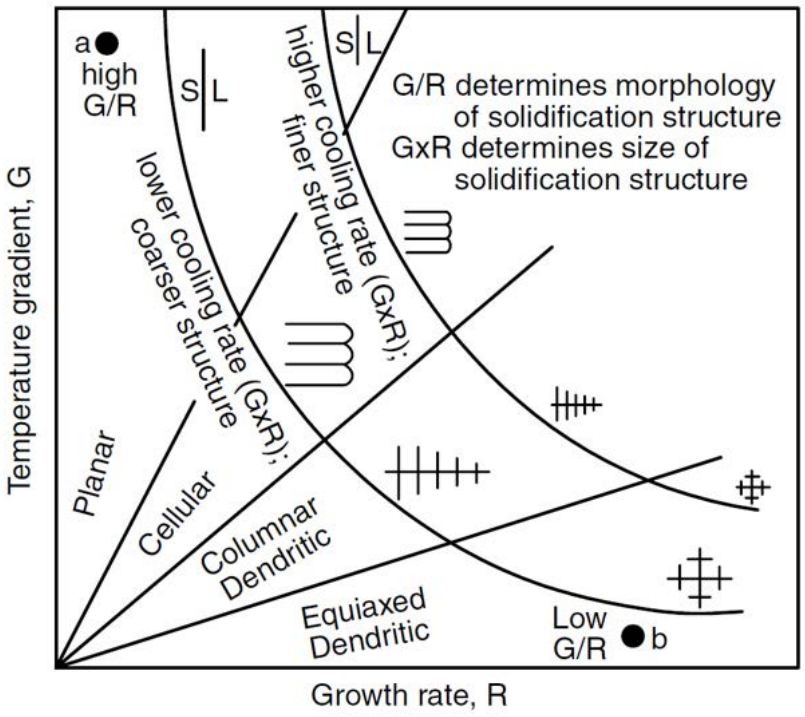

Figure 5.3: Solidification structure regimes showing the dependence of microstructures on temperature gradients (G) and solidification growth rate (R) and how grain morphology and size can be predicted[9]

In Figure 5.3, the temperature gradient (G) is considered the temperature difference from a desired location in the melt pool to the melt pool solid-liquid

boundary, divided by the distance between those points. Figure 5.4 gives a diagram showing the location of T_{max} and the centerline (CL). The temperature gradient between T_{max} and the centerline solid-liquid boundary was determined for each of the four representative cases through the computational modeling detailed in Section 4.4.

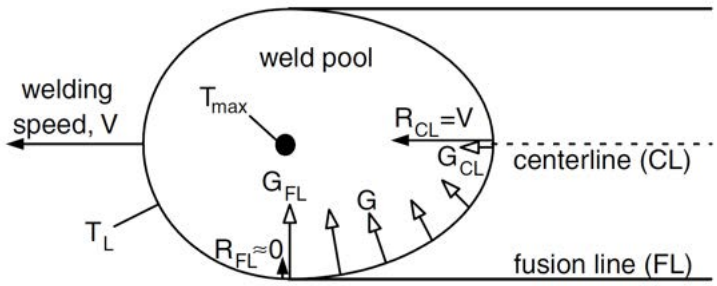

Figure 5.4: Temperature gradient (G) as a function of melt pool location. As the distance between the melt pool boundary and maximum temperature decreases, the temperature gradient increases [9].

The solidification/growth rate (R) for these processes must also be compared. Single pass models were approximated as single pass welding, and the solidification rate was estimated by Equation 5.2, where V is the welding velocity, and α is the angle between the welding direction and the normal vector of a location of interest at the pool boundary in 3D space [11].

$$R = V cos\alpha \tag{5.2}$$

For centerline solidification rates, $\alpha = 0$, so the solidification rate can be approximated as V . The solidification rate will never exceed V and can be considerably less at the bottom of the melt pool, where α approaches 90°. The maximum solidification rate, V , was used for quantitative analysis. The SLM printed at scan speeds 0.1 to 1.6 m/s; EBF^3 ranged from 0.00635 (15) to 0.0127 m/s (30 ipm).

From the computational results and Equation 5.2, the temperature gradients, maximum solidification rates, and maximum cooling rates were predicted and are compiled in Table 5.2.

Table 5.2: Predicted solidification rate, temperature gradients, and cooling rates. Predicted solidification rate is taken to be the free surface centerline solidification rate, which is the maximum solidification rate.

	Power (W)	**Solidification Rate** (R) (m/s)	**Thermal Gradient** (G) (K/μm)	**Cooling Rate** ($G \cdot R$) (K/s)	**Morphology** (G/R) (K-s/mm^2)
SLM Med	110	0.4	45	1.8e7	112
SLM High	80	0.1	35	3.5e6	350
SLM Low	80	1.6	37.5	6.0e7	23.4
EBF^3	2550	0.0085	0.61	5.2e3	71.5

As expected, Table 5.2 shows that EBF^3 had a significantly lower solidification and cooling rates than SLM. Within the three SLM cases, slower scan speeds and solidification rates corresponded with a lower predicted cooling rate. Independent of printing process, a slower scan/translation speed relates to a lower cooling rate, in agreement with solidification theory.

An additional parameter of interest is the morphology parameter (G/R). The morphology parameter provides indication of the solidification structure, dependent on the thermal gradient and solidification rate. From Table 5.2, the computed morphologies ranged from 23.4 to 350 K-s/mm^2. As noted in Figure 5.3, a higher morphology value corresponds with planar solidification and low morphology values corresponds with dendritic solidification. From Table 5.2, the two cases with good printablity, SLM Med and EBF^3, have similar morphology values despite the differing processing conditions.

For comparison to the predicted solidification values, the experimental EBSD microstructures associated with the four cases considered in Table 5.2 are given in Figure 5.5. From Figure 5.5 grain morphology, aspect ratios, and orientations were qualitatively observed. Significant porosity (black) is observed in SLM High and Low, supporting the over-melted and under-melted observations in Section 5.1.2. Moreover, the four cases have visually varied microstructures. EBF^3 samples exhibited needle-like columnar grains, which were several orders of magnitude larger in comparison to the SLM samples. Within SLM, SLM Low appeared to be minimally affected by the printing process, and largely unconsolidated. Spherical powder particles with small grains are observed. The grains of SLM Low have no visible orientation or texture relative to the printing coordinate system. SLM High exhibits the largest SLM grains (80.74 μm), with a significant number of grains oriented in the <111> direction. Table 5.3 compiles the quantitative data obtained from the EBSD plots.

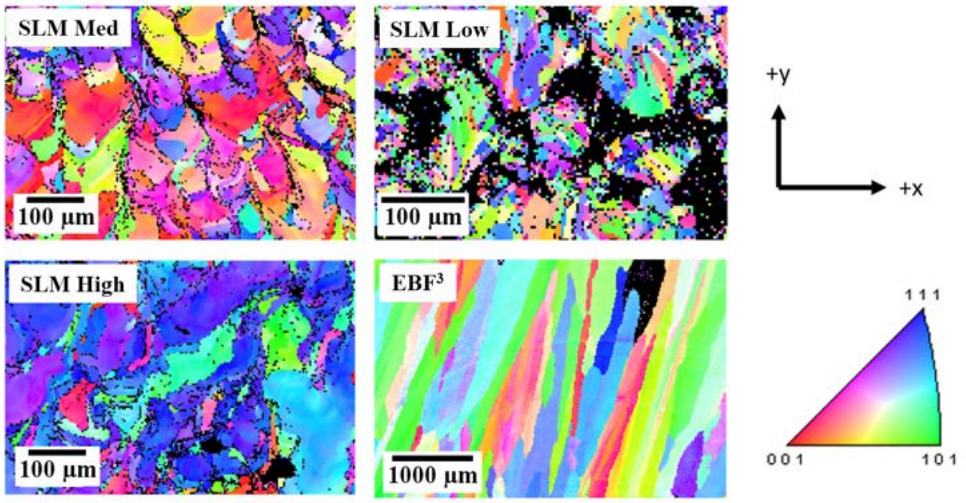

Figure 5.5: Inverse pole figures (+Z direction) of SLM and EBF^3 samples. The +y direction indicates the build direction (height) of the samples, while the +x direction indicates the roller direction for the SLM samples and the translation direction for EBF^3.

Table 5.3: Experimental EBSD grain size, texture, and grain structure of the four representative cases.

	Power (W)	**Velocity** (m/s)	**Average Grain Diameter** (Area Averaged) µm	**MUD**	**Structure**
SLM Med	110	0.4	57.06	3.314	Epitaxial Columnar
SLM High	80	0.1	80.78	6.401	Cellular
SLM Low	80	1.6	15.98	1.812	Equiaxed Dendritic
EBF^3 Case	2550	0.0085	714.19	4.877	Epitaxial Columnar

The overall solidification impact is summarized in Figure 5.6, which shows the approximate locations and experimental microstructures of the four cases on the theoretical solidification diagram [9]. Locations are placed using the data of Table 5.2. The two printing methods and varied processing parameters generated significantly different microstructures, with measured differences in solidification structure, grain morphology, texture, size, and defects.

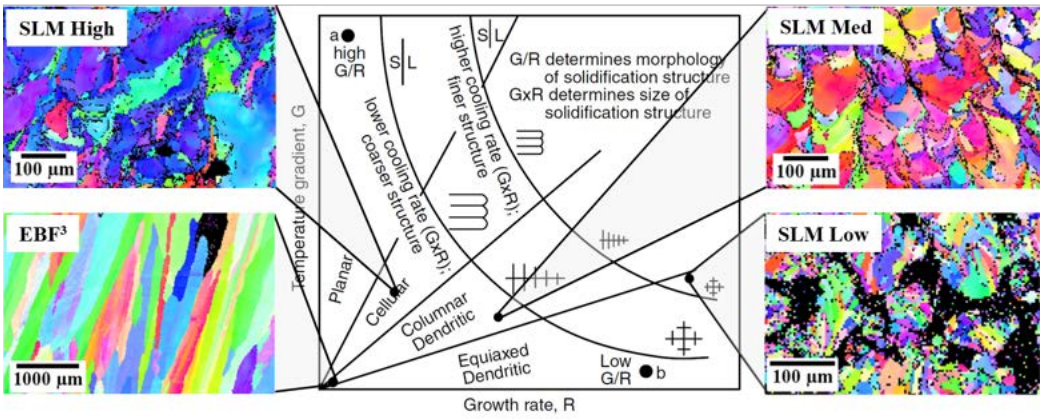

Figure 5.6: Solidification plot from *Welding Metallurgy* qualitatively showing the microstructures and locations of the four sample regions [9].

The processing extremes used for SLM were represented by SLM High and Low, which had the highest and lowest volumetric energy densities (222 and 13.9 J/mm^3). Comparing SLM High and Low, the G and R parameter-structure relationships depicted in Figure 5.6 hold. For SLM Low, $G/R =$ 23.43 K-s/mm^2, and the structure was the most equiaxed structure observed of the four. SLM Low also had the lowest MUD value (1.812) from the pole plots, provided in Figure 5.7a. SLM High (80 W, 0.1 m/s) had the highest predicted G/R value (350 K-s/mm^2), the strongest experimentally observed texture (MUD = 6.401), and a cellular solidification structure. Figure 5.7 contrasts the pole plots of SLM Low against High, underscoring the difference in texture and orientation between the SLM processing extremes.

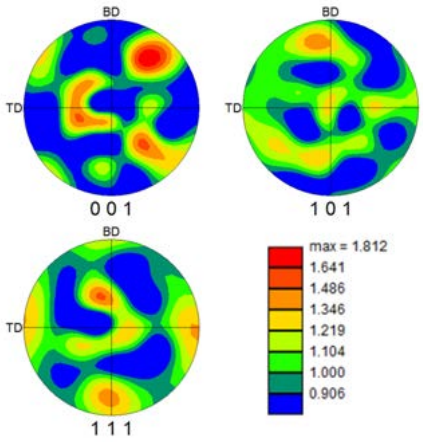

(a) SLM Low (80W, 1.6 m/s) Pole Plot

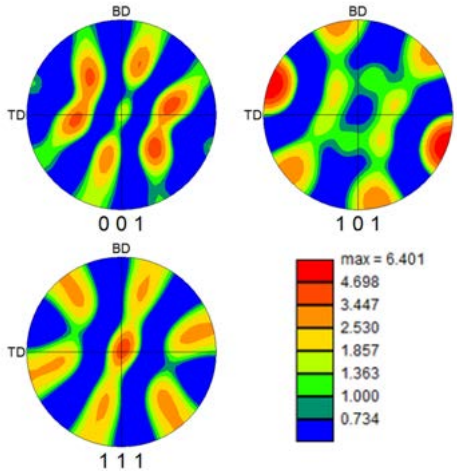

(b) SLM High (80W, 0.1 m/s) Pole Plot

Figure 5.7: Pole plots of SLM Low (80 W, 1.6 m/s) and SLM High (80W, 0.1 m/s). SLM Low (5.7a) shows a low MUD value, and a more even orientation distribution. SLM High (5.7b) has a very strong Goss texture, and a 3.5 times greater MUD value than SLM Low.

In addition to texture and structure differences, the cooling rate impact on grain size is evident between Tables 5.2 and 5.3. The predicted cooling rate of SLM High (3.5 x 10^6 K/s) was seventeen times smaller than SLM Low (6.0 x 10^7 K/s); solidification theory for cooling rates predicts that SLM High will have larger grains than SLM Low. The area-averaged grain diameter for SLM High was 15.98 μm, five times smaller than the grain diameter of SLM Low (80.78 μm). The relationship between low cooling rate and large grain size is repeated again when comparing EBF^3 and all SLM cases. For EBF^3, the area average grain diameter is four orders of magnitude larger than SLM (714.19 μm), with a significantly lower cooling rate. Comparing the four predicted cooling rates and measured grain sizes, a logarithmic trendline is approximated between maximum estimated cooling rate (G·R) and average area grain diameter (Figure 5.8). With a minimal number of samples, the trendline is illustrative, but demonstrates the inverse relationship between grain size and cooling rate.

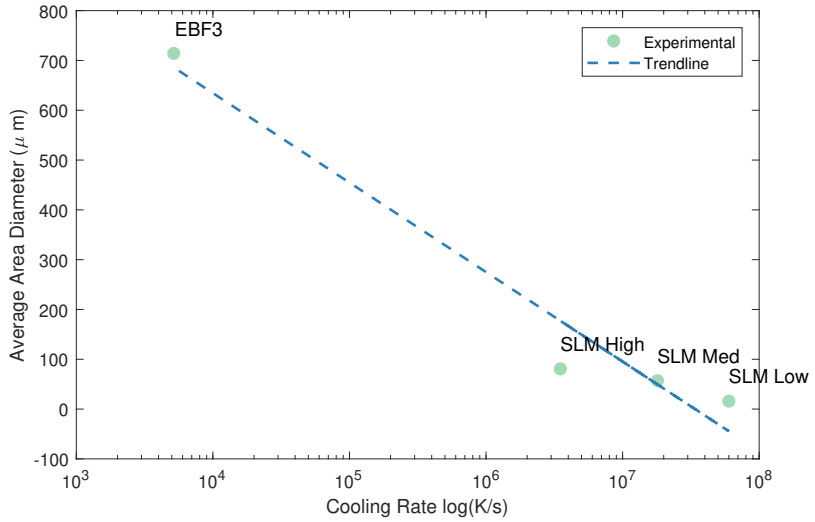

Figure 5.8: Relationship of theoretical maximum cooling rate and measured average grain size. Plotted on a semilog plot, with a logarithmic trend line $y = -78.04ln(x) + 1353.2$ (R^2=0.9583) shown.

The relationships between morphology, cooling rate, grain size, and thermal gradient transcend printing processes, as evidenced by the similarities of EBF^3 and SLM Med. The two samples were considered moderate parameter sets, with good printability and minimal structural defects. Although the melt pool size and cooling rates were different by orders of magnitude, the G/R morphology calculation was similar (EBF^3 = 71.55 K-s/mm^2, SLM Med = 112.5 K-s/mm^2). Moreover, volumetric energy calculations were similar, with EBF^3 E_v= 87.48 J/mm^3, and SLM Med E_v= 76.39 J/mm^3. As seen in Figure 5.5 and Table 5.3, both samples presented a strong Goss texture with epitaxial columnar grains extending through multiple layers. Though SLM Med was less needle-like than EBF^3, the columnar descriptor is appropriate given the epitaxial grain growth through multiple layers and comparison to other SLM microstructures in literature [8].

Further inspection of EBF^3 and SLM Med in Figure 5.5 showed a clear preferred crystal growth direction for EBF^3, but less directionality for SLM Med. The directionality difference is due to the scan speed and solidification direction dependence. With EBF^3, the translation speed only occurred in one direction; each layer was deposited parallel to the previous one. The

repetitive heat input encouraged heterogeneous crystal growth of the easy <100> solidification direction. The new layers continued to apply the thermal gradient in the same direction, propagating the initial crystals through the height of the deposit. In contrast, the SLM scan direction alternated and rotated 15° for each new layer. The rotation encouraged competitive growth and heterogeneous nucleation of crystals, as the maximum thermal gradient direction changed with every laser pass. A more intentional SLM scan pattern, with no layer rotation, will promote growth in a way similar to EBF^3 [15].

5.3 Magnetic Properties

The resultant magnetic properties are divided into two subcategories: structure insensitive and structure sensitive. Structure insensitive properties are dependent only on phase and composition of the sample. The structure insensitive property, saturation magnetization, had little variance and stayed relatively unchanged through varied processing parameters for both EBF^3 and SLM.

The structure sensitive properties vary with microstructure; grain morphology, size, and defect structures can impact the structure sensitive magnetic properties of the material. The structure sensitive magnetic properties, including coercivity, permeability, and hysteresis loss, exhibited statistically significant variations as a function of material processing.

For an optimized soft magnetic material, high saturation magnetization, low coercivity, high permeability, and low hysteresis loss are desired. Focusing on microstructural effects, magnetic domain walls propagate through a sample under an applied magnetic field in a manner analogous to edge dislocations under applied stress. Movement of domain walls is inhibited by grain boundaries and non-magnetic inclusions (e.g. porosity and precipitates). Smaller grains and high porosity are undesirable as they slow the movement of the domain walls, which leads to high coercivity, low permeability, and high hysteresis loss [5, 45].

Additionally, texture impacts domain wall movement. The domain walls have a preferred crystallographic direction for motion, dependent on planar spacing and crystal anisotropy. For FCC, the easy direction of magnetization is <111>, the medium direction is <110>, and the hard direction is <100>

[5]. FeNi will have the most desirable magnetic response if the predominate sample texture <111> is in the direction of the applied magnetic field, and least desirable when the sample texture <100> is oriented with the applied field.

The magnetic properties for the four cases of interest in Section 5.2 are tabulated in Table 5.4. Using Table 5.4 and Figure 5.6, relationships between the microstructure and magnetic response are investigated. Considering the structure sensitive, microstructurally-dependent properties, the EBF^3 case had the smallest measured coercivity and one of the higher permeabilities. The EBF^3 case has large grains and a strong Goss texture which utilizes the medium magnetization direction (<110>). Similarly, the over-melted SLM High had the largest grains produced by SLM and a strong cellular Goss texture and had the lowest SLM coercivity and hysteresis loss. The strong texture and large grain size of EBF^3 and SLM High yielded more desirable coercivity values, trending towards suitable properties for additively manufactured soft magnetic materials.

Table 5.4: Summary of experimentally measured magnetic properties of four representative cases.

	Saturation Magnetization (emu/g)	**Coercivity** (Oe)	**Permeability** (μ)	**Hysteresis Loss** (J/g)
SLM Med	143±2.9	5.8±4.0	160±23	5.62E-4±1.7E-5
SLM High	143±2.8	3.1±0.62	37±3.2	2.8E-4±1.2E-5
SLM Low	140±2.8	6.2±2.6	51±9.9	4.37E-4±2.7E-05
EBF^3	146±2.9	3.3±2.6	131±15	1.63E-3±4.9E-5

However, the small subset of data in Table 5.4 is not effective for extrapolating processing-microstructure-property linkages for all deposited samples. Ultimately, the goal is to evaluate statistically significant relationships between AM parameters and magnetic responses. The Pearson coefficient plots from Sections 4.2.2 and 4.3.2 are recalled in Figure 5.9 to explore the processing-property relationship.

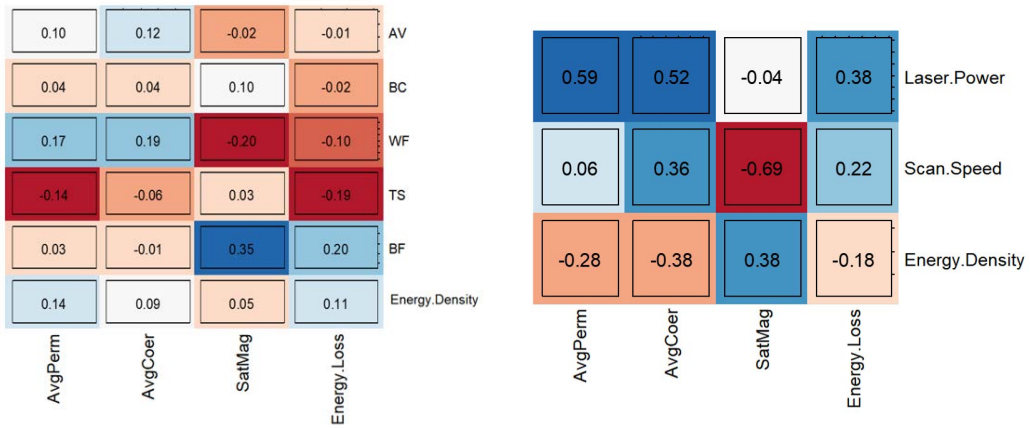

(a) EBF^3 Pearson Coefficients

(b) SLM Pearson Coefficients

Figure 5.9: Heatmap of the Pearson correlation coefficients between processing parameters and magnetic measurements for EBF^3 (5.9a) and SLM (5.9b).

Significant correlations to saturation magnetization included EBF^3 beam focus (r=0.35) and SLM scan speed (r=-0.69). However, the saturation magnetization must show statistically significant variance in order for the correlations to draw meaningful relationships. The implications of these correlations are explored in Section 5.3.1. For structure sensitive properties, high correlations between the SLM laser power and coercivity (r=0.52), SLM scan speed and coercivity (r=0.36), and permeability and SLM laser power (r=0.59) are observed. The correlations for structure sensitive properties are discussed in Section 5.3.2.

5.3.1 Structure Insensitive Magnetic Properties

Two-sided t-tests were performed on the EBF^3 and SLM saturation magnetization values to determine statistical variance between the base material and additively manufactured populations. Table 5.5 compiles the base material measurements (null hypothesis), 95% confidence interval for additively manufactured population mean, and the associated p-value.

Table 5.5: T-tests were performed to determine if saturation magnetization significantly changed due to printing. The structure insensitive property is expected to change only if phase or composition changes.

	Base Material (Null hypothesis)	**Deposits** ($\alpha = 0.05$)	**P-Value**
EBF^3	148.6	[147.2 148.9]	0.1686
SLM	141.93	[141.46 142.67]	0.639

From the 95% confidence intervals tabulated in Table 5.5, neither EBF^3 or SLM processing caused a statistically significant change to the saturation magnetization. Saturation magnetization is a measurement of magnetization once all the magnetic domains have aligned to an applied field and is only dependent on the net magnetic moment of a structure. Saturation magnetization was expected to remain constant through processing, since phase or composition change was not expected.

Both SLM and EBF^3 processes yield FCC, as determined from XRD and EBSD. While Fe50Ni can form an ordered $L1_0$ phase, the printed sample coercivity values for both printing processes (1.152 to 6.073 Oe) indicate that the resulting FCC has no long-range ordering of Fe and Ni and is not the tetragonal $L1_0$ phase (H_c=1200 Oe) [35]. The disordered FCC phase was the expected phase, given the small free energy differences between ordered and disordered Fe50Ni. Though $L1_0$ is stable below 320 °C, diffusion between Fe and Ni is incredibly sluggish (1 atomic jump/10000 years) [36, 76, 77].

Other theoretical work to form $L1_0$ has utilized rapid solidification processes. Laser irradiation has been proposed as a method to introduce crystal defects and vacancies to manufacture faster diffusion paths [78]. $L1_0$ has been formed in 30 μm melt-spun ribbons. Melt spin forming, a high cooling rate solidification process (10^4 to 10^6 K/s), was used to make amorphous Fe50Ni ribbons, which were then annealed at 370 °C [37, 79].

Despite additive manufacturing being a rapid solidification process, additive manufacturing formed disordered FCC over $L1_0$. The molten volume of additive manufacturing is much larger than laser irradiation or melt-spin forming, so the cooling and solidification rates vary throughout the melt pool. While simulations predicted solidification rates on the order of 10^7 K/s, the predicted solidification is an upper bound, in an idealized thermal

gradient. The cooling and solidification rates at other locations within the melt pool were much lower. Moreover, additive manufacturing encourages heterogeneous nucleation and growth, where new layers have preferred growth based on the grain orientation surrounding the local melt pool.

Compositionally, EDS showed minimal variance between starting materials and final depositions. The base wire comprised of 50.0wt% Fe, 49.7wt% Ni, while a final deposit contained 51.3wt% Fe, 48.1wt% Ni. While EDS is a semi-quantitative measurement, it provides support for the minimal magnetic variance. The minimal variance in composition is also supported by vaporization curves. Figure 5.10 presents the equilibrium vapor pressure curves at a given temperature for Ni, Fe, Mn, and Si [80]. These curves indicate expected elemental loss to vaporization. Fe and Ni have similar curves and are expected to vaporize at comparable rates, keeping the composition of the deposits stable during printing.

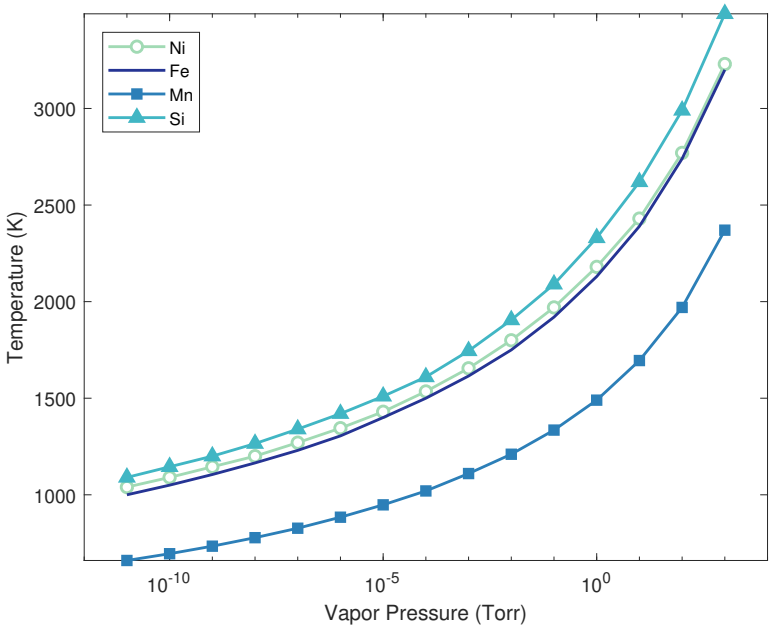

Figure 5.10: Equilibrium vapor pressure curves at a given temperature for Ni, Fe, Mn, and Si [80]. Vapor pressure curves can provide insight into potential elemental loss due to vaporization during the deposition process. At 10^{-4} Torr or lower, the EBF^3 operational range, Mn will vaporize most easily. Ni and Fe have similar curves and will be vaporized at similar rates. At atmospheric pressure, 760 Torr (operating pressure for SLM), Mn will still vaporize most easily, but at a lesser rate than at 10^{-4} Torr.

While minimal, the highest processing-property correlation observed for EBF^3 was saturation magnetization and beam focus (r=0.35). However, as t-testing showed the saturation magnetization did not change significantly from the base wire to final deposits. Moreover, the 95% confidence interval for the saturation magnetization deposits is [147.2 148.9] emu/g, while measurement uncertainty is $\pm$2.95 emu/g. Since the measurement uncertainty is larger than the confidence interval, any variance and correlations are not statistically significant.

The other highly correlated value is the SLM scan speed and saturation magnetization (r=-0.69). While the SLM scan speed and saturation magnetization relationship could indicate a correlation between SLM energy density

and vaporization, based on the low correlation of laser power and saturation magnetization (r=-0.04) it is more likely a remnant of the saturation magnetization computation described in Section 3.5.2. It is observed that higher scan speeds correlate with a slower rate magnetic saturation, so the averaged saturation magnetization is likely lower than the true value at high scan speeds. Figure 5.11 shows the different rates of approaching saturation magnetization for scan speeds 0.1 m/s to 1.6 m/s at 80 W laser power.

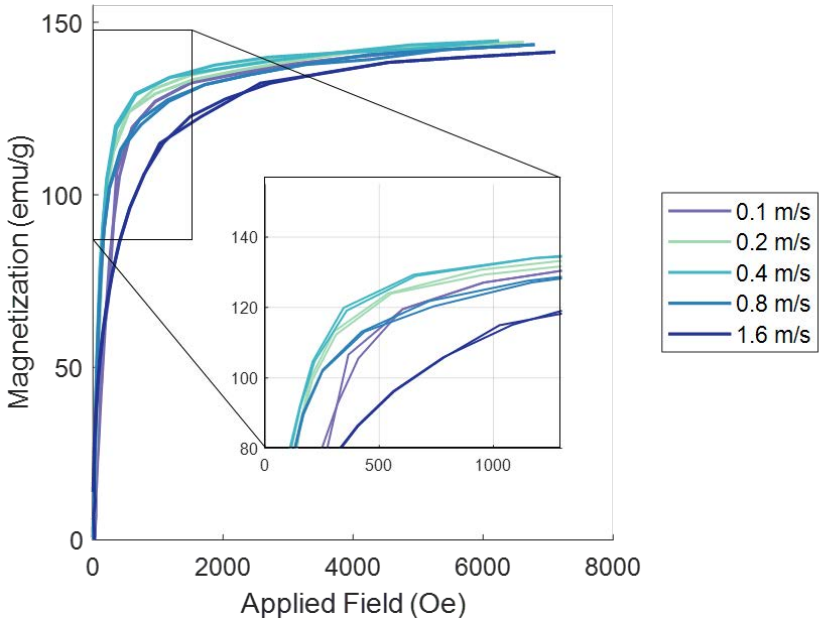

Figure 5.11: Hysteresis loop shape variance for differing SLM scan speeds. Of note, the higher scan speeds approach saturation magnetization at a slower rate than the low speeds at equivalent laser power (80 W).

Given minimal compositional change and no phase transition, a constant saturation magnetization value was expected. Such behavior is supported by Zhang et. al, where various SLM parameter changes resulted in M_s values between 95 emu/g to 99 emu/g for Fe80%Ni [27]. Only research which utilized the BCC-FCC phase transition at Fe30%Ni reported large changes in saturation magnetization (400 to 565 emu/g [19], 120 to 165 emu/g [24]).

5.3.2 Structure Sensitive Magnetic Properties

Grain size, morphology, texture, and non-magnetic inclusions all contribute to the structure sensitive magnetic properties. For this work, the structure sensitive properties of interest are coercivity, permeability, and hysteresis loss. To visualize the relationships between microstructural features and structure sensitive properties, Table 5.6 qualitatively demonstrates the relationships between changing microstructure and magnetic properties.

Table 5.6: Qualitative relationships between microstructural features and structure sensitive magnetic properties. Texture and aspect ratios are anisotropic and are presented with the preferred magnetization direction and elongated grain dimension aligned with the applied magnetic field. Beneficial microstructural properties are shown in green, while detrimental microstructural features are shown in red.

	Increased Grain Size	**Increased Porosity**	**Preferred Texture Strengthening**	**Increased Grain Aspect Ratio**
Coercivity	Decrease	Increase	Decrease	Decrease
Permeability	Increase	Decrease	Increase	Increase
Hysteresis Loss	Decrease	Increase	Decrease	Decrease

Considering coercivity, historical work has been done to theoretically compute the coercivity dependence on grain boundaries, non-magnetic inclusions, and residual stress. Equation 5.3, obtained from *Soft Magnetic Ni-Fe and Co-Fe Alloys - Some Physical and Metallurgical Aspects*, was proposed and experimentally verified by Pfeifer and Radeloff in 1980 [39].

$$H_c = H_{co} + H_{ck} + H_{ci} \tag{5.3}$$

For Equation 5.3, H_c is the measured coercive field, H_{ck} denotes the grain boundary contribution, H_{ci} describes the influence of non-magnetic inclusions, and H_{co} gives a basic coercive field strength, which encompasses magnetostrictive residual stresses.

The influence of grain boundaries, H_{ck} can be calculated using Equation 5.4, using wall energy γ_w, saturation polarization J_s, and grain diameter (d_k) (cm).

$$H_{ck} \approx 3\frac{\gamma_w}{J_s}\frac{1}{d_k} \tag{5.4}$$

The wall energy is further disseminated in Equation 5.5, where k is the Boltzmann constant, T_c is the Curie temperature, a is the lattice constant, and K_1 is the crystal energy.

$$\gamma_w \approx \sqrt{kT_cK_1/a} \tag{5.5}$$

For Fe50Ni, the necessary values to determine H_{ck} are compiled in Table 5.7 [39].

Table 5.7: Magnetic and material constants used to determine wall energy, Bloch-wall thickness, and coercivity constant for Fe50Ni.

		Fe50Ni
Lattice constant a	(m)	3.58E-10
Curie temperature, Tc	(K)	823
Crystal energy, K_1	(Ws/m^3)	800
$3\sqrt{kT_cK_1/a}/J_s$	(mA)	0.3115
Bloch-wall thickness $\delta_w \approx \sqrt{kT_cK_1/a}$	(μm)	0.21

The influence of non-magnetic inclusions can be described by Equation 5.6, where v is volume fraction of non-magnetic inclusions [39].

$$H_c \approx v \tag{5.6}$$

However, non-magnetic inclusions have the most significant impact when the diameter of the inclusion is approximately the Bloch-wall thickness. For $d >> \delta_w$, the effect of the inclusions are considerably reduced. From Table 5.7, the Bloch-wall thickness is 0.21 (μm). From Figure 4.19, the porosity is orders of magnitude larger, on the order of 20 to 150 μ. For this reason, the effect of non-magnetic inclusions was neglected in computing H_c.

Pfeifer and Radeloff set $H_{oc} = 8$ (mA/cm) based on experimental line-of-best-fit for their samples. Since experimental residual stress data is not available, H_{oc} will be treated as a source of error.

Equation 5.3 is applied using Equation 5.7. EBSD average area grain diameter data was used for experimental d_k and Figure 5.12 plots the experimental $\frac{1}{d_k}$

and H_c. A line indicating the predicted coercivities using Equation 5.7 in units of Oe is also plotted.

$$\begin{aligned} H_c &= 0.3115/d_k \text{ (mA/cm)} \\ H_c &= 1.246\pi/d_k \text{ (Oe)} \end{aligned} \tag{5.7}$$

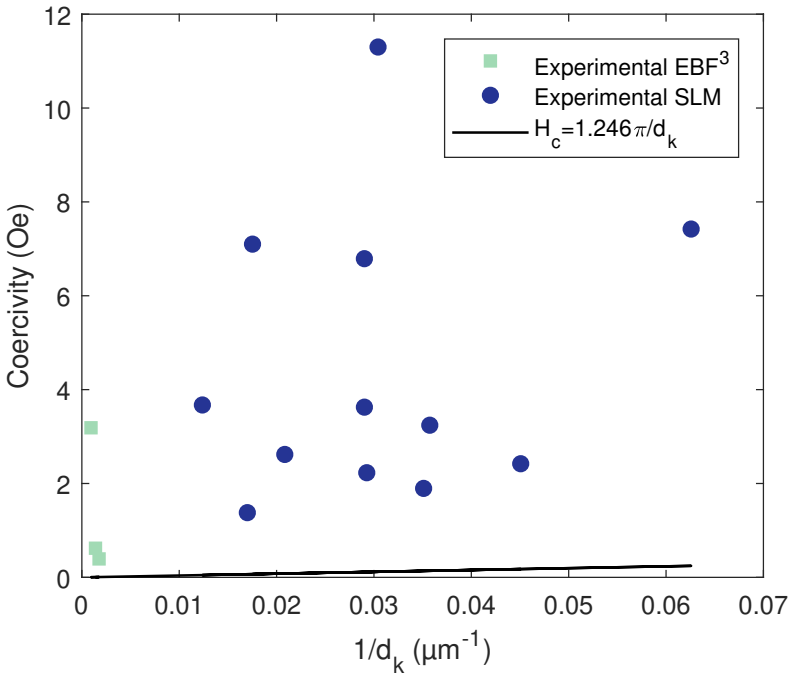

Figure 5.12: Predicted and measured coercivities as a function of inverse grain diameter. The experimental coercivities are represented as a scatter plot. The EBF^3 samples are shown in the lower left quadrant of the plot, below 0.01 μm^{-1}. The black line near the x-axis ($H_c = 1.246\pi/d_k$) is the predicted coercivity, which is significantly less than any of the experimentally measured values.

Figure 5.12 shows that Equation 5.7 underestimates the coercive values obtained experimentally. To understand why, the base assumptions of Equation 5.3 and 5.7 were reviewed [39].

First, the influence of residual stress was assumed to be a source of error. The residual stress influence on coercivity is likely not negligible, given the

residual stresses historically observed during additive manufacturing [81, 8]. In a thin film experiment with Fe80Ni20, a reduction of residual stress from 14.4 to 2.07 GPa through annealing reduced the coercivity from 280 Oe to 120 Oe [82]. For SLM deposited Fe50Ni, Mazeeva et. al showed a reduction from 2.51 to 1.25 Oe between an as-deposited sample and a heat-treated sample, indicating that H_{oc} was $\sim$1.26 Oe [29].

Additionally, Equation 5.4, the model for grain size assumes equiaxed grains. The assumption of equiaxed grains is not valid for the long, columnar grains observed in the EBF^3 samples and samples printed at the lower energy densities with SLM. Moreover, the long, columnar grains can introduce shape anisotropy, increasing coercivity [5].

Finally, Equation 5.3 was only experimentally verified up to a 5 μm grain diameter [39]. The smallest average grain diameter observed in SLM or EBF^3 deposits was 15.98 μm (SLM Low) and the largest was 1064 μm (EBF^3 10-3). Equation 5.3 may not extend into the length scale needed. At the larger grain diameters, subgrains and variations within the grains will contribute more of an effect on the coercivity and domain wall movement.

Though the coercivity was not well-described with theoretical computations, experimental relationships were explored. Since the only moderate correlation obtained from Figure 5.9a was between beam focus and saturation magnetization, additional processing-property correlations for coercivity and permeability of EBF^3 samples will not be discussed further.

From Figure 5.9b, correlations between the SLM laser power and coercivity (r=0.52), scan speed and coercivity (r=0.36), and volumetric energy density and coercivity (r=-0.38) are observed. The scan speed-coercivity relationship is able to be directly explained. As the scan speed increases (and volumetric energy decreases), metallurgical characterization shows that the porosity increases, grain size decreases, and easy magnetization texture direction decreases. All three of the microstructural observations lead to more difficult domain wall propagation, which will raise the coercivity value.

The correlation between laser power and coercivity (r=0.52) is believed to be an artifact of the trilevel (50, 80, 110 W) distribution of the beam power. The error associated with the coercivity computation increases significantly at 110 W. To avoid the impact of outliers, lines of best fit with R^2 less than 0.7 were discarded, leaving 2 measurements at 110 W. With only 2 observations

present at higher laser power, and only three total laser power levels, the 2 observations (with ±4 Oe error), artificially inflated the linear Pearson correlation value. The discarding of this correlation is supported by the correlations between scan speed, volumetric energy density, and coercivity, which are more robust in level and data distribution.

The correlation coefficient permeability and SLM laser power (r=0.59) is also assumed to be a discardable artifact. However, experimental measurements support this trend. From Table 4.9, higher power for the same scan speed trended towards larger grains and stronger texture. Both larger grain size and stronger texture would increase the permeability, which is beneficial for soft magnetic applications.

Coercivity and permeability values from EBF^3 and SLM can be compared to results from literature for both historical manufacturing techniques and SLM.

Table 5.8: Permeability, coercivity, and hysteresis loss values compiled from published literature on historical manufacturing techniques, the selective laser melting of Fe50Ni, and the electron beam freeform fabrication of Fe50Ni

	EBF^3 ($\alpha = 0.05$)	**SLM** ($\alpha = 0.05$)	**As-Built SLM** [29]	**Heat-Treated SLM (1300 °C, 6 hr)** [29]	**Cold-Rolled Traditional** [38]
Coercivity (H_c)	[1.152 1.727] Oe	[3.575 6.073] Oe	200 A/m (2.51 Oe)	100 A/m (1.25 Oe)	2.5 Oe
Permeability (μ_{max})	[47.16 70.61]	[50.36 82.97]	1000	5000	8e5
Hysteresis Loss (W_L)	[3.9E-4 7.3E-4] J/g	[4.4E-4 6.2E-4] J/g	–	–	1.7E-7 J/g
Grain size	565.7-1064 µm	15.98-80.78 µm	10-100 µm	10-100 µm	–

The coercivity values listed in Table 5.8 show that EBF^3 had competitively low values, while SLM was higher than literature values. The low coercivity associated with EBF^3 indicates that EBF^3 produced soft magnetic components may have merit. The grain sizes obtained with SLM are comparable to the literature for SLM processing. However, permeability for both EBF^3 and SLM are significantly lower than other additively manufactured processes and traditionally produced Fe50Ni.

The low permeability values were unexpected. It is hypothesized that the permeability values may not have been accurately corrected for shape due to the high demagnetization correction factor and field. While the rectangular

prisms provided a method of measuring the bulk response of the deposited material, a more elongated bar shape would have required a smaller demagnetizing field correction. Given the length scale of EBF^3, using elongated samples would introduce local layer effects and the elongated sample may not describe the bulk deposition. Figure 4.18 in Section 4.2.2 discusses the magnetic and microstructural variation present between the middle layers and the top layer. Finally, the permeability was estimated from the slope of B/H through the x-intercepts of the hysteresis loop, which underestimates the permeability (Section 3.5.2). The reported permeability values for EBF^3 and SLM are all less than or equal to the actual permeability of the samples. Higher resolution initial magnetization curves would be needed for a more accurate permeability measurements.

Hysteresis loss was poor for both EBF^3 and SLM. The hysteresis loss per cycle for commercial Hipernik (55Fe-45Ni) is $1.7\text{x}10^{-7}$ J/g, which is three orders of magnitude smaller than EBF^3 or SLM hysteresis loss [38]. To reduce hysteresis loss, higher energy densities to strengthen texture and increase grain size can be used.

Chapter 6
Conclusions

Research was conducted to evaluate the magnetic properties of Fe50Ni using additive manufacturing methods. Two different additive methods, SLM and EBF^3, were used to fabricate 80 EBF^3 and 36 SLM samples, 87 (51 EBF^3 and 36 SLM) of which were characterized magnetically and metallurgically. The printability of a novel alloy, the microstructural effects of solidification rate from two different printing processes, and the influence of the printing processes on the magnetic properties of the material were investigated.

Fe50Ni was successfully printed using both EBF^3 and SLM. The EBF^3 depositions exhibited excellent printability, with good surface finishes, no visible porosity, and no cracking. In comparison, the SLM samples resulted in a wide printability map, yielding both good and poor quality samples. The best quality SLM sample, 10-1 / SLM Med, had a good optical surface finish and minimal porosity. SLM Med was deposited at a volumetric energy density of 76.39 J/mm^3, which was comparable to literature (60.93 to 83.33 J/mm^3) and EBF^3 (87.48 J/mm^3)[29, 30].

In addition, the two printing processes resulted in significantly different melt pool sizes, which yielded orders of magnitude different deposition, solidification, and cooling rates. The predicted maximum cooling rate for high quality samples was 5.2x10^{-3} K/s for EBF^3 and 1.8x10^{-7} K/s for SLM, which led to the grain diameter variation between the two processes: 566 to 1064 μm for EBF^3 and 16 to 81 μm for SLM. While the cooling rates impacted grain size, epitaxial growth and columnar grains were seen across print processes for samples with good printability.

The structure insensitive magnetic property, saturation magnetization (M_s), had little variance and stayed relatively unchanged through varied processing parameters for both EBF^3 and SLM. All printed samples were shown to be disordered FCC, with saturation magnetization values ranging from 141 to 148 emu/g, near the literature value of 154 emu/g for Fe50Ni. No significant change in saturation magnetization was observed between the initial materials and

the final samples, which is consistent with unchanging phase and composition through the printing process.

In general, large grains, minimal porosity, and preferred texture orientation are desired to enhance the structure sensitive magnetic properties and encourage low coercivity. Overall, EBF^3 generated lower coercivity values in comparison to SLM printed samples. The EBF^3 samples had large FCC columnar grains and a strong Goss texture, both of which are favorable for the intrinsic properties of soft magnetic Fe50Ni. The low coercivity associated with EBF^3 indicates that soft magnetic components produced with EBF^3 may have merit.

Future Work

Further work is needed to draw robust conclusions on the impact of additive manufacturing on the intrinsic magnetic properties of Fe50Ni. First, magnetic measurements on samples with lower demagnetization factors are needed. A more elongated bar shape would remove the error associated with the correction factors, providing more accurate permeability measurements. Similarly, more deposition and magnetic data are needed to better determine the correlations between processing parameters and magnetic response.

Extending the work, two areas of additional investigation arise. First, methods of post-processing could be considered. Typical Fe-Ni components are hydrogen heat-treated, which greatly reduces residual stress and improves permeability. Mazeeva et. al successfully reduced the coercivity and increased permeability after heat-treating SLM-deposited Fe50Ni, indicating potential for improved properties through heat-treatment [29].

Second, the possibility of scaling the results of this thesis to applications can be explored by considering larger deposits and the development of a test article. This thesis performed fundamental research to determine the potential for additively manufactured Fe50Ni, while a future extension could assess the application of the research to a demonstration component.

The results of this initial research suggest that AM soft magnets have potential but further development is required. The ability to achieve the desired properties with AM would enable more intricate, customizable, and efficient soft magnetic components.

Appendices

Appendix A
EBF^3 Parameter Sets

Table A.1: EBF^3 VSM Cube Dimensions and Demagnetization Factors

Sample	AV (kV)	BC (mA)	WF (ipm)	TS (ipm)	BF	E_L (kJ/in)
8-1	30	85	40	20	318	7.65
8-2	30	85	50	20	318	7.65
8-3	30	85	30	20	318	7.65
8-4	30	95	40	20	318	8.55
8-5	30	75	40	20	318	6.75
8-6	30	85	40	15	318	10.2
8-7	30	85	40	30	318	5.1
8-8	30	85	40	20	318	7.65
8-9	30	85	40	20	318	7.65
8-10	40	100	95	20	318	12
9-1	30	75	40	20	318	6.75
9-2	30	100	40	20	318	9
9-3	30	95	40	20	318	8.55
9-4	30	90	40	20	318	8.1
9-5	30	80	40	20	318	7.2
9-6	30	85	40	20	318	7.65
9-7	30	85	40	20	318	7.65
9-9	30	75	40	20	318	6.75
9-10	30	100	40	20	318	9
10-1	30	85	40	10	323	15.3
10-2	30	85	40	15	323	10.2
10-3	30	85	40	20	323	7.65
10-4	30	85	40	25	323	6.12
10-5	30	85	40	30	323	5.1
10-6	30	85	40	35	323	4.37
10-7	30	85	40	40	323	3.825
10-8	30	85	40	45	323	3.4
10-9	30	85	40	50	323	3.06
10-10	30	85	40	55	323	2.78

Continued on next page

Table A.1 – *Continued from previous page*

Sample	AV (kV)	BC (mA)	WF (ipm)	TS (ipm)	BF	E_L (kJ/in)
11-1	30	60	40	20	323	5.4
11-2	30	70	40	20	323	6.3
11-3	30	75	40	20	323	6.75
11-4	30	80	40	20	323	7.2
11-5	30	85	40	20	323	7.65
11-6	30	90	40	20	323	8.1
11-7	30	100	40	20	323	9
11-8	30	110	40	20	323	9.9
11-9	30	120	40	20	323	10.8
11-10	30	85	40	20	323	7.65
12-2	25	85	40	20	323	6.37
12-3	30	85	40	20	323	7.65
12-4	35	85	40	20	323	8.92
12-5	27.5	85	40	20	323	7.01
12-6	32.5	85	40	20	323	8.28
12-7	30	85	40	20	323	7.65
12-8	30	85	40	20	323	7.65
12-9	30	85	40	20	323	7.65
12-10	30	85	40	20	323	7.65
15-7	30	85	40	20	333	7.65
15-8	30	85	40	20	313	7.65

Appendix B
VSM Sample and Demagnetization Calculations

Table B.1: Initial Material Cylindrical Dimensions and Demagnetization Factors

	Diameter D (mm)	Height H (mm)	Mass (mg)	Density (g/cm^3)	Aspect Ratio D/H	N_d
Wire	1.60	6.85	101.94	7.98	4.285	0.047
Powder	3.96	2.08	46.71	5.73	0.9166	0.1867

Table B.2: EBF^3 VSM Cube Dimensions and Demagnetization Factors

	Front c (mm)	Side a (mm)	Height b (mm)	Mass (mg)	Density (g/cm^3)	Aspect Ratio ($c/\sqrt{ab}$)	Aspect Ratio b/a	N_d
8-1	4.22	3.86	6.68	861.37	7.92	0.8302	1.7303	0.3289
8-2	4.17	3.84	6.27	821.42	8.19	0.8492	1.6358	0.3232
8-3	3.94	3.63	3.96	450.18	7.94	1.0378	0.9167	0.2599
8-4	4.04	3.45	5.99	677.62	8.10	0.8875	1.7353	0.3086
8-5	4.01	3.23	5.49	570.93	8.04	0.9540	1.7008	0.2853
8-6	4.01	4.24	5.89	791.91	7.89	0.8027	1.3892	0.3426
8-7	3.96	3.66	4.60	543.01	8.15	0.9663	1.2569	0.2847
8-8	4.01	3.81	5.51	683.11	8.11	0.8758	1.4467	0.3157
8-9	4.06	3.81	6.05	755.37	8.07	0.8468	1.5867	0.3246
8-10	4.19	4.42	7.59	1128.33	8.02	0.7234	1.7184	0.3669
9-1	5.36	3.61	4.60	722.43	8.13	1.3161	1.2746	0.2248
9-2	5.08	3.10	6.02	758.04	8.00	1.1762	1.9426	0.2411
9-3	4.83	2.92	6.65	723.47	7.71	1.0946	2.2783	0.2507
9-4	4.37	4.22	4.52	669.64	8.04	1.0006	1.0723	0.2738
9-5	4.17	4.04	5.51	755.50	8.15	0.8829	1.3648	0.3139
9-6	4.14	2.69	6.48	579.17	8.02	0.9914	2.4057	0.2652
9-7	4.09	4.09	5.82	751.24	7.72	0.8385	1.4224	0.3294
9-9	3.96	3.68	5.28	621.22	8.06	0.8983	1.4345	0.3077
9-10	4.01	4.34	6.10	842.67	7.93	0.7799	1.4035	0.3507
10-1	5.82	6.15	8.53	2374.80	7.78	0.8035	1.3870	0.3424
10-2	5.74	4.41	7.32	1490.77	8.05	1.0103	1.6599	0.2678
10-3	5.79	3.68	6.44	1063.64	7.75	1.1894	0.5714	0.2405
10-4	5.3	3.86	5.42	858.10	7.74	1.1587	1.4041	0.2475
10-5	5.64	3.68	4.68	725.08	7.46	1.3590	1.2717	0.2184
10-6	4.74	3.91	4.58	650.09	7.66	1.1201	1.1714	0.2550
10-7	4.84	3.55	4.16	537.88	7.53	1.2595	1.1718	0.2340
10-8	4.74	2.64	4.32	423.67	7.84	1.4036	1.6364	0.2094
10-9	4.9	3.29	3.68	439.19	7.40	1.4082	1.1185	0.2120
10-10	4.64	2.99	3.38	364.27	7.77	1.4596	1.1304	0.2041
11-1	5.26	3.48	7.24	1053.28	7.95	1.0479	2.0805	0.2659
11-2	5.18	4.09	5.83	947.00	7.67	1.0608	1.4254	0.2620

Continued on next page

Table B.2 – *Continued from previous page*

	Front c (mm)	Side a (mm)	Height b (mm)	Mass (mg)	Density (g/cm^3)	Aspect Ratio ($c/\sqrt{ab}$)	Aspect Ratio b/a	N_d
11-3	4.51	2.88	7.27	719.35	7.62	0.9856	2.5243	0.2659
11-4	5.17	4.03	6.47	1047.73	7.77	1.0125	1.6055	0.2679
11-5	4.88	4.18	6.22	965.47	7.61	0.9571	1.4880	0.2861
11-6	3.81	3.4	5.03	504.03	7.74	0.9213	1.4794	0.2990
11-7	5.39	4.43	5.15	926.33	7.53	1.1285	1.1625	0.2538
11-8	5.35	4.5	5.22	992.33	7.90	1.1039	1.1600	0.2576
11-9	4.51	4.33	5.67	878.56	7.93	0.9102	1.3095	0.3046
11-10	5.55	3.4	4.62	650.71	7.46	1.4003	1.3588	0.2116
12-2	3.93	3.39	7.13	710.92	7.48	0.7994	2.1032	0.3350
12-3	4.54	3.85	4.62	636.76	7.89	1.0765	1.2000	0.2614
12-4	3.91	4.85	5.08	765.10	7.94	0.7877	1.0474	0.3521
12-5	3.95	4.01	6.54	816.43	7.88	0.7713	1.6309	0.3510
12-6	2.73	4.76	5.37	535.48	7.67	0.5400	1.1282	0.2310
12-7	4.47	3.47	3.68	443.30	7.77	1.2509	1.0605	0.2361
12-8	4.59	4.1	6.75	982.94	7.74	0.8725	1.6463	0.3148
12-9	3.44	4.3	5.69	652.30	7.75	0.6955	1.3233	0.3823
12-10	4.41	3.98	6.5	850.16	7.45	0.8670	1.6332	0.3169
15-7	3.79	3.81	4.79	559.59	8.09	0.8872	1.2572	0.3135
15-8	3.84	3.8	4.55	531.06	8.00	0.9235	1.1974	0.3008

Table B.3: SLM VSM Cube Dimensions and Demagnetization Factors

	Front c (mm)	Side a (mm)	Height b (mm)	Mass (mg)	Density (g/cm^3)	Aspect Ratio ($c/\sqrt{ab}$)	Aspect Ratio b/a	N_d
1-1	5.15	5.04	4.71	904.54	7.4	1.057	0.9345	0.2693
1-2	5.14	5.13	4.35	840.24	7.33	1.088	0.8480	0.2642
1-3	5.13	5.19	4.47	884.49	7.43	1.065	0.8613	0.2678
2-1	5.07	5.10	4.2	802.77	7.39	1.096	0.8235	0.2629
2-2	5.07	5.11	4.42	832.48	7.27	1.067	0.8650	0.2675
2-3	5.02	5.07	5.26	1006.24	7.52	0.972	1.0375	0.2997
3-1	5.01	5.07	4.11	687.75	6.59	1.098	0.8107	0.2625
3-2	4.95	5.02	4.51	759.36	6.78	1.040	0.8984	0.2717
3-3	4.99	5.00	4.46	761.18	6.84	1.057	0.8920	0.2692
4-1	4.93	4.99	4.58	635.19	5.64	1.031	0.9178	0.2732
4-2	4.91	4.94	4.25	582.36	5.65	1.072	0.8603	0.2668
4-3	4.99	4.98	5.1	700.43	5.53	0.990	1.0241	0.2877
5-1	5.23	5.15	4.94	928.77	6.98	1.037	0.9592	0.2725
5-2	5.24	5.20	4.18	810.48	7.12	1.124	0.8038	0.2585
5-3	5.21	5.28	4.33	845.76	7.1	1.090	0.8201	0.2638
6-1	5.03	5.15	4.02	742.05	7.13	1.106	0.7806	0.2612
6-2	5.07	5.02	4.02	774.31	7.57	1.129	0.8008	0.2577
6-3	5.09	5.08	4.33	810.53	7.24	1.085	0.8524	0.2646
7-1	4.97	5.00	4.48	850.53	7.64	1.050	0.8960	0.2702
7-2	4.98	5.01	5.19	957.04	7.39	0.977	1.0359	0.2970
7-3	4.97	5.03	4.57	863.15	7.56	1.037	0.9085	0.2723
8-1	4.95	4.97	4.17	689.71	6.72	1.087	0.8390	0.2643
8-2	4.85	4.93	5.34	879.5	6.89	0.945	1.0832	0.3207
8-3	4.92	4.93	4.63	760.54	6.77	1.030	0.9391	0.2735
9-1	4.86	4.92	5.01	664.82	5.55	0.979	1.0183	0.2930
9-2	4.88	4.93	4.93	623.34	5.26	0.990	1.0000	0.2839
9-3	4.86	4.90	4.71	610.98	5.45	1.012	0.9612	0.2764

Continued on next page

Table B.3 – *Continued from previous page*

	Front c (mm)	Side a (mm)	Height b (mm)	Mass (mg)	Density (g/cm^3)	Aspect Ratio ($c/\sqrt{ab}$)	Aspect Ratio b/a	N_d
10-1	4.94	4.98	4.09	808.65	8.04	1.095	0.8213	0.2590
10-2	4.91	4.95	4.47	887.43	8.17	1.044	0.9030	0.2702
10-3	4.96	4.98	4.1	820.41	8.1	1.098	0.8233	0.2606
11-1	4.89	4.93	3.98	747.56	7.79	1.104	0.8073	0.2615
11-2	4.86	4.88	4.09	789.79	8.14	1.088	0.8381	0.2642
11-3	4.89	4.92	4.3	823.77	7.96	1.063	0.8740	0.2681
12-1	4.83	4.90	4.41	652.18	6.25	1.039	0.9000	0.2719
12-2	4.86	4.93	4.29	647.42	6.3	1.057	0.8702	0.2691
12-3	4.85	4.85	4.25	626.46	6.27	1.068	0.8763	0.2674

Appendix C
Magnetic Properties

Table C.1: EBF^3 magnetic properties

	Sat. Mag. (emu/g)		Coercivity (Oe)		Permeability		R_1^2	R_2^2	Hyst. Loss (J/g)	
	μ	σ	μ	σ	μ	σ			μ	σ
8-1	146	2.92	3.338	2.685	130.9	14.59	0.9898	0.9898	1.63E-03	4.89E-05
8-2	145.8	2.916	2.916	2.001	122.9	12.23	0.9902	0.9940	3.78E-04	1.13E-05
8-3	146.2	2.923	0.3348	0.1357	16.12	1.528	0.9990	0.9989	1.76E-04	5.29E-06
8-4	145.4	2.907	1.376	0.9247	53.08	5.309	0.9934	0.9940	1.28E-04	3.84E-06
8-5	146.1	2.922	0.7418	0.3301	33.33	2.431	0.9980	0.9985	3.10E-04	9.29E-06
8-6	145.7	2.914	9.436	28.18	241.9	240.6	0.5048	0.5250	2.33E-03	6.98E-05
8-7	146.5	2.93	2.841	2.044	102.1	11.17	0.9917	0.9894	1.89E-03	5.67E-05
8-8	145.7	2.913	1.932	1.461	75.62	8.087	0.9910	0.9923	1.04E-04	3.11E-06
8-9	146.7	2.934	2.473	2.222	105.5	13.52	0.9868	0.9865	1.35E-04	4.06E-06
8-10	144.5	2.889	2.2	1.059	85.24	6.221	0.9959	0.9969	1.73E-04	5.18E-06
9-1	147.4	2.948	0.3258	0.1359	17.15	1.508	0.9992	0.9992	9.70E-05	2.91E-06
9-2	148.4	2.968	1.298	0.6883	55.51	3.906	0.9974	0.9974	1.48E-04	4.45E-06
9-3	148.2	2.965	0.7967	0.6076	33.35	3.347	0.9957	0.9950	2.64E-04	7.93E-06
9-4	146.8	2.936	0.8034	0.2827	31.87	2.217	0.9986	0.9986	1.65E-04	4.95E-06
9-5	147.9	2.958	2.131	1.331	76.23	7.496	0.9925	0.9936	6.03E-04	1.81E-05
9-6	147.6	2.953	1.011	0.6604	38.78	3.866	0.9945	0.9952	1.41E-04	4.23E-06
9-7	147.4	2.948	0.7384	0.4772	35.32	2.942	0.9972	0.9969	3.33E-04	1.00E-05
9-9	146.5	2.93	0.9346	0.4243	36.05	2.781	0.9976	0.9977	4.28E-04	1.28E-05
9-10	144.3	2.885	1.275	0.6815	48.33	4.02	0.9957	0.9968	1.56E-04	4.69E-06
10-1	146	2.92	4.496	19.72	241.7	159.3	0.6843	0.7318	3.65E-04	1.09E-05
10-2	149.6	2.993	0.7139	0.3718	32.64	2.505	0.9982	0.9978	2.56E-04	7.69E-06
10-3	150	2.999	1.521	0.8568	67.6	4.582	0.9970	0.9976	8.11E-05	2.43E-06
10-4	148.3	2.966	0.8346	0.343	31.24	2.374	0.9980	0.9984	4.42E-04	1.33E-05
10-5	145.3	2.905	0.2865	0.09558	14.28	1.321	0.9996	0.9995	9.51E-05	2.85E-06
10-6	146.9	2.938	0.769	0.2299	26.5	1.866	0.9989	0.9990	2.38E-04	7.13E-06
10-7	148	2.961	0.7664	0.3218	25.7	2.233	0.9966	0.9989	2.14E-04	6.43E-06
10-8	149.4	2.988	2.51	1.65	90.86	8.235	0.9964	0.9919	9.02E-05	2.71E-06
10-9	144.7	2.893	0.9623	0.3573	34.59	2.359	0.9985	0.9986	2.20E-03	6.59E-05
10-10	149.3	2.987	1.102	0.3053	35.26	2.157	0.9990	0.9990	1.68E-04	5.04E-06
11-1	145.8	2.916	1.592	0.8203	69.66	4.57	0.9973	0.9976	7.61E-04	2.28E-05
11-2	150.4	3.008	1.173	0.685	51.77	3.789	0.9974	0.9971	1.28E-03	3.84E-05
11-3	149.6	2.991	1.123	0.7935	46.74	4.19	0.9968	0.9942	9.59E-04	2.88E-05
11-4	149.3	2.987	1.222	0.6455	48.69	3.567	0.9974	0.9973	1.31E-03	3.93E-05
11-5	149	2.98	0.9267	0.7906	42.9	4.361	0.9965	0.9914	1.60E-03	4.79E-05
11-6	152.8	3.055	1.744	1.152	74.54	5.791	0.9964	0.9957	1.48E-03	4.45E-05
11-7	152.9	3.057	1.172	0.631	48.04	3.452	0.9976	0.9975	1.61E-03	4.82E-05
11-8	152	3.04	1.341	0.8097	61.27	4.441	0.9966	0.9974	1.31E-03	3.94E-05
11-9	153.1	3.062	-4.813	25.46	-165.1	109	0.7186	0.7060	1.02E-03	3.06E-05
11-10	151.2	3.025	0.3317	0.2053	15.06	1.705	0.9977	0.9983	1.23E-03	3.69E-05
12-2	140.8	2.817	0.6415	0.3916	25.59	2.543	0.9965	0.9966	1.91E-04	5.73E-06
12-3	153.1	3.062	1.936	1.323	91.32	7.002	0.9962	0.9956	4.03E-04	1.21E-05
12-4	150.3	3.006	-3.001	9.8	-79.94	42.13	0.9953	0.7228	4.62E-04	1.39E-05

Continued on next page

Table C.1 – *Continued from previous page*

	Sat. Mag. (emu/g)		Coercivity (Oe)		Permeability		R_1^2	R_2^2	Hyst. Loss (J/g)	
	μ	σ	μ	σ	μ	σ			μ	σ
12-5	150.2	3.003	3.175	45.08	104.4	615	0.0212	0.0374	3.99E-04	1.20E-05
12-6	146.2	2.923	0.214	0.1263	9.372	1.443	0.9980	0.9981	1.44E-03	4.32E-05
12-7	150.6	3.012	2.645	2.164	129.8	11.12	0.9943	0.9941	1.77E-03	5.30E-05
12-8	150.6	3.011	4.49	4.986	194.6	31.49	0.9838	0.9701	4.83E-04	1.45E-05
12-9	152.5	3.051	-2.785	24.53	-107.8	109.9	0.5851	0.4507	6.99E-04	2.10E-05
12-10	151.1	3.023	2.928	2.191	117.9	11.47	0.9919	0.9931	7.77E-04	2.33E-05
15-7	136.3	2.726	1.675	1.429	72.31	7.988	0.9905	0.9917	1.90E-03	5.70E-05
15-8	139.2	2.783	1.007	0.44	41	2.833	0.9983	0.9978	1.73E-03	5.18E-05

Table C.2: SLM magnetic properties

	Sat. Mag. (emu/g)		Coercivity (Oe)		Permeability		R_1^2	R_2^2	Hyst. Loss (J/g)	
	μ	σ	μ	σ	μ	σ			μ	σ
1-1	143.9	2.878	1.377	0.5607	39.58	3.082	0.9975	0.9972	3.02E-04	9.05E-06
1-2	142.4	2.848	3.007	1.219	39.78	5.837	0.9904	0.9831	5.48E-04	1.64E-05
1-3	143.8	2.876	3.486	0.9467	43.42	4.521	0.9949	0.9927	5.91E-04	1.77E-05
2-1	143.3	2.865	2.237	0.9322	56.32	4.837	0.9957	0.9955	3.98E-04	1.19E-05
2-2	141.2	2.825	1.78	0.7465	36.14	3.692	0.9930	0.9964	1.46E-04	4.39E-06
3-1	141.8	2.837	1.95	0.8886	42.69	3.881	0.9955	0.9959	2.72E-04	8.17E-06
3-2	143	2.86	4.123	1.705	73.86	7.426	0.9934	0.9922	5.58E-04	1.67E-05
3-3	140.1	2.803	5.724	1.806	61.02	8.14	0.9862	0.9883	5.27E-04	1.58E-05
4-1	140	2.800	2.49	0.9583	42.14	3.909	0.9961	0.9949	3.54E-04	1.06E-05
4-2	140.6	2.811	5.803	4.629	44.66	14.76	0.8663	0.9717	4.45E-04	1.33E-05
5-1	141.9	2.838	4.049	2.263	28.4	7.729	0.9385	0.9619	2.80E-04	8.41E-06
5-2	142.6	2.852	1.306	0.6243	36.61	3.154	0.9966	0.9969	4.01E-04	1.20E-05
5-3	140.7	2.814	2.084	0.5553	30.24	2.891	0.9959	0.9969	6.98E-04	2.09E-05
6-1	143.4	2.869	2.677	1.187	66.97	5.663	0.9952	0.9956	7.02E-04	2.11E-05
6-2	143.8	2.877	7.224	6.552	77.76	25.74	0.8833	0.9368	3.14E-04	9.43E-06
6-3	144.1	2.883	4.71	1.693	56.64	7.578	0.9895	0.9852	5.85E-04	1.76E-05
7-1	143	2.861	3.908	1.407	93.94	7.508	0.9960	0.9949	7.03E-04	2.11E-05
7-2	143.7	2.874	13.94	18.84	161.6	103.7	0.7752	0.6605	5.67E-04	1.70E-05
7-3	142.9	2.858	10.3	4.281	116.1	19.53	0.9825	0.9705	8.11E-04	2.43E-05
8-1	142	2.839	3.605	1.62	80.55	7.373	0.9950	0.9931	5.40E-04	1.62E-05
8-2	144.3	2.886	-0.1105	35.29	12.52	109.7	0.0141	0.0105	7.07E-04	2.12E-05
8-3	142.8	2.855	11.57	6.207	112.5	27.83	0.9454	0.9527	1.21E-03	3.63E-05
9-1	139.4	2.788	9.159	9.799	65.04	35.38	0.8103	0.7710	4.37E-04	1.31E-05
9-2	140.4	2.809	3.541	2.278	51.62	8	0.9828	0.9829	4.00E-04	1.20E-05
9-3	140.3	2.807	6.172	2.602	51.82	9.875	0.9748	0.9715	8.86E-04	2.66E-05
10-1	143.1	2.862	5.827	4.065	160	23.69	0.9854	0.9765	5.66E-04	1.70E-05
10-2	142.4	2.849	13.5	47.44	161	406.7	0.1765	0.1079	8.96E-04	2.69E-05
10-3	142.8	2.856	27.62	25.16	311.5	200.8	0.6763	0.7842	7.51E-04	2.25E-05
11-1	141.5	2.83	22.79	30.51	262.3	221.5	0.5755	0.6175	5.70E-04	1.71E-05
11-2	140.4	2.809	-8.114	30.94	-164.1	163.8	0.6699	0.3683	3.94E-04	1.18E-05
11-3	141.9	2.837	-8.066	46.36	-123.5	285	0.2797	0.0672	9.29E-04	2.79E-05
12-1	141.7	2.833	10.31	21.42	198	169.7	0.5802	0.6050	3.20E-04	9.60E-06
12-2	140.2	2.803	12.24	24.02	111.9	128	0.4352	0.4628	1.07E-03	3.20E-05
12-3	139.6	2.792	13.62	15.22	121.5	74.15	0.7997	0.6965	6.24E-04	1.87E-05

Bibliography

[1] M. C. Halbig and J.-A. S. Hocker, "Camiem: Compact additively manufactured innovative electric motor," Tech. Rep. GRC-E-DAA-TN74521, 2019.

[2] T. Hirooki, K. Shoichi, and E. Yuji, "High-efficiency motors using soft magnetic cores," *Electrical Engineering in Japan*, vol. 189, no. 2, pp. 45–53, 2014.

[3] C. W. T. McLyman, *High Reliability Magnetic Devices: Design & Fabrication*, vol. 115. CRC Press, 2002.

[4] B. M. Moskowitz, *Classes of Magnetic Materials*. University of Minnesota Institute for Rock Magnetism.

[5] B. Cullity and C. Graham, *Introduction to Magnetic Materials*. Wiley, 2011.

[6] D. H. Föll, *Magnetic Materials: Hard and Soft Magnets*. University of Kiel.

[7] N. R. Center, "The hysteresis loop and magnetic properties."

[8] T. DebRoy, H. Wei, J. Zuback, T. Mukherjee, J. Elmer, J. Milewski, A. Beese, A. Wilson-Heid, A. De, and W. Zhang, "Additive manufacturing of metallic components process, structure and properties," *Progress in Materials Science*, vol. 92, pp. 112 – 224, 2018.

[9] S. Kou, *Weld Metal Solidification I: Grain Structure*, ch. 7, pp. 170–198. John Wiley & Sons, Ltd, 2003.

[10] F. Yan, W. Xiong, and E. J. Faierson, "Grain structure control of additively manufactured metallic materials," *Materials*, vol. 10, no. 11, 2017.

[11] S. Kou, *Weld Metal Solidification II: Microstructure within Grains*, ch. 8, pp. 199–215. John Wiley & Sons, Ltd, 2003.

[12] K. M. B. Taminger, J. K. Watson, R. A. Hafley, and D. D. Petersen, "Solid freeform fabrication apparatus and method," Jan 2007.

[13] K. M. B. Taminger and R. A. Hafley, "Characterization of 2219 aluminum produced by electron beam freeform fabrication," in *13th Solid Freeform Fabrication Symposium*, pp. 458–465, Aug 2002.

[14] S. Inc, *Programming manual: Electron beam weld system.* 2002.

[15] B. Koscielny, "The effect of the inter-layer time interval on selective laser melted inconel 718," Master's thesis, University of Virginia, 2019.

[16] C. Huber, C. Abert, F. Bruckner, M. Groenefeld, O. Muthsam, S. Schuschnigg, K. Sirak, R. Thanhoffer, I. Teliban, C. Vogler, R. Windl, and D. Suess, "3d print of polymer bonded rare-earth magnets, and 3d magnetic field scanning with an end-user 3d printer," *Applied Physics Letters*, vol. 109, no. 16, p. 162401, 2016.

[17] L. Li, A. Tirado, B. Conner, M. Chi, A. M. Elliott, O. Rios, H. Zhou, and M. P. Paranthaman, "A novel method combining additive manufacturing and alloy infiltration for ndfeb bonded magnet fabrication," *Journal of Magnetism and Magnetic Materials*, vol. 438, pp. 163 – 167, 2017.

[18] C. V. Mikler, V. Chaudhary, T. Borkar, V. Soni, D. Jaeger, X. Chen, R. Contieri, R. V. Ramanujan, and R. Banerjee, "Laser additive manufacturing of magnetic materials," *JOM*, vol. 69, pp. 532–543, Mar 2017.

[19] B. Zhang, N.-E. Fenineche, L. Zhu, H. Liao, and C. Coddet, "Studies of magnetic properties of permalloy (fe30 % ni) prepared by slm technology," *Journal of Magnetism and Magnetic Materials*, vol. 324, no. 4, pp. 495 – 500, 2012.

[20] P. C. Magnetics, "All about neodymium magnets," Jan 2015.

[21] L. Li, B. Post, V. Kunc, A. M. Elliott, and M. P. Paranthaman, "Additive manufacturing of near-net-shape bonded magnets: Prospects and challenges," *Scripta Materialia*, vol. 135, pp. 100 – 104, 2017.

[22] L. Li, A. Tirado, I. C. Nlebedim, O. Rios, B. Post, V. Kunc, R. R. Lowden, E. Lara-Curzio, R. Fredette, J. Ormerod, T. A. Lograsso, and M. P. Paranthaman, "Big area additive manufacturing of high performance

bonded ndfeb magnets," *Scientific Reports*, vol. 6, pp. 36212 EP –, Oct 2016. Article.

[23] J. Geng, I. C. Nlebedim, M. F. Besser, E. Simsek, and R. T. Ott, "Bulk combinatorial synthesis and high throughput characterization for rapid assessment of magnetic materials: Application of laser engineered net shaping (lens^{TM})," *JOM*, vol. 68, pp. 1972–1977, Jul 2016.

[24] C. Mikler, V. Chaudhary, V. Soni, B. Gwalani, R. Ramanujan, and R. Banerjee, "Tuning the phase stability and magnetic properties of laser additively processed Fe-30at% Ni soft magnetic alloys," *Materials Letters*, vol. 199, pp. 88 – 92, 2017.

[25] V. Chaudhary, T. Borkar, C. V. Mikler, B. Gwalani, D. Choudhuri, V. Soni, T. Alam, R. V. Ramanujan, and R. Banerjee, "Additively manufactured functionally graded feni based high entropy magnetic alloys.," in *2018 IEEE International Magnetics Conference (INTERMAG)*, pp. 1–1, April 2018.

[26] B. Zhang, N.-E. Fenineche, H. Liao, and C. Coddet, "Microstructure and magnetic properties of feni alloy fabricated by selective laser melting fe/ni mixed powders," *Journal of Materials Science & Technology*, vol. 29, no. 8, pp. 757 – 760, 2013.

[27] B. Zhang, N.-E. Fenineche, H. Liao, and C. Coddet, "Magnetic properties of in-situ synthesized FeNi3 by selective laser melting fe-80 % Ni powders," *Journal of Magnetism and Magnetic Materials*, vol. 336, pp. 49 – 54, 2013.

[28] I. Shishkovsky and V. Saphronov, "Peculiarities of selective laser melting process for permalloy powder," *Materials Letters*, vol. 171, pp. 208 – 211, 2016.

[29] A. Mazeeva, M. Staritsyn, V. Bobyr, S. Manninen, P. Kuznetsov, and V. Klimov, "Magnetic properties of feni permalloy produced by selective laser melting," *Journal of Alloys and Compounds*, vol. 814, p. 152315, 2020.

[30] M. Yakout, M. Elbestawi, L. Wang, and R. Muizelaar, "Selective laser melting of soft magnetic alloys for automotive applications," 09 2019.

[31] L. J. Swartzendruber, V. P. Itkin, and C. B. Alcock, "The fe-ni (iron-nickel) system," *Journal of Phase Equilibria*, vol. 12, pp. 288–312, Jun 1991.

[32] R. B. Scorzelli, "Meteorites: messengers from the outer space," *Journal of the Brazilian Chemical Society*, vol. 19, pp. 226 – 231, 00 2008.

[33] K. B. Reuter, D. B. Williams, and J. I. Goldstein, "Determination of the Fe-Ni phase diagram below 400°C," *Metallurgical Transactions A*, vol. 20, pp. 719–725, Apr. 1989.

[34] A. Montes-Arango, L. Marshall, A. Fortes, N. Bordeaux, S. Langridge, K. Barmak, and L. Lewis, "Discovery of process-induced tetragonality in equiatomic ferromagnetic feni," *Acta Materialia*, vol. 116, pp. 263 – 269, 2016.

[35] L. H. Lewis, A. Mubarok, E. Poirier, N. Bordeaux, P. Manchanda, A. Kashyap, R. Skomski, J. Goldstein, F. E. Pinkerton, R. K. Mishra, R. C. K. Jr, and K. Barmak, "Inspired by nature: investigating tetrataenite for permanent magnet applications," *Journal of Physics: Condensed Matter*, vol. 26, jan 2014.

[36] R. Scorzelli, "A study of phase stability in invar fe–ni alloys obtained by non-conventional methods," *Hyperfine Interactions*, vol. 110, pp. 143–150, 9 1997.

[37] J. Kim, S. Kim, J.-Y. Suh, Y. J. Kim, Y. K. Kim, and H. Choi-Yim, "Properties of a rare earth free l10-feni hard magnet developed through annealing of fenipc amorphous ribbons," *Current Applied Physics*, vol. 19, no. 5, pp. 599 – 605, 2019.

[38] R. Bozorth, *Ferromagnetism*. Wiley, 1993.

[39] F. Pfeifer and C. Radeloff, "Soft magnetic ni-fe and co-fe alloys - some physical and metallurgical aspects," *Journal of Magnetism and Magnetic Materials*, vol. 19, no. 1, pp. 190 – 207, 1980.

[40] G. Herzer, "Nanocrystalline soft magnetic materials," *Journal of Magnetism and Magnetic Materials*, vol. 112, no. 1, pp. 258 – 262, 1992.

[41] T. Sawa and Y. Takahashi, "Magnetic properties of fecu (3d transition metals) sib alloys with fine grain structure," *Journal of Applied Physics*, vol. 67, no. 9, pp. 5565–5567, 1990.

[42] T. Sawa and Y. Takahashi, "Magnetic properties of fecu (3d transition metals) sib alloys with fine grain structure," *Journal of Applied Physics*, vol. 67, no. 9, pp. 5565–5567, 1990.

[43] K. Suzuki, A. Makino, N. Kataoka, A. Inoue, and T. Masumoto, "High saturation magnetization and soft magnetic properties of bcc fe-zr-b and fe-zr-b-m (m=transition metal) alloys with nanoscale grain size," *Materials Transactions, JIM*, vol. 32, no. 1, pp. 93–102, 1991.

[44] H.-Q. Guo, T. Reininger, H. Kronmller, M. Rapp, and V. K. Skumrev, "Magnetism and microstructure in nanocrystalline fecozr ferromagnets," *physica status solidi (a)*, vol. 127, no. 2, pp. 519–527, 1991.

[45] C. W. Chen, *Magnetixm and Metallurgy of Soft Magnetic Materials*. Amsterdam: North-Holland Publishing Company, 1977.

[46] A. Tabei, E. Mirkoohi, H. Garmestani, and S. Liang, "Modeling of texture development in additive manufacturing of ni-based superalloys," *The International Journal of Advanced Manufacturing Technology*, vol. 103, 07 2019.

[47] D. Ma, A. D. Stoica, Z. Wang, and A. M. Beese, "Crystallographic texture in an additively manufactured nickel-base superalloy," *Materials Science and Engineering: A*, vol. 684, pp. 47 – 53, 2017.

[48] A. Green, "150 years of industry & enterprise at enderby's wharf," 2016.

[49] G. W. Elmen, "Magnetic alloys of iron, nickel, and cobalt*," *Bell System Technical Journal*, vol. 15, no. 1, pp. 113–135, 1936.

[50] Lin Li, "Controlling annealing and magnetic treatment parameters to achieve high permeabilities in 55 ni-fe toroid cores," *IEEE Transactions on Magnetics*, vol. 37, no. 4, pp. 2315–2317, 2001.

[51] *Laser Additive Manufacturing Processing of a Mixture of Iron and Nickel Powders*, Lecture Notes in Computer Science, (Salt Lake City, UT), Materials Science & Technology 2016, 2016.

[52] A. W. International, "Nilo 52," 2020.

[53] "Standard specification for iron-nickel sealing alloys," standard, ASTM International, West Conshohocken, PA, 2017.

[54] Sandvik, "Osprey metal powders product range," 2015.

[55] T. W. Watson and H. E. Robinson, "Thermal Conductivity of Some Commercial Iron-Nickel Alloys," *Journal of Heat Transfer*, vol. 83, pp. 403–407, 11 1961.

[56] G. F. Vander Voort, *Metallography and Microstructures*. ASM International, 12 2004.

[57] "Standard practice for microetching metals and alloys," standard, ASTM International, West Conshohocken, PA, 2015.

[58] "Standard test methods for determining average grain size," standard, ASTM International, West Conshohocken, PA, 2013.

[59] S. Suwas and R. Ray, *Crystallographic Texture of Materials*. 01 2014.

[60] LakeShore, *Users Manual 7300 Series VSM System*. Lake Shore Cryotronics, Inc, Westerville, OH, 4 ed., 2 2001.

[61] D. . Chen, E. Pardo, and A. Sanchez, "Demagnetizing factors for rectangular prisms," *IEEE Transactions on Magnetics*, vol. 41, pp. 2077–2088, June 2005.

[62] Du-Xing Chen, E. Pardo, and A. Sanchez, "Demagnetizing factors of rectangular prisms and ellipsoids," *IEEE Transactions on Magnetics*, vol. 38, pp. 1742–1752, July 2002.

[63] R. Bjrk and C. R. H. Bahl, "Demagnetization factor for a powder of randomly packed spherical particles," *Applied Physics Letters*, vol. 103, no. 10, p. 102403, 2013.

[64] D. Jiles, C. Owen, and W. Spitzig, "Magnetic properties of porous iron compacts," *J Nondestruct Eval*, vol. 6, no. 9, pp. 119–127, 1987.

[65] L. Néel, "Bases d'une nouvelle théorie générale du champ coercitif," *Annales de l'université de Grenoble*, vol. 22, pp. 299–343, 1946.

[66] W. W. LaMorte, "The correlation coefficient (r)," 2019.

[67] I. B. L. Ltd., "Type 1 (k94490) iron-nickel soft magnetic alloy," 2009.

[68] B. Buchholz, E. F. Wassermann, W. Pepperhoff, and M. Acet, "Ir spectroscopy on feni and fept invar alloys," *Journal of Applied Physics*, vol. 75, no. 10, pp. 7012–7014, 1994.

[69] K. Jin, S. Mu, K. An, W. Porter, G. Samolyuk, G. Stocks, and H. Bei, "Thermophysical properties of ni-containing single-phase concentrated solid solution alloys," *Materials & Design*, vol. 117, pp. 185 – 192, 2017.

[70] A. Seifter, G. Pottlacher, H. Jger, G. Groboth, and E. Kaschnitz, "Measurements of thermophysical properties of solid and liquid feni alloys," *Berichte der Bunsengesellschaft fr physikalische Chemie*, vol. 102, pp. 1266 – 1271, 09 1998.

[71] C. Y. Ho, M. W. Ackerman, K. Y. Wu, S. G. Oh, and T. N. Havill, "Thermal conductivity of ten selected binary alloy systems," *Journal of Physical and Chemical Reference Data*, vol. 7, no. 3, pp. 959–1178, 1978.

[72] A. Sharan, T. Nagasaka, and A. Cramb, "Densities of liquid Fe-Ni and Fe-Cr alloys," *Metallurgical and Materials Transactions B*, vol. 25, pp. 939–942, Dec. 1994.

[73] A. Hozoorbakhsh, M. Hamdi, A. A. D. M. Sarhan, M. I. S. Ismail, C.-Y. Tang, and G. C.-P. Tsui, "Cfd modelling of weld pool formation and solidification in a laser micro-welding process," *International Communications in Heat and Mass Transfer*, vol. 101, pp. 58 – 69, 2019.

[74] G. Dumpich, E. Wassermann, V. Manns, W. Keune, S. Murayama, and Y. Miyako, "Structural and magnetic properties of nixfe1-x evaporated thin films," *Journal of Magnetism and Magnetic Materials*, vol. 67, no. 1, pp. 55 – 64, 1987.

[75] F. X. Zhang, K. Jin, S. Zhao, S. Mu, H. Bei, J. C. Liu, H. Z. Xue, D. Popov, C. Park, G. M. Stocks, W. J. Weber, and Y. Zhang, "X-ray absorption investigation of local structural disorder in ni1-xfex (x=0.10, 0.20, 0.35, and 0.50) alloys," *Journal of Applied Physics*, vol. 121, no. 16, p. 165105, 2017.

[76] R. Skomski, "Phase formation in l10 magnets," *Journal of Applied Physics*, vol. 101, no. 9, p. 09N517, 2007.

[77] V. L. Kurichenko, D. Y. Karpenkov, A. Y. Karpenkov, M. B. Lyakhova, and V. V. Khovaylo, "Synthesis of feni tetrataenite phase by means of chemical precipitation," *Journal of Magnetism and Magnetic Materials*, vol. 470, pp. 33 – 37, 2019. International Baltic Conference on Magnetism: focus on functionalized magnetic structures for energy and biotechnology.

[78] M. He, C. Wu, M. V. Shugaev, G. D. Samolyuk, and L. V. Zhigilei, "Computational study of short-pulse laser-induced generation of crystal defects in ni-based single-phase binary solidsolution alloys," *The Journal of Physical Chemistry C*, vol. 123, no. 4, pp. 2202–2215, 2019.

[79] R. W. Cahn and P. Haasen, "Preface to the third edition," in *Physical Metallurgy (Fifth Edition)* (D. E. Laughlin and K. Hono, eds.), pp. xv – xvi, Oxford: Elsevier, fifth edition ed., 2014.

[80] R. Honig and D. Kramer, *Vapor Pressure Data for the Solid and Liquid Elements*. RCA Laboratories, David Sarnoff Research Center, 1969.

[81] M. Mulvaney, "Electron beam freeform fabrication of alumninum: Investigating properties and cracking in alloys 2219 and 7075," Master's thesis, University of Virginia, 2019.

[82] C. Kim, K. Cho, and H. Suk, "A study of the effect of residual stress on magnetic properties of fe-ni thin film using a synchrotron x-ray," *The Physics of Metals and Metallography*, vol. 115, pp. 1338–1341, 12 2014.

[83] E. A. Wilson, " transformation in fe, feni, and fecr alloys," *Metal Science*, vol. 18, no. 10, pp. 471–484, 1984.

[84] E. A. Wilson, "Theoretical calculations of kinetics of equiaxed ferrite transformations in fe, feni, and fecr alloys," *Materials Science and Technology*, vol. 7, no. 12, pp. 1089–1100, 1991.

[85] V. Chaudhary, N. M. S. K. K. Yadav, S. A. Mantri, S. Dasari, A. Jagetia, R. Ramanujan, and R. Banerjee, "Additive manufacturing of functionally graded cofe and nife magnetic materials," *Journal of Alloys and Compounds*, vol. 823, p. 153817, 2020.

[86] C. Mikler, "Laser additive manufacturing of magnetic materials," Master's thesis, University of North Texas, 2017.

[87] Sciaky, "The ebw 110 system," 2020.

[88] Sciaky, "Benefits of wire vs. powder metal 3d printing," 2020.

[89] U. of Birmingham, "Soft magnetic materials."

[90] G. Herzer, *Soft Magnetic MaterialsNanocrystalline Alloys*. American Cancer Society, 2007.